A NEW MARTIAN GENERAL CIRCULATION MODEL:

APPLICATIONS TO THE MARTIAN HYDROLOGIC CYCLE

By

RICHARD ATSUKI URATA

B.A., University of California at Berkeley, 2005

M.A., University of Colorado at Boulder, 2008

A thesis submitted to the

Faculty of the Graduate School of the

University of Colorado in partial fulfillment

of the requirement for the degree of

Doctor of Philosophy

Department of Astrophysical and Planetary Sciences

2012

The thesis entitled:
A new Mars general circulation model: Applications to the Martian hydrologic cycle
written by Richard Atsuki Urata
has been approved for the Department of Astrophysical and Planetary Sciences

_____
(Fran Bagenal)

_____
(Brian Toon)

Date _____

The final copy of this thesis has been examined by the signatories, and we
Find that both the content and the form meet acceptable presentation standards
Of scholarly work in the above mentioned discipline.

Urata, Richard Atsuki (Ph.D., Astrophysical and Planetary Sciences)

A New Martian General Circulation Model: Applications to the Martian Hydrologic Cycle

Thesis directed by Professor Brian Toon

A new general circulation model for the simulation of the Martian climate is introduced. The model, based on the Community Atmosphere Model (CAM) version 3.1 developed by the National Center for Atmospheric Research (NCAR) is a three dimensional model with full support for multi-processor computing. The model is validated by comparing the simulation results to various spacecraft observations including atmospheric temperature, surface temperature, convective boundary layer depth, water vapor, and cloud opacity. Comparisons of zonal mean atmospheric temperatures are typically within 5 K of observations, and the largest divergences can be accounted for by including the radiative effects of water-ice clouds. Both the pattern and magnitude of the observations for the present-day water vapor and cloud annual cycles have been reproduced in the model.

The model is then used to study a hypothetical ancient Martian climate with a 500 mb CO_2 atmosphere, and a solar constant reduced to 75% of the current value. Sensitivity of the climate to the hydrologic cycle is tested assuming various amounts of initial atmospheric water, and cloud parameterizations. The results show that with an initial injection of at least 1000 pr-μm of water vapor, 10 μm cloud particles, and long

atmospheric water lifetimes, a stably warm climate can be achieved. In these climates, the globally averaged surface temperature is 265 K, with tropical annual mean temperatures above the freezing temperature of water.

Precipitation rates and patterns in the warm climates are investigated for obliquities ranging between 0° - 65°, and with the presence of oceans, to determine the conditions for river valley formation. Without oceans, significant precipitation at the river valley latitudes only happens at high obliquity, with an initial injection of 50 pr-cm of water into the atmosphere. With oceans, precipitation at river valley latitudes is observed at all obliquities, with local annual precipitation rates above 10 cm per Martian year. The latitudes for peak precipitation depend on obliquity, suggesting that if oceans were present on early Mars, the Noachian river valley should show periodical formation reflecting the obliquity cycle.

Table of Contents

List of Tables

List of Figures

Chapter 1: Introduction

The ancient climate of Mars has been a topic of interest for Mars research since the first observations of fluvial erosion features on the Martian surface by Mariner 9. Each following mission to Mars has revealed increasingly more evidence for a warm and wet past climate. One of the most compelling recent arguments for the warm and wet past of Mars is the widespread presence of the Martian river valley networks (Fassett and Head 2008a; Fassett and Head, 2008b; Hoke and Hynek, 2009; Di Achille and Hynek, 2010). These river valley networks are highly developed, and are indicative of long-term fluvial activity on the surface. The requirement for such features is that the surface temperatures are warm enough to sustain liquid water at the surface for 10^5-10^8 years (Craddock and Howard, 2002; Hoke and Hynek, 2011). However, while the geological evidence for a warm and wet past climate has accumulated over the years, finding a self-consistent set of conditions for a warm and wet climate has proven to be a difficult task.

Early 1-dimensional models of the ancient Mars climate showed that even with a solar constant near the present day value, many bars of CO_2 would have been required to achieve global mean surface temperatures of 273 K (Pollack et al., 1987; Kasting, 1991).

The solar constant at the time of river valley formation was between 70-75% of the present day value; a value for which a CO_2 greenhouse could not have led to a warm and wet climate according to Kasting (1991), due to the condensation of CO_2 lowering the atmospheric lapse rate and decreasing the greenhouse effect. Subsequent attempts have been made to find stable warm and wet early climates to varying degrees of success (Haberle, 1998; Segura et al., 2002, 2008; Johnson et al., 2008; Toon et al., 2010; Wordsworth et al., 2011). However even when possible solutions for warm climates were found, the results have been met with speculation because the resulting climates are transient, and only last for a few hundred years.

One process that the previous studies have not examined in detail is the water cycle, and the radiative effects of water-ice clouds in the ancient Mars climate. The purpose of this work is to introduce a new general circulation model for Mars, and use the model to study this question about the ancient Martian climate. Specifically, we look at the Martian water cycle in the present, as well as in the past, and look at whether or not a stably warm and wet ancient climate could have been achieved through greenhouse warming by water vapor and water clouds.

Modeling of the Martian climate has been around since the early days of climate modeling (Leovy and Mintz, 1969). These climate models have been proven to be useful tools for studying many questions related to the Martian climate including dust storms (Murphy et al., 1995, etc.), water-ice clouds (Montmessin et al., 2004; Machtoub, 2012; etc.), and carbon dioxide clouds (Colaprete et al., 2008; etc.). There are currently multiple different general circulation models in use by researchers of the Martian climate, with the NASA Ames model (Pollack et al., 1981, 1990; Haberle et al., 1993, 2003), and the

Laboratoire de Meteorologie Dynamique (LMD) model (Hourdin et al., 1995; Forget et al., 1999) being two of the pioneering models in the field.

The main body of the thesis is presented in chapters two through four. Chapter two introduces the new general circulation model that we have developed. This includes a general description of the model, a discussion of the changes made to the model for simulating the Martian climate, and a comparison to spacecraft observations of the climate in order to validate the model results. Chapter three expands on chapter two, and focuses more on the water cycle, and the radiative effects of water-ice clouds. Spacecraft observations of water vapor and water-ice opacity are used to assess the model's ability to simulate the Martian water cycle, and to understand where the model deficiencies are. The model is then used to study the ancient Martian climate with a 500 mbar CO_2 atmosphere, and a reduced solar constant, in order to study the possible effects of a water cycle greenhouse. Chapter four uses the model to simulate the ancient climate, and look at the precipitation patterns under various obliquities and water sources, to see if significant precipitation could be found where the river valleys are observed. Chapters two and three are papers that have been submitted, and are currently undergoing the review process. Chapter four is a paper that is in preparation, and planned to be submitted in the near future.

Chapter 2: A new general circulation model for Mars based on the NCAR Community Atmosphere Model

2.1 Introduction

The Mars General Circulation Models (GCMs) in existence today have been all adapted from terrestrial GCMs developed by the terrestrial atmosphere modeling community. Models developed in this fashion include the NASA/Ames GCM (Pollack et al., 1981, 1990; Haberle et al., 1993, 2003), the Laboratoire de Meteorolgie Dynamique (LMD) GCM (Hourdin et al., 1995, Forget et al., 1999), and planetWRF developed by the Jet Propulsion Laboratory and Caltech (Richardson et al., 2007) among others (Wilson and Hamilton, 1996; Richardson and Wilson, 2002; Moudden and McConnell, 2004; Kuroda et al., 2005). Here we introduce a new Mars GCM, adapted to Mars from the Community Atmosphere Model (CAM version 3) developed by the National Center for Atmospheric Research (NCAR) (Collins et al, 2004), and describe the ability of the model to reproduce the climate of current Mars. In a companion paper (Urata and Toon, 2012b) we use the model to simulate the current water vapor/cloud cycle on Mars, apply the model to understand the water vapor greenhouse effect on Mars and employ the model for paleo-climate simulations.

2.1.1 General Circulation Models of the Martian Atmosphere

General circulation models of the Martian atmosphere began with the work of Leovy and Mintz (1969). For their work, they adapted to Martian conditions a GCM recently developed for Earth by a team at UCLA. Their model successfully predicted the condensation of CO_2, and the existence of baroclinic waves. Researchers working at the NASA Ames Research Center further improved upon this model, and their modeling has provided many useful findings about the Martian climate (Pollack et al., 1981, 1990; Haberle et al., 1993, 2003). In addition to simulating climate patterns under varying parameters, their simulation results have also been used to determine likely meteorological conditions at spacecraft landing sites (Haberle et al., 1997). The Ames Mars GCM has been used to simulate Martian dust storms (Murphy et al., 1995), the hydrological cycle (Nelli et al., 2009), water and carbon dioxide clouds (Colaprete et al., 2008) and numerous other features of the Martian climate.

In 1995, a group at the Laboratoire de Meteorologie Dynamique adapted a terrestrial model developed by LMD researchers to Martian conditions by adding a new radiative transfer code and CO_2 condensation (Hourdin et al., 1995) reproducing the pressure variations observed by the Viking landers. Like the NASA/Ames GCM, this model has also evolved and undergone upgrades (Forget et al., 1999). The LMD model incorporates modern dynamical algorithms and also includes a chemistry package for in-depth studies of atmospheric composition (Lefevre et al., 2004).

The Geophysical Fluid Dynamics Laboratory (GFDL) also has a Mars GCM, which is based on the terrestrial "Skyhi" model (Wilson and Hamilton, 1996; Richardson and Wilson, 2002). This is a proven, modern model capable of running on multiple

processors, with well-developed physics modules, and has the computational advantage of using a “cubed-sphere” grid.

Richardson et al., (2007) adapted NCAR’s Weather Research and Forecasting (WRF) regional model to Mars to create PlanetWRF. PlanetWRF is a computationally modern model, capable of simulations from the regional scale to the global scale. The model includes a nesting capability, enabling small-scale simulations over particular areas, and coarser resolution elsewhere in order to save computation power.

These models, and others (Moudden and McConnell, 2005; Hartogh et al., 2005; Kuroda et al., 2005) make up a large community of Mars general circulation models. We chose to develop a new model based on the NCAR CAM models, because the CAM models are supported by a large group of developers at NCAR, the basic model is distributed to the community so it is available to all interested users, it is a modern model with advanced numerics that runs well on modern computers, and the physics packages in the model are well developed.

2.2 Description of the Model

The model used in this research has been adapted to Martian conditions from the Community Atmosphere Model (CAM) developed by the National Center for Atmospheric Research (NCAR) (Collins et al., 2004). CAM is a fully modern circulation model that includes the ability for computations on parallel processors, a conservative finite-volume dynamical core, and output in NetCDF format for simple analysis. The

ability to run the model in parallel is a key feature that makes simulations significantly faster than older models that do not possess the same capability.

CAM is structured in such a way that makes expanding the capabilities of the model relatively simple. The most extensive expansion of the model is called the Whole Atmosphere Community Climate Model (WACCM). WACCM couples two additional models to CAM. A chemistry model called the Model of Ozone and Related Tracers (MOZART), and the Thermosphere-Ionosphere-Mesosphere-Electrodynamics Processes (TIME) model for upper atmosphere physics. These models in addition to the inherently coupled Community Land Model (CLM) and Slab Ocean Model (SOM) allow for our model to be potentially used to investigate many different questions in all regions of the Martian atmosphere. The land model provides the ability to simulate a comprehensive hydrologic cycle, including precipitation, infiltration, runoff, and evaporation, or sublimation.

We employ the fourth generation of NCAR's CAM model (CAM 3), which was originally released in 1996. Recently, the newest version of the model (CAM5) was released. However we have not yet had the opportunity to upgrade our Mars model to this version. The main improvements made in the newer versions are increased flexibility with the radiation transfer, the addition of a modernized aerosol model for parallel processing, and better physics to include interactions with aerosols.

The finite-volume dynamical core in CAM3 (and CAM5) conserves mass, momentum, and total energy, making it very appealing. The horizontal discretization of the transport process is based on the "flux-form semi-Lagrangian" scheme developed by Lin and Rood (1996). In this scheme two 1-D orthogonal flux-form transport operators

characterize the horizontal transport. These two are then combined to find the 2-D transport. The vertical discretization is Lagrangian, using a hybrid sigma-p coordinate system. In order to ensure conservation, a re-mapping algorithm is applied based on mass, momentum, and total energy.

The longwave radiation transfer scheme in CAM3 is based on the broad-band model approach (Kiehl and Briegleb, 1991; Kiehl and Ramanathan, 1983). This method has the advantage of being simple and computationally efficient, however it lacks the versatility needed in an atmosphere where carbon dioxide is the major atmospheric component, and scattering by dust in the infrared is important, such as on Mars. Hence we have replaced the CAM3 radiation code as discussed below.

2.2.1 Basic constants for Mars

In adapting the model to Mars, a number of changes were required. Table 2.1 lists the fundamental planetary parameters with the corresponding Martian values. Table 2.2 summarizes the relevant atmospheric constants used in the model. The dry atmosphere is assumed to have a composition of 95% carbon dioxide, 3% nitrogen, and 2% argon. The condensation of carbon dioxide at the winter pole on Mars enriches the concentration of nitrogen, argon, and other trace gasses. However, we do not take the trace gas enrichment into consideration in our model at this time. The dynamic viscosity of carbon dioxide was determined experimentally by Pang et al. (2005) using a simulated Martian atmosphere.

Variable	Value	Source
Gravity	3.72 m s^{-2}	Williams, D.R. (2010)

Mars orbit semi-major axis[2]	2.321547 AU[2]	Williams, D.R. (2010)
Obliquity	25.19	Williams, D.R. (2010)
Eccentricity of orbit	0.09334	Williams, D.R. (2010)
Areocentric Longitude of perihelion (L_s)	250.9	Allison and Schmunk, 2008
Length of year	668.6 sols	Allison and Schmunk, 2008
Length of sidereal day	88642.663 s	Williams, D.R. (2010)
Planetary radius	3.38992×10^6 m	Williams, D.R. (2010)
Topography	Fig. 2.1	Smith, D. et al. (2003)

Table 2.1. Mars planetary parameters.

Variable	Value	Source
C_p dry air	735 J kg^{-1} K^{-1}	Specific heat of pure CO_2 at 200 K, constant pressure
Dry adiabatic lapse rate	5.06×10^{-3} K m^{-1}	g / c_p
Molecular weight of dry air	43.34 g mol^{-1}	
Dry air gas constant	191.84 J kg^{-1} K^{-1}	$R_{universal} / MW_{dry\ air}$
Dynamic viscosity of air	1.45×10^{-3} Pa s	Pang et al. 2005

Table 2.2. Basic atmospheric properties.

The topography field is derived from Mars Orbiter Laser Altimeter (MOLA) data (Smith et al., 2003). The data are available at horizontal resolutions of 4, 16, and 32 pixels per degree. Because we are interested in resolutions larger than 1 degree, we have chosen to use the 4 pixels per degree data set. The data are averaged to the CAM grid by CAM, which takes the mean height of the grid-cell, and then finds the standard deviation of the height over the same area, which is later used in gravity wave drag and mountain stress calculations. Figure 2.1 displays the topography field at a resolution of 2x2.5 degrees (lat-lon).

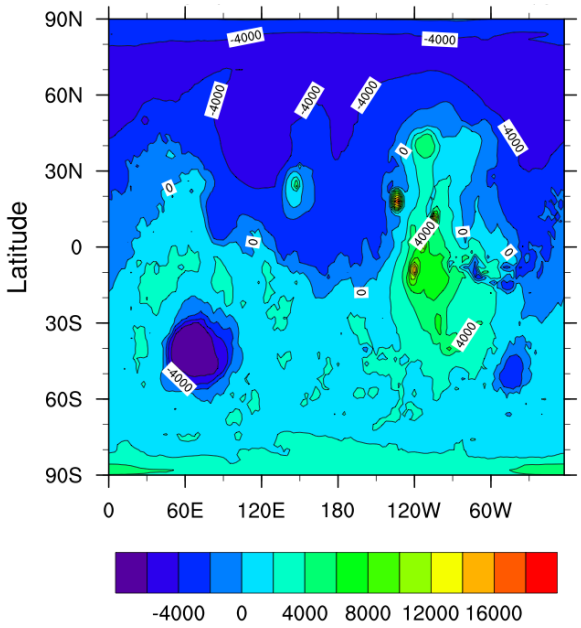

Figure 2.1. Model topography at a resolution of 2°x2.5° (heights in m).

Time is kept in the Mars-CAM model by reference to L_s=0, the time at which the Northern Hemisphere spring equinox occurs. The zero second is defined as midnight at 0º longitude.

2.2.2 Surface properties and energy budget for Mars

CAM has a sophisticated set of routines for the surface energy budget (Oleson et al., 2004). We chose the desert planet settings in CAM to represent present-day Martian conditions, which assumes that all land is dry, and has sand-like properties. The CAM model solves for the temperature at the surface with the standard heat balance equations when condensation is not occurring:

$$(d/dz)(S^* - \varepsilon(\sigma T_g^4 - F) + kdT/dz + H) = \rho c_p dT_g/dt \qquad (2.1)$$

In this equation, S* is the net solar energy deposited at the surface, which is computed by the radiative transfer code. In the absence of an atmosphere it would be equal to (1-A)S cos(i) where A is the surface albedo; S is the solar constant; and *i* is the solar incidence angle. ε is surface emissivity; T_g is the surface temperature; F is the net downward irradiance from the atmosphere (including reflection from the surface) which is computed by the radiation code; *k* is the thermal conductivity of the ground; *dT/dz* is the vertical temperature gradient in the soil with z positive downward; and *H* is the sensible and moisture heat flux from the soil. The right-hand side of the equation represents the time rate of change of the surface energy represented as a rate of temperature change multiplied by the heat capacity of soil times the density.

The albedo dataset was averaged to model resolutions from TES observations as illustrated in Fig. 2.2. The albedo, which is derived from Mars Global Surveyor Thermal Emission Spectrometer (MGS TES) data, is measured as the fraction of solar energy that is reflected at wavelengths between 0.3 – 2.9 μm (Christensen et al., 2001). While the surface is not gray across the spectrum, the use of this broad-band parameter as a constant across all wavelengths yields accurate results for the surface temperature, as discussed in later sections. We will discuss the application of the albedo data to the radiative transfer calculations below.

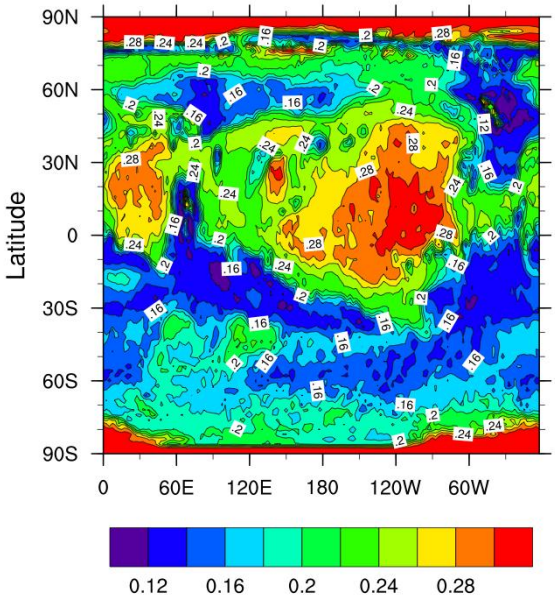

Figure 2.2. Model broadband surface albedo at a resolution of 2°x2.5°. Polar regions are assumed to have an albedo that corresponds to ice.

For the surface emissivity, we use the default settings in CAM. This value is 0.96 for bare land, 0.97 for glaciers, 0.96 for wetlands, and 0.97 for snow-covered surfaces. The value is reduced to 0.8 for areas that are covered by condensed carbon dioxide.

The thermal inertia dataset (Fig. 2.3) was created from Putzig's (2007) data derived from TES surface temperature measurements. We averaged this dataset to the desired resolution for our simulations, typically 2x2.5, or 4x5 degrees latitude by longitude.

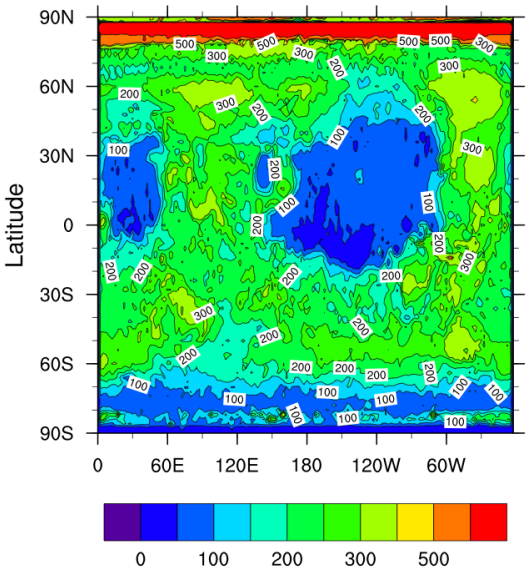

Figure 2.3. Model thermal inertia (J m^{-2} K^{-1} $s^{-1/2}$). Polar regions are assumed to have a thermal inertia that corresponds to ice (approximately 2000).

Comparing the topography, albedo, and thermal inertia datasets (Fig. 2.1-2.3), we can see that most of the southern hemisphere is higher than the northern hemisphere, and is also relatively dark compared to the north. Also of note, is that the regions of high albedo (higher than 0.25) roughly correspond to areas with low thermal inertia (50-70 J m^{-2} K^{-1} $s^{-1/2}$, compared to 100-400 J m^{-2} K^{-1} $s^{-1/2}$ in the dark regions). Specific topography features also stand out in albedo and thermal inertia. For example, the deep Hellas basin has low albedo and high thermal inertia. The high altitude Tharsis volcanic construct has high albedo and low thermal inertia.

While the thermal inertia is used in computing the thermal conduction in the soil, one also needs the soil density and soil heat capacity, given in Table 2.3. The values for soil density and soil heat capacity in Table 2.3 were taken from Mellon et al. (2000) who also compiled a global thermal inertia map for Mars. The thermal inertia is defined as $I=(k\rho c)^{1/2}$. The thermal inertia (Fig. 2.3), soil density, and soil heat capacity are used to

determine the soil thermal conductivities in the model. The CAM subsurface model has 10 layers. The top layer is 0.7 cm thick, with each subsequent layer exponentially thicker, so that the total depth of the layers is 2.8 meters.

Variable	Value	Source
Average soil density	1500.0 kg m^{-3}	Mellon et al. 2000
Average soil heat capacity	627.9 J kg^{-1} K^{-1}	Mellon et al. 2000

Table 2.3. Properties of the soil.

An important consideration in the surface energy balance is the transport of sensible and latent heat between the ground and atmosphere, H. The sensible heat transport is controlled by stability conditions, which depend on the temperature difference between the first atmosphere layer and the ground, the air density, the specific heat capacity of air, and the friction velocity. The latent heat transport is affected by ice that may be deposited on the surface as well as water that is present in the soil. The transport of soil moisture in the model is done by diffusion with a soil moisture potential. The details are described in Oleson et al. (2004). We initialize the model assuming that there is no moisture in the soil. However, ice is deposited on the surface in the model, and latent heat release occurs when it sublimes from the surface.

2.2.3 Surface energy balance with condensation

Carbon dioxide condensation and sublimation in the polar regions is an important process on Mars. We compute the mass deposited or lost (we ignore condensation in the atmosphere presently) as:

$$S^* - \varepsilon(\sigma T_g^4 - F) + kdT/dz + H = -Ldm/dt \qquad (2.2)$$

The terms on the left hand side of the equation have the same meanings as in Eq. 2.1. *L* is the latent heat of sublimation for carbon dioxide (776 kJ kg^{-1}); *dm/dt* is the rate of change of the mass per unit area of the carbon dioxide frost. The surface temperature in this case is the calculated carbon dioxide frost point temperature. Using this temperature for the ground temperature assumes that the latent heat exchange from condensation and sublimation will keep the temperature constant at the frost point.

Table 2.4 lists the physical parameters used in the CO_2 condensation model. The density of carbon dioxide snow was found by Smith et al. (2001) by observing the annual change in polar cap height, and comparing it to the change in the $C_{2,0}$ coefficient of the aeroid. In the model, the density of carbon dioxide snow is used to determine the depth of the snow. Unfortunately, the albedo and emissivity of the condensed carbon dioxide are poorly known. Measurements (Paige and Ingersoll, 1985), and model studies (Warren et al., 1990) found these values to range between 0.7-1.0 for emissivity, and 0.4-0.8 for albedo. The Warren study concluded that these values are very sensitive to grain size, water snow content, and dust content. The values used in this model of 0.6, and 0.8 for the albedo and emissivity respectively, were chosen by Hourdin et al. (1993) to achieve the observed annual pressure cycle.

Variable	Value	Source
Carbon dioxide snow density	910.0 kg m^{-3}	Smith et al. 2001
Carbon dioxide latent heat of sublimation	7.76×10^5 J kg^{-1}	Latent heat of fusion + vaporization
Carbon dioxide snow visible albedo	0.6	Hourdin et al. 1993
Carbon dioxide snow ir emissivity	0.8	Hourdin et al. 1993

Carbon dioxide vapor pressure	Varies with T	
Water ice specific heat	2.054e3 J kg^{-1} K^{-1}	Collins et al. 2004
Water ice heat of fusion	3.34e5 J kg^{-1}	Collins et al. 2004
Water ice heat of evaporation	2.501e6 J kg^{-1}	Collins et al. 2004

Table 2.4 Properties of condensates.

Presently, any carbon dioxide that condenses to the surface is deposited on top of any existing water ice sheets or snow, and no mixing between the carbon dioxide and water snow is accounted for. If there is any snow (H_2O) on top of the bare ground, the temperature profile is calculated, and the top layer of the snow is used for the temperature gradient calculation. Depending on the amount of snow, the model allows for up to 5 layers, and performs heat transfer calculations in a module separate from the carbon dioxide condensation. The carbon dioxide snow is assumed to form a single isothermal layer on top of the snow.

2.2.4 Radiative transfer

We have replaced the radiative transfer code in CAM so that we are able to treat scattering in the infrared, and so that the infrared and visible radiation schemes are consistent. We use the two-stream radiative transfer algorithm developed by Toon et al (1989). The particular version we employ was updated to Fortran 90 by T. Michaels (personal communication). Similar algorithms are used widely in the Mars community. For instance they are employed in the NASA Ames GCM (Haberle et al., 1999), and in the 1-D climate models used by Kasting (Kasting, 1991, Pavlov et al., 2000). The algorithm uses a delta-Eddington approximation to the two stream equations for visible

wavelengths. At infrared wavelengths we use the hemispheric mean two-stream approximation to treat scattering and the isotropic emission from the Planck function, as discussed by Toon et al (1989). We also use the integral form of the radiative transfer solution, which is "exact" in the limit of no scattering. We use 8 gauss points to perform the integrations. Some treatments using the Toon et al. (1989) algorithm only use the two stream equations in the infrared, which is inherently less accurate.

The absorption coefficient data set we use is based on that employed in the NASA Ames GCM, and by Kasting (1984, 1991). The model uses the "correlated-k" technique. This data set was developed for high carbon dioxide pressures, ranging up to 10 bars. One computational issue with the correlated-k technique set is the treatment of the overlap of absorption bands between gasses. As discussed by Haqq-Misra (2008), the brute force approach leads to the requirement that thousands of calculations of column radiative transfer be done each time step. To reduce the computational demands we have implemented the method described by Colaprete and Toon (2003) in which overlap is treated with an equivalent absorber approach. This same approach is widely used in modern terrestrial GCMs. Our set of k coefficients is essentially identical to that used by Colaprete and Toon (2003). Optical depths are calculated over 60 wave bands, ranging between 40 cm^{-1} and 40000 cm^{-1}, assuming water and carbon dioxide to be the predominant gas absorbers. We also include the pressure-induced absorption of water vapor and carbon dioxide. We use the method of Wordsworth et al. (2010) for carbon dioxide, and follow the method of Thomas and Nordstrom (1985) for water vapor. The Rayleigh scattering is calculated using the method of Hansen and Travis (equation 2.32, 1974) for a pure CO_2 atmosphere, scaled to Mars pressure and gravity from Venus. This

is shown below in Eq. 2.3. λ is the wavelength in microns, g is Venusian gravity (870 cm s^{-2}), g' is Martian gravity, P is the pressure of the level, and P_0 is the surface pressure of Venus (93 atmospheres).

$$\tau_{ray} = 1.527\lambda^{-4}(1.+0.013\lambda^{-2})*(g/g')*(P/P_0) \quad (2.3)$$

The formation of carbon dioxide clouds, and their radiative effects have not been considered at this time. Radiative transfer in liquid- and ice-water clouds are included. However their treatment will be discussed in the companion paper (Urata and Toon, 2012b) that has a larger focus on the water cycle. The results presented here do not include the radiative effects of clouds.

2.2.5 Boundary layer parameterization

To calculate turbulent processes, CAM finds the local turbulent diffusivities of the free atmosphere, and uses an explicit, non-local parameterization for the planetary boundary layer. The turbulent diffusivities are expressed as functions of an eddy length scale, and local vertical gradients of wind and virtual potential temperature. A detailed description of the calculation can be found in Collins et al. (2004). We have made minimal changes to this part of the model, and have largely adopted the CAM parameterizations directly. One of the few changes made included lowering the artificially set maximum possible boundary layer pressure height to 0.1 mb from 400 mb; without which the model would incorrectly limit the boundary layer to the bottom model level and report unrealistically shallow boundary layers.

2.2.6 Dust and tracer transport and radiation

Dust vertical transport and microphysics are calculated by the University of Colorado/NASA Community Aerosol and Radiation Model for Atmospheres (CARMA) (Toon et al. 1988). CARMA was also used by Colarpete and Toon (2003) to study Martain water and CO_2 clouds. An early version of CARMA was also used by Murphy et al. (1990, 1993) to simulate Martian dust storms, as well as in the NASA Ames Mars GCM. However, while CARMA has been coupled to CAM, we do not consider dust transport in this paper, and presently do not use CARMA to perform the ice cloud microphysics.

Instead, we include a constant dust background with a single particle size of 2 microns, following a vertical distribution described by Conrath (1975) corresponding to an optical depth at 1075 cm^{-1} ranging between 0.1-0.3; typical values for periods of normal dust activity (Colburn et al., 1989). We assume a ν parameter value of 0.03, which controls the vertical dust concentration in the Conrath formulation, following Pollack et al. (1990), in which $q = q_0 \exp(\nu(1-P_0/P))$, where P_0 is the average surface pressure, P is the local pressure, and q_0 is the dust specific concentration at P_0. To simulate low polar dust concentrations, we have set the column dust optical depth above 70 degrees latitude to a tenth of the value of the rest of the planet. The wavenumber dependent dust optical depth for each layer is calculated through Eq. 2.4. In this equation, r is the dust particle radius, q is the dust specific concentration (in number per gram of atmosphere) of the layer of thickness ΔP, $Q_{ext,\upsilon}$ is the wavenumber dependent extinction

efficiency, and g is gravity. Q_{ext} is obtained using a Mie code and the dust optical constants from Wolff and Clancy (2003).

$$\tau_{dust,\nu} = \pi r^2 \, q \, Q_{ext,\nu} \, \Delta P / g \qquad (2.4)$$

We transport water vapor and condensed water using the CAM transport algorithms, and hydrological cycle. The CAM hydrological cycle is described in Collins et al. (2004). At every time step, CAM calculates cloud coverage and thicknesses from the transported, and newly condensed water in the grid-cell. We have not allowed clouds to impact the calculations in this paper, but do consider them in the companion paper (Urata and Toon, 2012b). In the radiative transfer code, we consider partial gridbox cloud saturation and overlap using a Monte-Carlo independent column approximation method (Pincus et al., 2003). This method provides a fast, reliable method to account for the clouds not completely covering the typically very large grid cells and overlapping in altitude. The radiative effects of clouds are calculated through their column optical depths, found from the column mass of cloud ice, and the optical properties calculated using Mie theory, assuming a particle size for clouds typical on Mars (Eq. 2.5). Here, M_{cloud} is the layer cloud water path (g/m^2), $Q_{ext,\nu}$ is the wavenumber dependent extinction efficiency obtained via Mie theory and the optical constants for ice from Segelstein (1981) and Warren and Brandt (2008) for water and ice, respectively, ρ_{cloud} is the cloud particle density, and r is the cloud particle size.

$$\tau_{cloud,\nu} = (3 M_{cloud} \, Q_{ext,\nu}) / (4 \rho_{cloud} \, r) \qquad (2.5)$$

The column mass of cloud ice is calculated by first determining the saturation vapor pressure for water in each grid cell. If the grid cell is supersaturated, or clouds are present while the grid cell is not saturated, then water is condensed or evaporated until saturation

is reached. The remaining condensate is assumed to form water or ice cloud particles depending on the environmental temperature. Transport of clouds is performed as a mass flux by the dynamical core, while precipitation is a separate process that assumes an auto-conversion rate of cloud condensate to precipitate, which then falls with a Stokes velocity. We further discuss the hydrological cycle in Urata and Toon (2012b).

2.3 Simulation Results

Hundreds of papers have been written analyzing various aspects of the behavior of the Martian atmosphere. Our goal here is not to do a detailed analysis of the model's performance on every aspect of the Martian atmosphere, but instead to generally characterize the behavior of this model, at its current state of development. There are a number of areas in which model improvements could be made; for example the model would better simulate the current climate if we included a fully interactive dust cycle instead of a fixed background. However, despite lacking these processes, the model performs satisfactorily as we will show. We have validated the model against observations of Mars that are most relevant to its climate. To determine the realism of the model, our simulations are compared to Mars Global Surveyor Thermal Emission Spectrometer (TES) retrievals of the nadir atmosphere temperature, Mars Exploration Rover (MER) retrievals of the surface and 1 meter temperatures (Smith et al., 2006), Viking Lander measurements of annual pressure cycles (Murphy, et al., 1990), and convective boundary layer depths reported by Hinson et al. (2008). Since we have included fixed background dust, we only selected the non-global dust storm year TES

measurements for comparison. However, even in years without dust storms there is an appreciable optical depth of dust (Elteto and Toon, 2010) during the southern summer season, thus we have refrained from making comparisons during these periods.

2.3.1 Model Initial Parameters

The model was spun up from a rest state with a globally uniform temperature distribution of T = 250K. The model typically starts with no soil moisture, and only the northern water ice cap as a source; hence it is initially very dry. Likewise, there are no permanent CO_2 caps initially, and the total amount of CO_2 is initially in the atmosphere. The model was allowed to spin up for four Martian years, and the reported results come from simulations following the spin up phase. The model was run at a resolution of 4x5 degrees (latitude x longitude), and has 26 vertical hybrid-sigma pressure levels with the top at approximately 60 km. For reference such a model can be run using 16 processors on a Macintosh computer in about 12 hours per Martian year.

2.3.2 Simulated Temperatures and Comparison with Measurements

In order to compare the model simulations to the TES measurements, the times corresponding to L_s = 0°, 90° were chosen. These are the northern spring (0°) equinox, and the northern summer solstice (90°). The reason for choosing these particular times of year was because these periods mark turning points in the seasons of the Martian year, and are thus good indicators for the model's performance. We chose not to include

comparisons from the northern winter solstice, L_s=270° because this is typically when dust storm activity is highest, and our model does not include dust storms. The 180^o case is sufficiently similar to the 0^0 case that we do not show it. In each case, we include comparative plots assuming different dust concentrations to observe the sensitivity to dust. TES data are obtained twice daily at approximate local times of 2 AM, and 2 PM. In order to suppress longitudinal variability we averaged the TES temperature profiles over longitude. Nighttime temperature fields do not differ significantly from those during the day, except for the lowest portion of the atmosphere. Our model results were also averaged over longitude, with profiles chosen from the approximate local times of the TES overpass.

Figures 2.4a-2.4e are plots of the zonally averaged temperatures comparing the model results to the data for Ls=0^o. Due to a lack of data, we are not able to make comparisons above roughly the 10 Pa pressure level, so the model plots have been truncated in the vertical to match the TES data. Figure 2.4a shows the zonally averaged temperature from the TES measurements. Figures 2.4b and 2.4c are the model zonally averaged temperatures for two different column dust optical depths (τ_{dust}); 0.1, 0.3. The optical depths refer to the 1065-1108 cm^{-1} waveband. Plots 2.4d and 2.4e are the temperature differences (model – TES) for the column dust optical depths of 0.1 and 0.3 respectively.

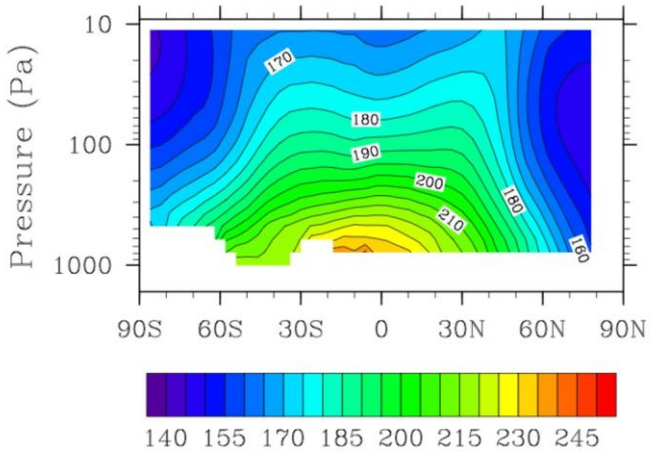

Figure 2.4a. Zonally averaged temperatures at L_s=0° for TES.

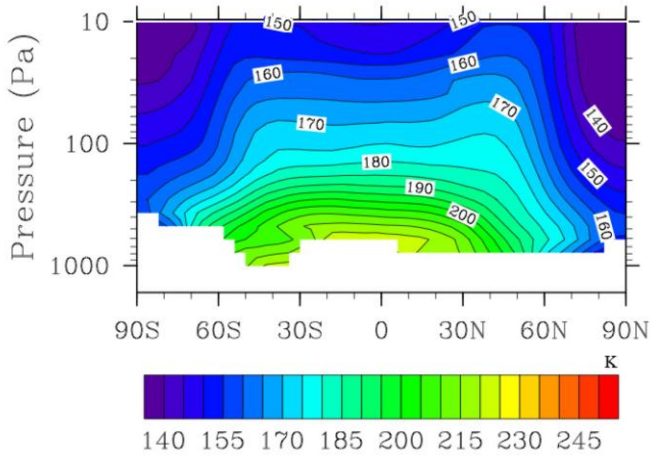

Figure 2.4b. Zonally averaged temperatures at L_s=0° for τ_{dust}=0.1 between 1065-1108 cm^{-1}.

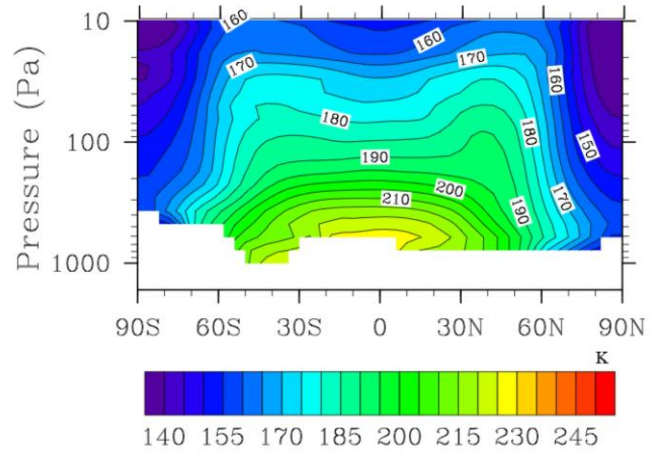

Figure 2.4c. Zonally averaged temperatures at L_s=0° for τ_{dust}=0.3 between 1065-1108 cm^{-1}.

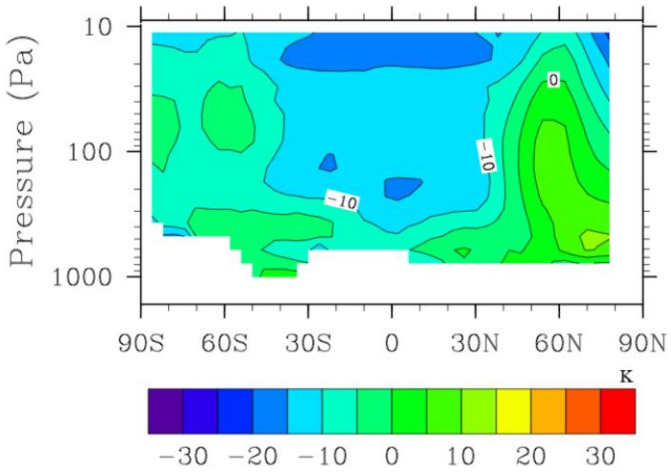

Figure 2.4d. Zonally averaged temperatures at L_s=0° for Model – TES temperature difference for τ_{dust}=0.1.

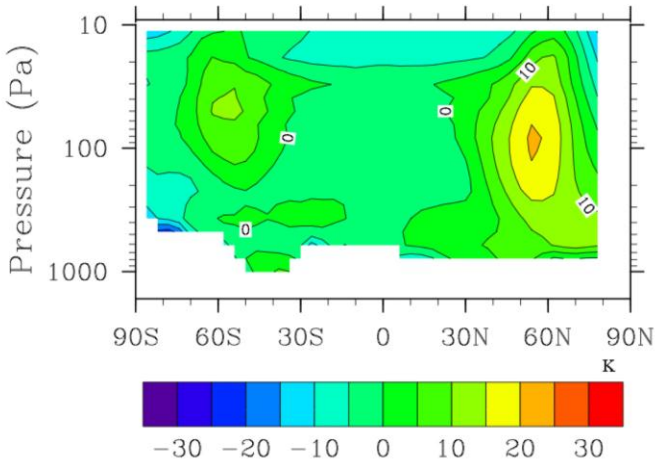

Figure 2.4e. Zonally averaged temperatures at L_s=0° for Model – TES temperature difference for τ_{dust}=0.3.

The general morphology of the zonally averaged temperature is the same in the data and in the model. In all cases, the temperature is roughly symmetric about the equator, with temperatures decreasing towards the poles. There is little difference between the various dust concentration simulations except for slightly higher atmospheric

temperatures corresponding with higher dust concentrations. In the τ_{dust} = 0.1 case, the model is typically 10-15 K cooler than the data near the equator, and up to 10 K warmer at some locations in the high northern latitudes. The τ_{dust} = 0.3 case is similar to the τ_{dust} = 0.1 case, but the model temperatures are raised by roughly 5 K in all locations. In the lower latitudes, the model is roughly 5 K cooler at the 100 Pa level. At the higher northern latitudes, the model is up to 15 K higher than the data. In summary, the model is most consistent with the data in the tropics and the Southern high latitudes for a dust optical depth near 0.3. However, an even lower optical depth is needed for the high Northern latitudes. It should be noted that Urata and Toon (2012b) show that water ice clouds also have a significant impact on the atmospheric temperature. In particular they warm high altitudes above the equator, which is somewhat cold in Fig. 2.4, and cool the lower atmosphere above the poles.

The cause for the model being much warmer than the data near 60°N is unclear. A likely contributing factor is the dust opacity being too high even for an optical depth of 0.1 (we made the dust optical depth 0.01 poleward of 70^{o}). Alternatively, the issue may be related to lack of radiative forcing by water-ice clouds in these simulations. TES observations (Smith, 2008) show an increase in water-ice opacity around this time of year at this latitude. Clouds tend to locally cool the atmosphere by reflecting incoming solar radiation, and radiating in the infrared, but they also heat by absorbing radiation from the ground. The degree of cooling or heating depends on cloud height and thickness, as well as the temperature difference between the ground and the cloud. The radiative properties of the clouds, and their impact on the temperature, is discussed further in Urata and Toon (2012b).

Figures 2.5a-2.5e show the same fields as the previous plots for L_s=90°. As was the case for L_s=0°, the structure of the atmospheric temperature field is almost the same for each dust concentration, but temperatures rise with higher amounts of dust. The temperatures northwards of 30° S are nearly constant along constant pressure surfaces, while southwards of that latitude there is a sharp temperature gradient along the isobars. Examining the temperature comparison plots, Fig. 2.5d and 2.5e, shows the best matching case is τ_{dust} = 0.3, where the temperature difference is typically within +/-5 K between the latitudes of 60° S and 60° N. The higher dust concentration simulations show model temperatures that are warmer, due to the additional radiative heating from the dust.

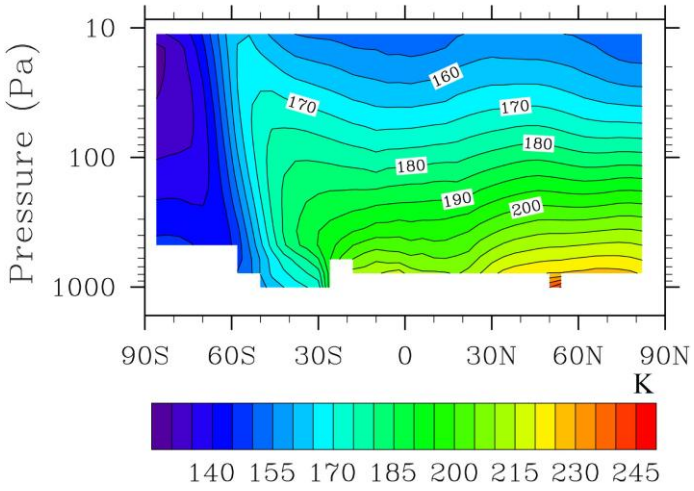

Figure 2.5a. Zonally averaged temperatures at L_s=90° for TES.

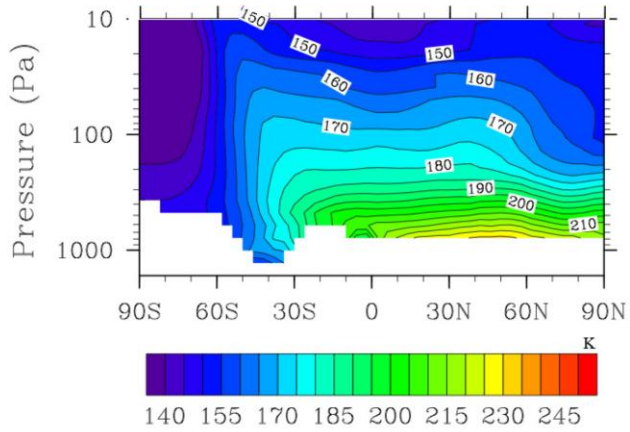

Figure 2.5b. Zonally averaged temperatures at L_s=90° for τ_{dust}=0.1 between 1065-1108 cm^{-1}.

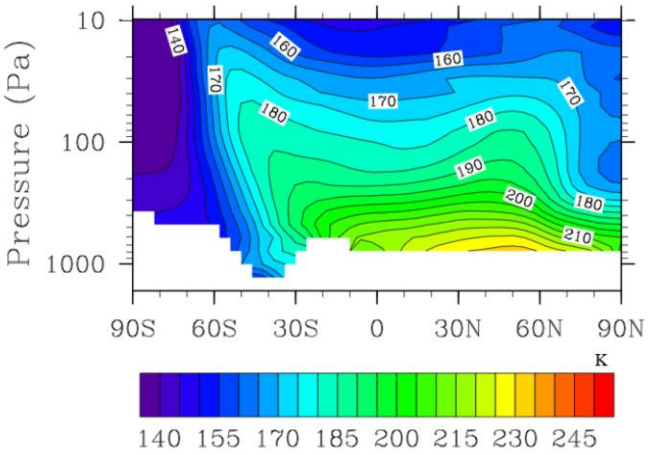

Figure 2.5c. Zonally averaged temperatures at L_s=90° for τ_{dust}=0.3 between 1065-1108 cm^{-1}.

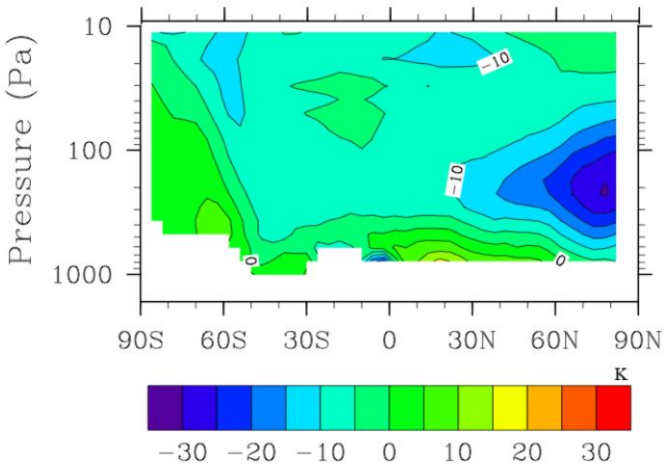

Figure 2.5d. Zonally averaged temperatures at L_s=90° for Model – TES temperature difference for τ_{dust}=0.1.

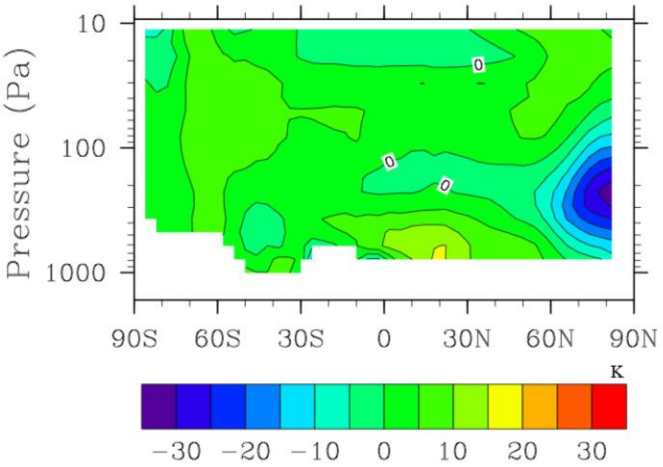

Figure 2.5e. Zonally averaged temperatures at L_s=90° for Model – TES temperature difference for τ_{dust}=0.3.

Comparisons between the TES temperature retrievals and the model output show a general agreement to within 10-15 degrees. The temperature is quite sensitive to the atmospheric dust content, and can increase by 15-20 K as τ_{dust} varies from 0.1-0.3. During the equinox season, L_s=0°, the largest differences occur at Northern latitudes poleward of 45 degrees where the model is warmer than the data, and at high altitudes

above the equator where the model is cooler than the data. The LMD model has implemented dust profiles that vary spatially in latitude as well as temporally in L_s (Montmessin et al., 2004). Using such a dust profile may improve the model results, however a better alternative would be to use the interactive dust model available in CARMA. Clouds also affect the temperature profile, and offset some of the larger differences noted in the simulations here, as further discussed by Urata and Toon (2012b). An additional possible source of error might be the reduction of high latitude dust by a factor of 10. While not included in the plots, simulations done with the same amount of dust at all latitudes caused extremely warm polar temperatures, which were reduced by decreasing the polar dust. However it is possible that the factor of 10 was too large, causing the very cool polar temperatures in the model.

2.3.3 1-D Vertical temperature profiles

In this section, we compare vertical temperature profiles from the same two seasons as in the previous section, northern spring equinox, and northern summer solstice. For the comparison, we chose daytime (red dash line) and nighttime (blue dash-dot line) temperature profiles from the TES data and plot 1-D temperature profiles from the model at the same location. In each case, we take data from locations closest to (20°, 0°) in latitude and longitude. This location was chosen because both day and night temperatures were available in the dataset, it is far from the poles so that polar influences are small, and far from sharp topographic changes to avoid orographic phenomena. Results have been taken from simulations with τ_{dust}=0.3, which gave the best agreement to

observations at low latitudes. In the L_s=0° case (Fig. 2.6), the model is within 5 K of the TES measurements throughout a majority of the atmosphere during the day (solid black line), but there is an increase in the lapse rate near the 20 Pa level causing the high altitude observed temperatures to be colder than the data. At higher altitudes, the model temperatures are up to 15 K lower than the data. The temperatures near the surface are also slighty too warm, possibly because of too much dust in the atmosphere. The nighttime temperatures (black dash-dot line) are within 5 K of the observations from the surface up to 50 Pa, and become slightly cooler than observations by 10 K at the 10 Pa level. Possibly clouds, not considered in this model, would warm the upper atmosphere (Uratra and Toon, 2012b). We discuss surface temperatures below.

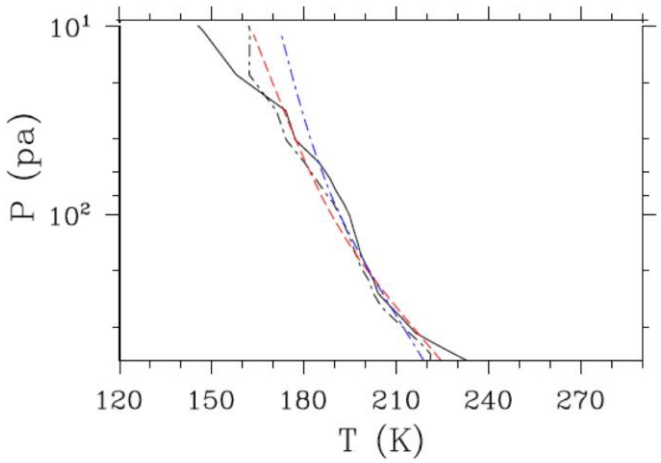

Figure 2.6. Day (black solid) and night (black dash-dot) vertical temperature profiles for (20°N, 0°W) at L_s=0° compared to TES day (red dash) and night (blue dash-dot). τ_{dust}=0.3.

In the L_s=90° plot (Fig. 2.7), the model profile is less smooth than the data. However, the model profile is within +/- 5 K of the TES data, except for the uppermost levels, where the model can be up to 15 K cooler, and near the surface where the model is

up to 25 K warmer. Similar to the data, the model day and night temperatures are very close to each other throughout the atmosphere, but diverge near the surface.

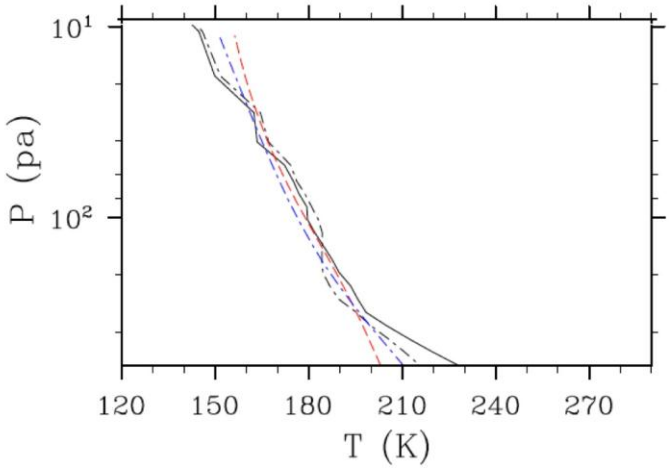

Figure 2.7. Day (black solid) and night (black dash-dot) vertical temperature profiles for (20°N, 0°W) at L_s=90° compared to TES day (red dash) and night (blue dash-dot). τ_{dust}=0.3.

Plots of the vertical temperature show that the model predicts the low latitude atmospheric temperature to within +/- 5 K for most of the atmosphere. There appears to be an issue in the model at high altitudes being significantly cooler than the data. The specific cause of this has not been determined. However, recent investigations show that there could be a significant amount of clouds present at these altitudes. The clouds are not radiatively active in these simulations. This impact of the clouds will further be investigated in the companion paper, which focuses more on the Martian water cycle.

2.3.4 The Surface Diurnal Temperature Cycle

In 2004, the Mars Exploration Rover Opportunity landed at Meridiani Planum on the surface of Mars at the coordinates (1.95°S, 5.53°W). In their 2006 paper, Smith et al. reported diurnal temperatures retrieved from the Mini-TES instrument aboard the rover. Figures 2.8 and 2.9 compare the simulated surface and near surface temperatures to the observed temperatures reported by Smith et al. The temperatures reported come from L_s = 75°-105°, Northern Hemisphere summer, the aphelion season. These temperatures are therefore averaged over more than two terrestrial months. We similarly averaged the model data. The error bars indicate the variability over this time period. Smith et al. (2006) also include a plot from the perihelion period of L_s = 225°-255°, but we have neglected these temperatures due to high atmospheric dust concentrations during this time. Unfortunately, the rover does not report nighttime temperatures, so we are not able to make a full diurnal comparison with the rover data.

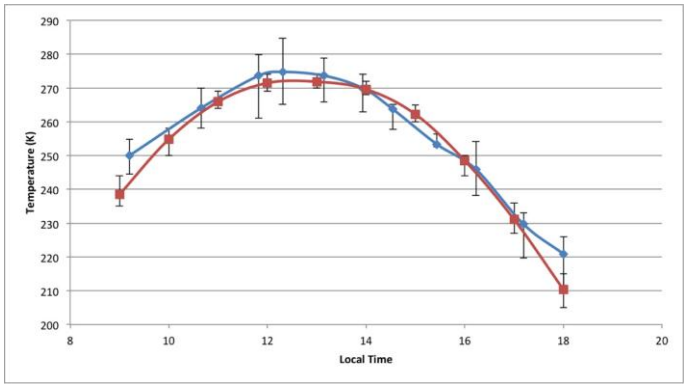

Figure 2.8. Model daytime surface temperature (red) compared to Opportunity observations (blue) for L_s = 75°-105°.

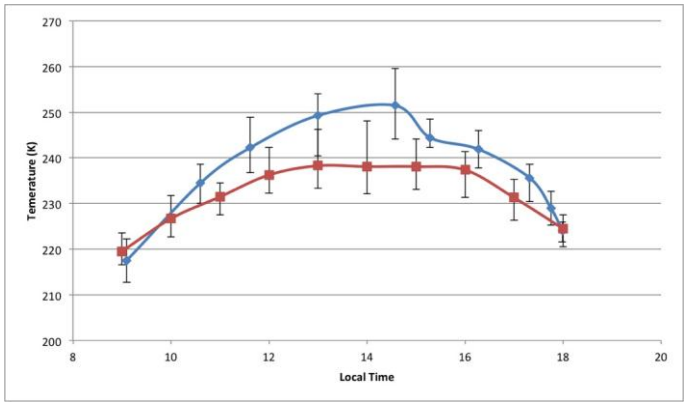

Figure 2.9. Model daytime 1 m temperature (red) compared to Opportunity observations (blue) for L_s = 75°-105°.

Figure 2.8 shows a comparison between the model and data for the temperature of the ground during the day, assuming a dust optical depth of 0.3 in the model. The error bars represent the variation in measurements over the season. The ground temperature comparison plot shows agreement to within the error bars between the model and data throughout most of the day. The model is colder than the data in the morning and late afternoon. The largest difference in the surface temperatures is approximately 10 K, which occurs at 1800 local time. Possibly these temperature differences are caused by too much dust in the model, or by an inaccurate representation of heat transfer next to the ground.

Figure 2.9, shows that the model temperatures at a height of 1 m are closest to the rover temperatures in the early morning or near dusk, and furthest at midday. Figures 2.8 and 2.9 show that the atmosphere 1 m above the surface is much colder than the ground, so that the lapse rate is significantly superadiabatic throughout much of the day. Although the model contains parameterizations to calculate the temperatures in the unstable boundary layer near the surface, they depend on values such as the local surface roughness; differences in which can lead to disagreements with the measurements. As the

surface properties in the model represent an average over a large area, and the rover measures local values, differences in surface albedo and thermal inertia may also lead to variations in temperature. The surface albedo and thermal inertia values from data and the model are given in Table 2.5.

Parame-ter	Opportun-ity (Opp.)	VL-1	VL-2	Model (Opp.)	Model (VL-1)	Model (Alt. VL-1)	Model (VL-2)	Model (Alt. VL-2)
Location	(1.95°S, 5.53°W)	(23°N, 48°W)	(48°N, 226°W)	(2°S, 5°W)	(22°N, 45°W)	(22°N, 105°W)	(50°N, 225°W)	(50°N, 120°W)
Season	L_s = 75°-105°	L_s = 98°	L_s = 120°	L_s = 90°	L_s = 98°	L_s = 98°	L_s = 120°	L_s = 120°
Surface albedo	0.13	0.26	0.225	0.13	0.2	0.3	0.22	0.28
Thermal inertia	220	215	240	211.7	302.1	55	231.1	120

Table 2.5. Surface properties at lander sites and corresponding model coordinates.

We have done similar temperature comparisons for the two Viking Landers. Viking Lander 1 is situated at (23°N, 48°W), and Viking Lander 2 at (48°N, 226°W). The measurements were made near L_s = 100°, and L_s = 120° for Viking Lander 1 & 2 respectively. The corresponding closest model grid-cells for the two landers are at (22°N, 50°W), and (50°N, 225°W). Figures 2.10 and 2.11 compare the model 2-meter diurnal temperatures to the 1.6 meter Viking Lander 1 and 2 temperatures respectively.

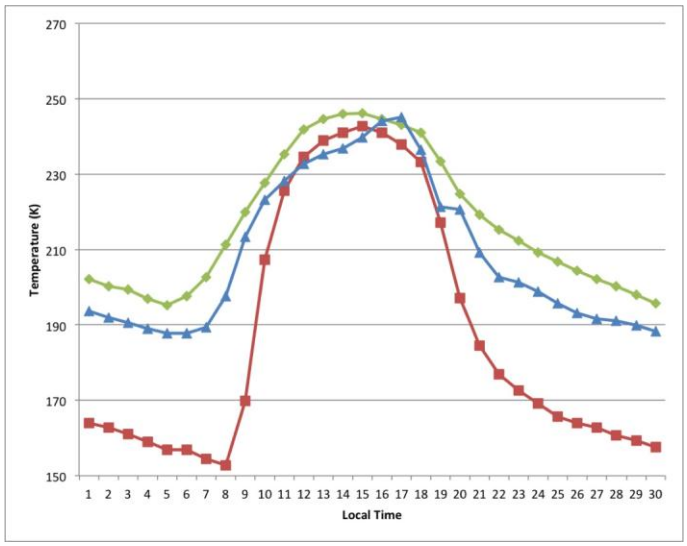

Figure 2.10. Model 2 m diurnal temperature cycle (green) compared to Viking Lander 1 observations (blue). The red line is the model temperature cycle at the same latitude, but lower thermal inertia.

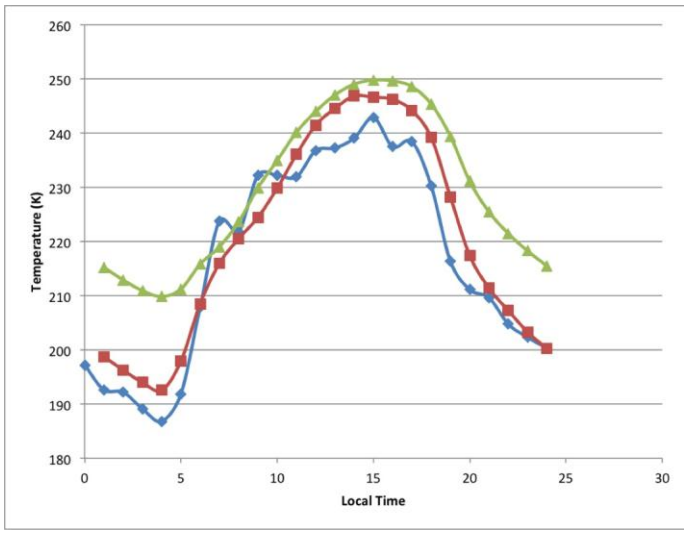

Figure 2.11. Model 2 m diurnal temperature cycle (green) compared to Viking Lander 2 observations (blue). The red line is the model temperature cycle at the same latitude, but lower thermal inertia.

The Viking Lander temperatures are denoted by blue diamonds, and the model temperatures by green triangles. The red squares are the model 2-meter temperatures for a location at the same latitude, but with higher surface albedo, and lower thermal inertia to

show the possible impact that these values can have on the near surface temperature. Table 2.5 includes the albedo and thermal inertia values (Haberle et al., 1993) of these locations for comparison. In the Viking Lander 1 comparison plot (Fig. 2.10), the model temperatures are between 0-5 K higher during most of the day except at midday, when the model is up to 15 K warmer. These differences are probably due to the albedo used in this grid cell being lower than that at the Viking sites (Table 2.5). Similarly, in the Viking Lander 2 comparison plot (Fig. 2.11), the model is consistently higher than the Viking Lander 2 measurements during the daytime by as much as 10 K, probably because of the albedo for the grid cell containing the Viking lander site being lower than the actual albedo at the site. The model is warmer than either Lander at night by 10-15 K. There is a strong temperature inversion near the surface during the night, and the model may have difficulty finding the 2-meter temperature due to the atmosphere being highly stable. However, comparison between the model simulations at two different longitudes, show that the nighttime temperatures are very sensitive to the thermal properties of the soil. Hence the specific values at the lander sites, which differ from the grid cell average values used in the model, are the most likely cause of the differences between observed and modeled temperatures.

While TES data cannot be used to chart the complete diurnal surface temperature cycle, it provides a daytime and nighttime snapshot of the planet's surface temperature. Figures 2.12 and 2.13 show the daytime and nighttime model surface temperatures, and difference plots of the model surface temperature and the TES surface temperature. We include comparisons at L_s=0° and L_s=90°, the equinox and northern summer solstice because these two times of year represent turning points in the Martian seasonal cycle.

We chose a dust optical depth of 0.3 for these comparisons, as the atmospheric temperatures most closely matched data with this value.

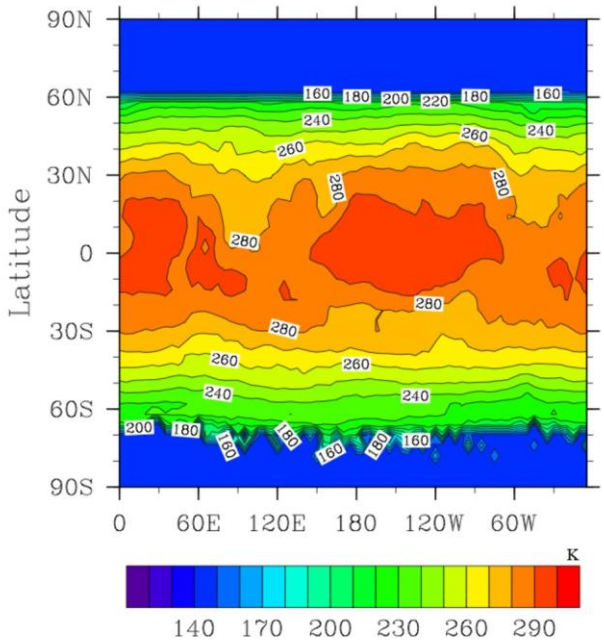

Figure 2.12a. Model daytime surface temperature at L_s=0°.

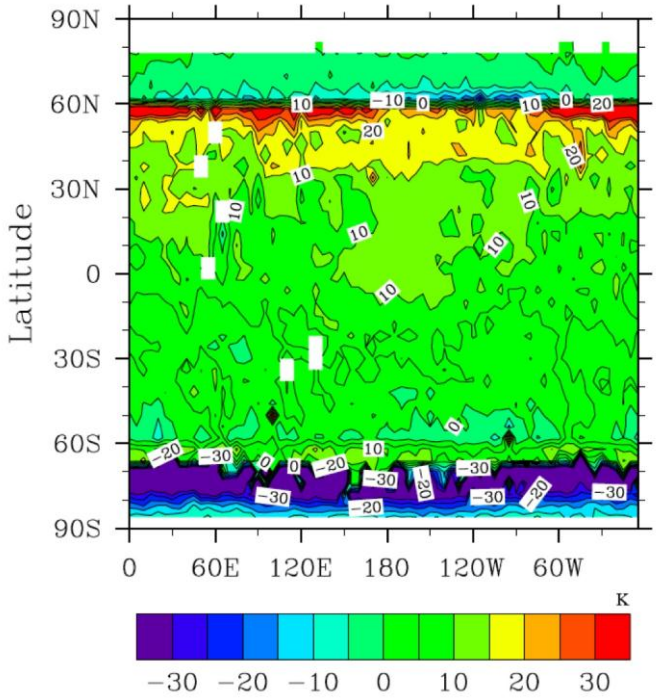

Figure 2.12b. Model – TES daytime surface temperature difference.

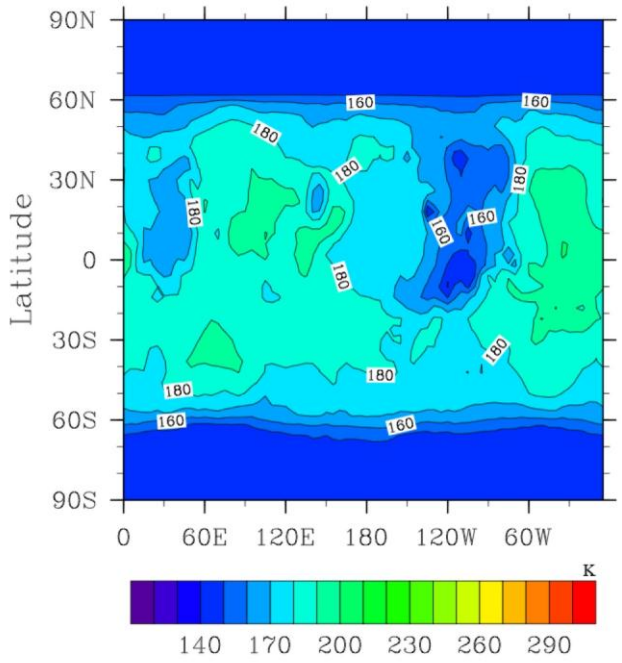

Figure 2.12c. Model nighttime surface temperature at L_s=0°.

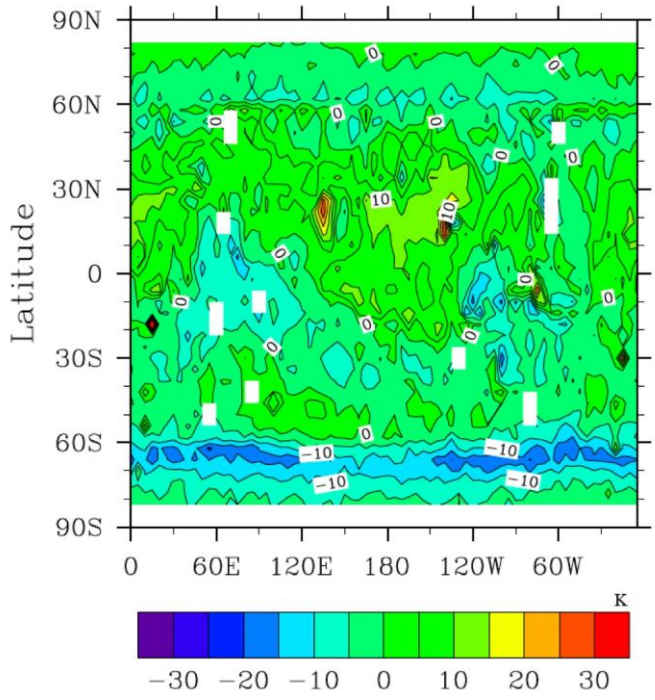

Figure 2.12d. Model – TES nighttime surface temperature difference.

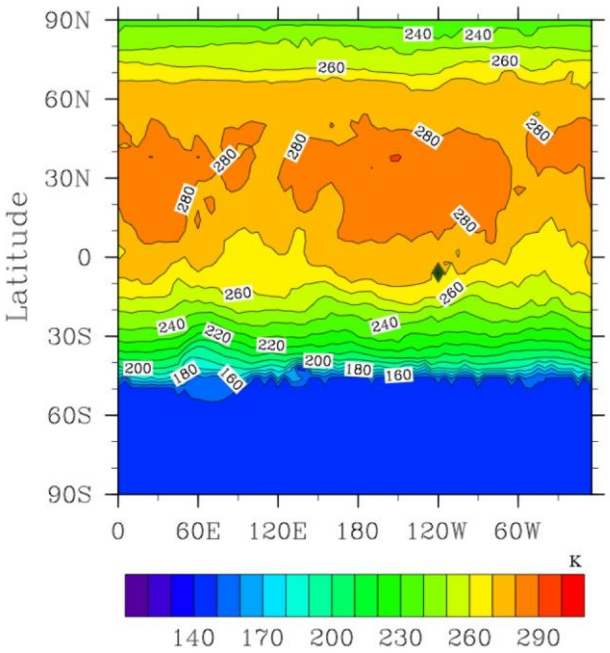

Figure 2.13a. Model daytime surface temperature at L_s=90°.

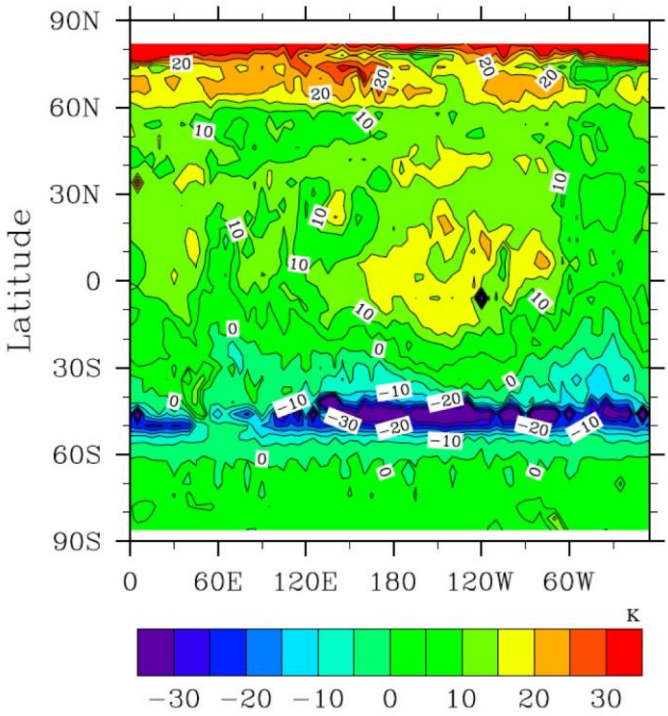

Figure 2.13b. Model – TES daytime surface temperature difference.

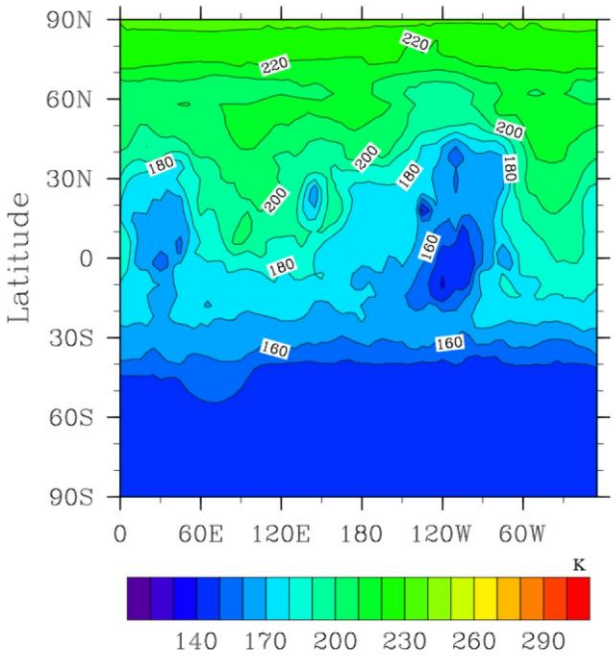

Figure 2.13c. Model nighttime surface temperature at L_s=90°.

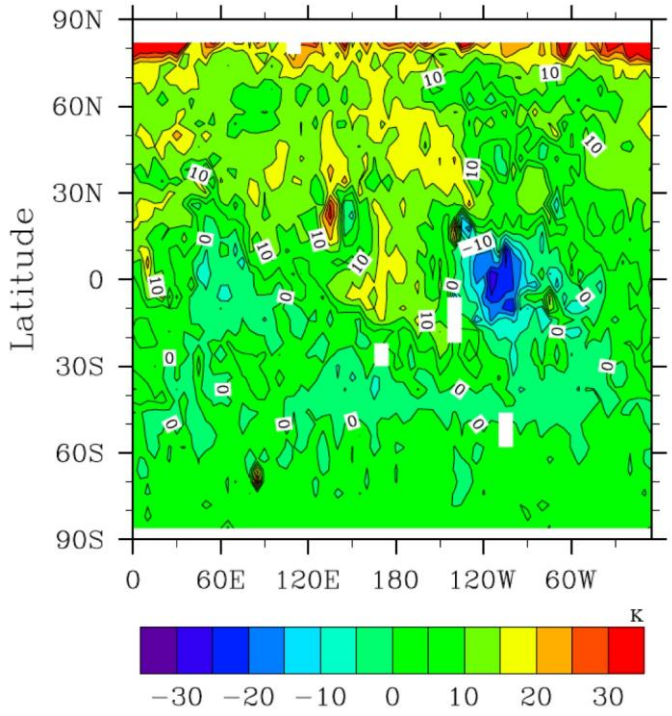

Figure 2.13d. Model – TES nighttime surface temperature difference.

During the day at L_s=0° (Fig. 2.12a, 2.12b), the model is within 5-10 K of the daytime data throughout the southern hemisphere and the low northern latitudes, but tends to be warmer by up to 20-30 K in some locations in the northern hemisphere. There is a sharp boundary at 60°N, representing the extent of the seasonal CO_2 cap. Differences near this boundary may be due to the model cap not extending down to the same latitudes as in the data. During the night (Fig. 2.12c, 2.12d), the difference is less pronounced, and the temperatures are within 5-10 K at almost all locations. Model daytime temperatures at L_s=90° (Fig. 2.13a, 2.13b) are typically within 10-15 K of the measurements, except for a band between 40°-50° S, where the model is colder than the measurements by 20 K or more. These latitudes represent the extent of the southern CO_2 cap, and the cold model temperatures indicate that the model cap is slightly larger than the observations. During the night (Fig. 2.13c, 2.13d), the agreement is better, and the latitude band of colder temperatures does not exist.

2.3.5 Annual Pressure Cycle

A large percentage of the atmosphere condenses onto the winter pole every year, which is evident in the annual pressure cycle. The two Viking Landers measured the local annual surface pressure cycles to within 10 Pa, over multiple Martian years. Figure 2.14 compares the observed annual pressure cycles at the two sites from the second and third Viking years to the pressure cycles at corresponding locations in the model, assuming a constant dust optical depth of 0.3 year-round.

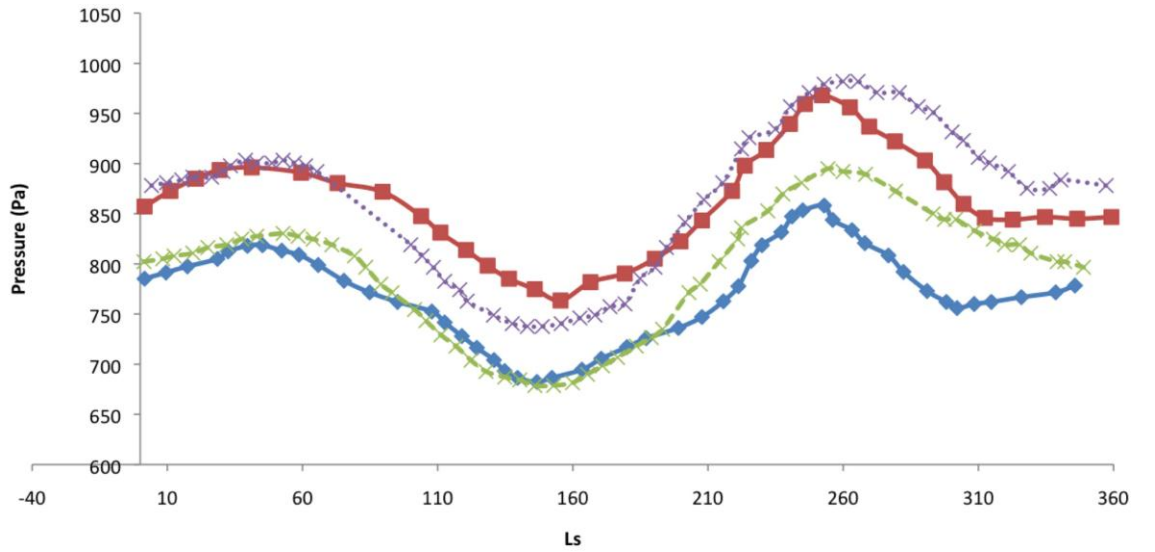

Figure 2.14. Comparison of model simulations and Viking Lander observations for the annual pressure cycle. Model data are marked by the red line for the VL-1 site, and blue line for the VL-2 site. The green line designates VL-1 observations, and the purple line is VL-2.

The data plotted came from Murphy et al., (1990). Two peaks and two troughs, roughly corresponding to the solstices and equinoxes, characterize the annual cycle. The L_s=60° pressure maximum and L_s=160° minimum are lower than the values at L_s=250° and 320°. This difference is related to the eccentricity of the orbit, and the southern hemisphere's winter being longer and cooler than the northern hemisphere's, which results in an increased amount of carbon dioxide condensation in the Southern Hemisphere winter and spring. This increased condensation leads to a global decrease in pressure that is larger in amplitude compared to northern winter through northern spring equinox. The model also shows two distinct peaks and troughs during the year, and generally follows the data to within 50 Pa. The difference between model and data is most noticeable between L_s = 250°-360°, corresponding to southern summer leading into fall. During this time, the model underestimates the surface pressure by up to 100 Pa. The model prediction of more

carbon dioxide condensation than what actually occurs could have a number of causes including incorrect polar albedos, incorrect polar heat transport, or failure to consider the radiative properties of increased dust activity or clouds during southern summer and fall. This season also marks the time when global dust storms may occur, however the data were chosen from non-global dust storm years, so the differences are unrelated to global dust storms. Although there are no global dust storms, dust activity is higher during this season compared to the rest of the year, and would lead to less carbon dioxide condensation in the north. Some other models (Pollack et al., 1993) produced similar underestimations of the surface pressure, but were able to match the Viking Lander curves by using time-variable dust distributions throughout the year.

2.3.6 Convective Boundary Layer

The planetary boundary layer (PBL) plays a significant role in the Martian climate, because exchanges of energy, momentum, dust and volatiles between the surface and atmosphere occur through this layer. During the day, when the surface heating causes the lower most part of the atmosphere to become unstable, the boundary layer become convective (CBL). This is of particular interest because it provides vertical transport of heat and momentum, which strongly influence the structure and circulation of the atmosphere. In contrast, the PBL is stable during the night, when the surface is cooler than the adjacent air. Hinson et al. (2008) used radio occultations from Mars Express to measure the depths of the CBL at different locations, between L_s = 34.7°-69.2°. An

interesting conclusion of their study is that the boundary layer depth depends strongly on elevation of the surface.

Ls	Lat.	Lon. (east)	Hinson CBL (km)	Ground Elevation (km)	CAM Lat.	CAM Lon.	CAM CBL (km)	CAM Ground Elevation (km)
34.7	53.6	206.3	2.6	-3.6	54	205	2.5	-3.80
35.1	52.5	271.7	5.4	-1.7	50	270	5	-0.83
39.6	39.5	336.7	4.4	-4.5	38	335	4.4	-4.41
40.5	37.3	9.4	5.7	-2.5	38	10	5.1	-2.53
44.5	27.5	107	4.6	-4.3	26	110	5	-4.25
45.9	24.4	106.9	5.6	-3.9	26	105	5.3	-4.07
47.1	21.8	205	5.1	-3.8	22	205	3.3	-3.86
47.8	20.6	74	10	-0.3	22	75	5.1	-0.21
48.4	19.3	303	7.8	-0.9	18	305	5.4	-1.53
48.8	18.6	8.4	8.8	-1.5	18	10	8.6	-1.67
49	18	172	7.5	-2.9	18	170	7.5	-2.70
49.1	17.8	73.8	9.3	-0.6	18	75	5.1	-0.91
49.2	17.5	335.6	6.5	-3.2	18	335	5.3	-2.88
49.4	17.4	237.5	7.9	0.9	18	235	6	0.90
51.2	13.7	204.6	4.2	-3.5	14	205	6	-3.65
51.5	13.3	8.2	7.3	-1.8	14	10	8.5	-1.28
51.6	13.3	270	8.9	1.8	14	270	8	1.76
52.1	12.3	237.2	8.2	2.4	14	235	6.9	1.37
53.3	10	335.3	5.7	-2.4	10	335	5.9	-2.54
53.7	9.5	40.7	7.8	0.5	10	40	6.8	0.52
53.8	9.2	302.5	9.2	-0.5	10	300	8.5	-0.45
54.1	8.8	106.1	8.8	-0.5	10	105	7.9	-1.14
54.3	8.4	269.8	9.5	1.9	10	270	9	1.83
57.4	3.3	335	6.1	-2.8	2	335	6.9	-2.05
58.2	2	7.7	3.8	-1	2	10	9.5	-0.72
58.5	1.5	171.3	5.4	-3	2	170	7	-2.97
58.6	1.5	73.1	9.8	1.3	2	75	9.8	1.16
60.5	-1.3	40.3	5.3	0.9	-2	40	10.1	1.17
60.8	-1.9	105.7	4.1	-0.2	-2	105	9	0.18
61.3	-2.5	73	8.3	1.9	-2	75	10	1.46
62.2	-3.9	105.6	5.2	-0.1				
63.9	-6.4	171	3.9	-2.9	-6	170	9	-2.63
64.8	-7.6	203.8	5.3	-0.9	-6	205	10.2	-1.08
64.9	-7.7	105.6	4.9	0.9	-6	105	9.8	0.75
65.2	-8.3	171	4.9	-2.8				
67	-10.2	236.6	9.9	8.7	-10	235	10.1	6.83
67.9	-12.1	170.7	3.1	-1.9	-10	170	10.2	-2.18
69.2	-13.5	268.9	6.5	5.5	-14	270	7.9	5.03

Table 2.6. Boundary layer depth comparisons.

Table 2.6 contains a summary of the boundary layer depths from Hinson et al. (2008), and the boundary layer depths from the model at the corresponding locations and times. Figure 2.15 plots the boundary layer depths versus the local elevation for both the model and observations, including a trend line. Figures 2.16a and 2.16b show a comparison between the observed values and the model values for the boundary layer depths and surface elevations, with a 1:1 line.

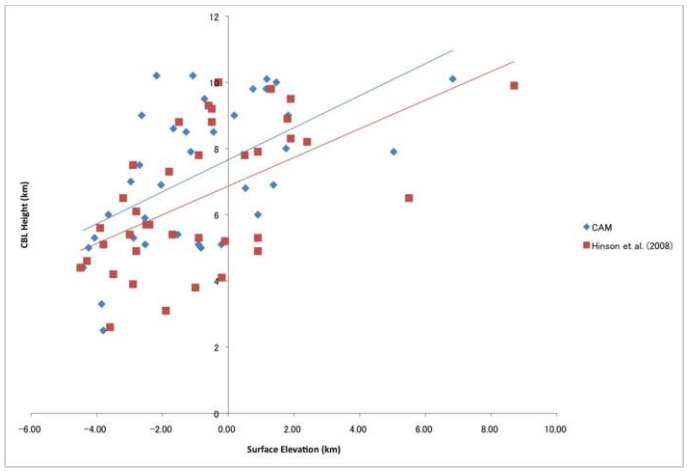

Figure 2.15. Boundary layer depth versus surface elevation for the model (blue) and observations (red) with trend lines.

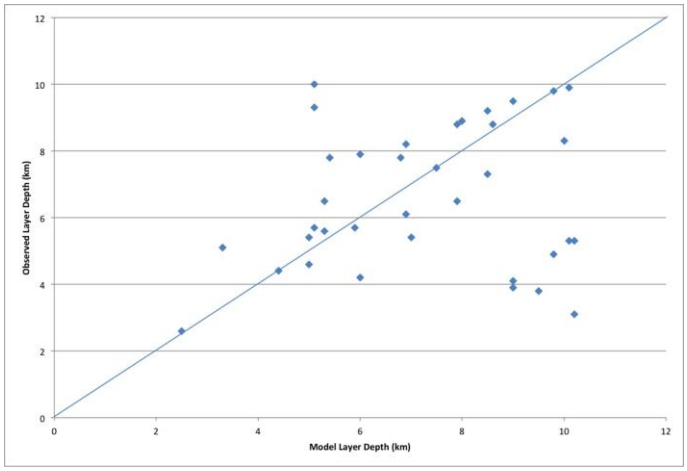

Figure 2.16a. Observed boundary layer depth vs. model predicted boundary layer depth with a 1:1 line.

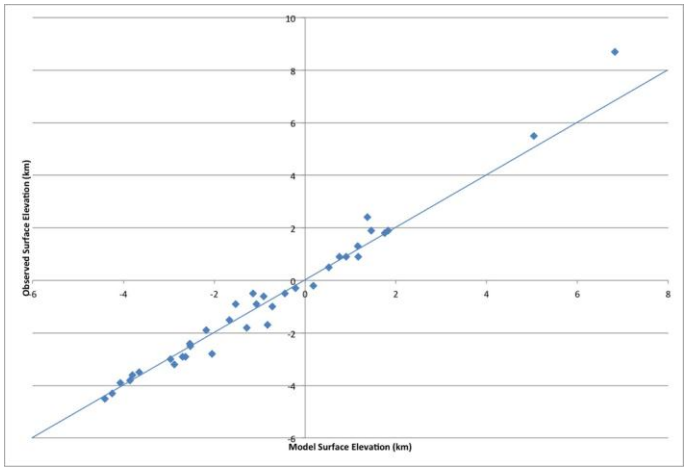

Figure 2.16b. Observed surface elevation vs. model surface elevation with a 1:1 line.

In most cases, the model predicts the observed boundary layer depths to within a kilometer; however there are a few outlying cases where the model and observations differ by 4-5 km. In general, the model tends to overestimate the boundary layer depth by an average of 600 meters, which is roughly a third of a model layer at 8 km. However, the observed trend of the boundary layer being deeper at higher elevations is found in the model as well as the data.

The cause for this trend has been called the "pressure effect," referring to the dependence of the potential temperature evolution on pressure (Spiga et al., 2010). The first law of thermodynamics can be used to define the potential temperature as

$$\theta = T(P_0/P)^{R/cp} \quad (2.6)$$

where T is the temperature, p_0 is some reference pressure, p is the pressure, R is the gas constant of air, and c_p is the specific heat of air. Using Eq. (2.6), the thermodynamic

equation can be expressed in terms of the potential temperature as (Salby, 1996, section 10.7)

$$\rho c_p \, d\theta/dt = \Pi^{1} \, (LW + SW + LH) + \rho c_p \kappa_T \nabla^2 \theta \quad (2.7)$$

where $\Pi=(p/p_0)^{R/Cp}$ is the "dimensionless pressure," ρ is the air density, LW is the divergence of the net longwave radiative flux, SW is the divergence of net shortwave radiative flux, LH is the net latent heating, and κ_T is the thermal eddy diffusivity ($\kappa_T=k_T/\rho c_p$; k_T is the thermal conductivity of air). The last term on the right hand side of Eq. (2.7) represents the net heating due to eddy diffusion. By applying a Reynolds decomposition to first order and averaging, the eddy diffusion term reduces to the divergence of the vertical eddy heat flux:

$$\overline{w'\theta'} = -\kappa_T \partial\overline{\theta}/\partial z \quad (2.8)$$

Evaluated at the surface, this can be related to the sensible heat flux, H_0:

$$H_0 = -\rho_0 c_p (\overline{w'\theta'})_0 \quad (2.9)$$

Due to the low density of the Martian atmosphere (approximately a factor of 150 smaller at the surface than Earth), the sensible heat contribution to the surface energy budget is small compared to the radiative heating (~2% of the incoming solar flux; Sutton et al., 1978). This is in contrast to Earth, where the sensible heat can make up a significant portion of the heat budget in arid regions during the day (Businger et al., 1971). The low specific humidity found on Mars also means that the latent heating is small. Therefore, the Martian surface temperature cycle is predominately driven by the equilibrium between the radiation and soil heat conduction. In this case, if the soil properties of two locations are similar, their surface temperatures will also be similar, despite any differences in surface pressure. It also follows from Eq. (2.7) that if the radiative terms in

the two locations are similar, then the potential temperature will be controlled by the dimensionless pressure, and a lower pressure will correspond to a higher potential temperature near the surface.

The boundary layer depth is dependent on the surface pressure because the heating is dominated by the radiative terms in the energy balance. However, whether or not the boundary layer depth increases with surface elevation will depend on other environmental factors such as the lapse rate of the free atmosphere, and the surface potential temperature difference between the two locations. More specifically, if the potential temperature lapse rate of the free atmosphere is smaller than the surface potential temperature variation with pressure, then the boundary layer depth will increase with surface elevation.

2.4 Conclusions

We have developed a new general circulation model for Mars from the Community Atmosphere Model developed by NCAR. The major modifications made to the model include the addition of a carbon dioxide condensation and sublimation scheme at the surface, and the replacement of the radiative transfer scheme with one that is more appropriate for Mars. Most of the original model physics has been left unmodified except for replacing the physical parameters such as gravity at the surface with corresponding Martian values.

In this paper, we compared model simulation results for various fields including temperature, pressure, and boundary layer height to spacecraft data. These comparisons

show that the model reproduces the modern Martian climate conditions to within the uncertainty related to dust concentrations. The atmospheric temperature profiles are generally within 10-15 K, and boundary layer heights usually to within ten percent. Daytime surface temperatures match Mars Exploration Rover observations, and the near-surface temperatures agree with Viking Lander measurements to within 5-10 K. Because temperature and boundary layer height can change greatly with local conditions, perfect agreement is not expected. Each of these comparisons is sensitive to the amount of dust present in the atmosphere, as we have shown. Many of them are also sensitive to the presence of clouds as discussed by Urata and Toon (2012b).

Based on these results, we conclude that the model is useful for simulating the Martian climate in 3 dimensions, and can be a helpful tool for investigations of the lower atmosphere. The model contains a complete microphysical package and could be extended to higher elevations or be used for atmospheric chemistry studies by attaching other standard components of the NCAR modeling suite, but these functionalities are not described here. In a companion paper, we use the model to examine the current and past water vapor and cloud cycles on Mars, and the effects of a thick, wet atmosphere on the ancient climate. The present model has been placed on the NCAR extraterrestrial CAM wiki page (https://wiki.ucar.edu/display/etcam/Extraterrestrial+CAM), and can be downloaded freely by any interested user.

Chapter 3. Simulations of the Martian hydrologic cycle with a general circulation model: Implications for the ancient Martian climate

3.1 Introduction

The Martian hydrologic cycle is often overlooked because water has very little impact on the current global climate compared to dust. Spacecraft observations show the presence of water-ice clouds on Mars (Kahn, 1984; Wang and Ingersoll, 2002), however these clouds tend to have low opacities. Because these clouds are so tenuous, precipitation is limited, and latent heating is very small compared to radiative heating (Savijarvi, 1995) or latent heating from carbon dioxide condensation. Water vapor is only present in trace amounts, and also makes little contribution to the atmospheric radiative heating compared to carbon dioxide or dust. However, despite its minimal influence on the current Martian climate, water is of great interest due to its importance to life, and because the water cycle was clearly much different in the early history of Mars when there were rivers, lakes, and possibly oceans.

In this paper we first consider the current water vapor cycle on Mars, and show that we can simulate it reasonably well. We then examine the hydrological cycle on Mars

when the solar luminosity was less than now. We find that the Martian climate has two stable states as previously suggested by Segura et al. (2008). One of these states is similar to the present climate of Mars, with low surface temperatures and low cloud and water amounts. The other state has strong greenhouse warming that is mainly contributed by high altitude cirrus clouds. This state has portions of the surface with annual average temperatures above freezing. Precipitation rates are moderately high in some of these simulations.

3.2 The present Martian hydrologic cycle

3.2.1 Observations

Multiple observations of the annual water vapor cycle have been provided by various spacecraft instruments including the Mars Atmospheric Water Detector (MAWD) on Viking (Farmer et al., 1977; Jakosky and Farmer, 1982), the Thermal Emission Spectrometer (TES) on the Mars Global Surveyor (Smith et al., 2001, 2004), the Compact Reconnaissance Imaging Spectrometer (CRISM), and the Mars Climate Sounder (MCS), the latter two both aboard the Mars Reconnaissance Orbiter (MRO) (Smith et al., 2009; McCleese et al., 2007). These investigations have pointed to spring time evolution of water vapor from the warming polar cap, followed by transport to lower latitudes.

A number of other studies have focused on clouds, which can be tracked in images from the Mars Orbital Camera (Wang and Ingersoll, 2002), and through other

observations such as those made by TES (Smith et al., 2001). Such studies have revealed two distinct seasonal cloud formations. The first type of these seasonal clouds tends to form during the northern spring and summer at low latitudes. These clouds, first identified by ground observations (Clancy et al., 1996), are often referred to as the "equatorial cloud belt," or alternatively as the "aphelion cloud belt" because they form during the aphelion season. The other type of clouds, referred to as the "polar hoods," tend to form at mid to high latitudes towards the end of summer, and persist through winter (Leovy et al., 1972). Detailed observations of the polar hoods have been limited until recently (Horne and Smith, 2009), due to the difficulty in obtaining retrievals over cold surfaces for TES (Smith, 2004), or the absence of sunlight for MOC images (Wang and Ingersoll, 2002).

Spacecraft observations of the annual hydrologic cycle include zonally averaged water vapor column versus time (Jakosky and Farmer, 1982; Smith, 2008; Smith et al., 2009), and water-ice opacity maps versus time (Smith, 2008). These observations show a globally averaged water vapor column abundance of approximately 10 precipitable microns (pr-μm), with a maximum above 60°N ranging between 50-75 pr-μm at around L_s=120°. For this work, we examine the conditions necessary to replicate the TES data. Particularly of interest is the observation of high water vapor abundance concurrent with low water-ice cloud optical depths at high latitude during the northern summer.

3.2.2 Previous modeling of the hydrological cycle

Modeling of the role of clouds in the Martian hydrologic cycle began with work by James (1990) who used a 1-D model to show that water-ice clouds play an important role in the transport of water from north to south. Richardson and Wilson (2002) and Richardson et al., (2002) performed the first study of the hydrologic cycle using a 3-D general circulation model (GCM) with the Geophysical Fluid Dynamic Laboratory (GFDL) Mars GCM. While their simulations resulted in a climate significantly wetter than the Viking MAWD observations, they were able to identify some key factors governing the hydrologic cycle, such as the small effect that a water reservoir in the regolith has, and that the southern residual polar cap should act as a cold trap for water. Mischna et al. (2003) used the same model to look at the hydrologic cycle as a function of orbital parameters such as eccentricity and obliquity. They found that the stability of surface ice is closely linked to the obliquity of the planet, and that the latitude of stable surface ice moves equatorward as the obliquity is increased with a preference toward the hemisphere with aphelion summer, a result anticipated in some of the earliest studies of Martian climate change (Toon et al., 1980). Montmessin et al. (2004) used a 3-D GCM developed at the Laboratoire de Meteorologie Dynamique to simulate the role of water-ice clouds in the hydrologic cycle. In their paper, they were able to reproduce the observed hydrologic cycle by predicting cloud particle sizes depending on the concentration and size of dust particles, which act as the nucleation cores. Most recently, Haberle et al. (2011) used the NASA Ames Mars GCM to simulate the effect of radiatively active water-ice clouds. Their preliminary results indicate that allowing clouds to be radiatively active could warm the upper tropospheric temperatures by as much as 10 K during summer, and cool the low polar atmospheric temperatures also by as much as

10 K during winter compared to the non-radiatively active cloud case. The reason this occurs is that during summer, the clouds are high and cold, and therefore trap the upwelling infrared radiation from the surface. In contrast, the polar hoods tend to form low in the atmosphere, and because the clouds are efficient radiators, they tend to locally cool the atmosphere. This effect is also observed in the polar stratospheric clouds on Earth (Pollack and McKay, 1985). A simplified explanation can be given by performing an energy balance between the surface and the cloud (Pollack and McKay, 1985). The cloud is warmed by upwelling radiation from the surface, and cooled by emission by the cloud in both the upwards and downwards direction. The energy balance will then be:

$$\text{Net heating} = e_c \sigma T_g^4 - 2 e_c \sigma T_c^4 \quad (3.1)$$

Here, e_c is the infrared cloud emissivity, σ is the Stefan-Boltzmann constant, T_g is the ground temperature, and T_c is the cloud temperature. This will lead to cloud warming if $T_c < T_g/2^{1/4}$, and cooling for the opposite case.

While allowing clouds to be radiatively active improved the predicted atmospheric temperatures in the Haberle et al (2011) model, they also found that this tended to dry the model. The cause was a thick cloud layer forming over the northern pole during the summer, which tended to lower the surface temperature to the point where the sublimation rate of water was significantly reduced. Such clouds are not observed during this season, indicating that some other microphysical process is important to include to properly simulate cloud formation over the pole during this time of year.

3.2.3 The ancient Martian climate

Since the first observations of the extensive valley networks on Mars in the early 1970's, there has been much debate as to their origins. These valley networks are believed to have formed near the end of the Noachian around 3.75 billion years ago (Fassett and Head, 2008). Studies show that a significant amount of runoff would have been required to form such networks (Hynek and Phillips, 2001, 2003), but the source of the water is unknown. The age of the valleys along with the amount of runoff required to form them has been used to support the idea of an ancient warm, wet Mars. A popular idea is that early in the Martian history the climate was warm enough to sustain liquid water on the surface for an extended amount of time, and that there was a significant hydrologic cycle that would have formed the valley networks.

In order to sustain such a climate, the ancient Martian atmosphere would have required a much higher surface pressure so that the greenhouse effect from CO_2 and water would be significantly higher than today. The amount of CO_2 in the ancient Martian atmosphere is poorly constrained. Tian et al. (2009) argue that any primordial atmosphere of CO_2 would have escaped to space prior to about 3.9 Gya (billion years ago). Hence a high CO_2 abundance during the formation of the river valley networks would have required outgassing after 3.8 Gya. Phillips et al. (2001) used terrestrial estimates for water and carbon dioxide contents of lavas and assumed that the formation of Tharsis processed the entire lithosphere below the volcanoes down to depths of 100 km. Given these assumptions, the formation of Tharsis could have released a mass of carbon dioxide equivalent to a surface pressure of 1.5 bar, a mass of $\sim 2.3 \times 10^{21}$ g of SO_2,

and the equivalent of a 120 m–thick layer of water. However, a more conservative estimate based on the measured water content of SNC meteorites—shergottites, nakhlites, and chassignites, which presumably came from Mars, would reduce the Tharsis water to no more than 10 meters. Additionally, little CO_2 should be expected from the Tharsis volcanoes, given that the origin of volcanic CO_2 on Earth is subduction. Alternatively, Toon et al. (2010) argue that an impact could produce a CO_2 atmosphere from the C in the impactor. An added source would be the 2-5% carbonate in the Martian regolith (Banfield et al., 2003), which might be released by an impact or its secondaries.

An additional difficulty greenhouse models must overcome is the "faint young sun problem," the fact that early in the history of the solar system the sun was 70-75% as bright as at present. The faint young sun problem greatly limits the ability of models to simulate a warm, wet atmosphere early in Martian history, even when accounting for the higher density atmosphere (Haberle, 1998).

Segura et al. (2002, 2008) proposed that the ancient climate could have been warmed through impacts 30-100 km or greater in size. Water released during the initial impact would act as the primary greenhouse agent, trapping the thermal energy released during impact. This water would potentially keep the climate in a quasi-stable warm state for periods of time ranging between 100 days to decades even without including the radiative effects of water clouds. When clouds effects were included, it was found that the equatorial region could potentially remain warm for centuries at a time, depending on the size of impactor.

Impactors of sufficient size would produce a global layer of hot debris, significantly raising the global surface temperature (Sleep and Zahnle, 1998). Most of

this debris comes from the crater formed in the initial impact, however some comes from secondary impacts, which occur after large pieces are thrown into the air because of the primary impact, and then land elsewhere, creating smaller craters. In addition to the solid ejecta, a significant amount of water is released during the impact. There are three main sources of water. Water contained inside the impactor, water contained in the surface material at the impact site, and any surface water ice, which will melt and evaporate when it comes into contact with the hot debris.

After the initial input of heat and water to the system, a certain period of time is required for the planet to return to pre-impact conditions. How long this takes depends on the total amount of heat and water, which is directly related to the impactor size. The study by Segura et al. (2008) showed that for impactors 30-100 km in size, this period could last for decades. During this time, the climate would support a stable hydrologic cycle. Additionally, the rainfall and following erosion would have been strong enough to produce the river valley networks observed today.

In this work, we simulate some possible ancient climate scenarios with a thick 500 mb CO_2 atmosphere, a reduced solar constant, and varying amounts of initial water. We will show that the greenhouse warming by water-ice clouds is very strong, and could have sustained a warm climate for extended periods of time.

3.3 Model Description

3.3.1 Climate model

We use a modified version of the Community Atmosphere Model (CAM) originally developed by the National Center for Atmospheric Research (NCAR). We have adapted the original terrestrial model (Collins et al., 2004) for Martian conditions. A detailed description of the most significant model changes, which includes changes to planetary parameters, the addition of carbon dioxide condensation and sublimation at the surface, and the replacement of the radiation transfer scheme, is in our companion paper (Urata and Toon, 2012a). Therefore in this paper we will focus on summarizing the physics in the model related to the hydrological cycle, beginning with the sources, then proceeding through the cloud related physics including formation, sedimentation, and radiative transfer.

3.3.2 Water sources

A permanent water-ice cap in the northern hemisphere is assumed as the sole source of water for the system, apart from the initial atmospheric water content in both the present climate and the past. In the present climate, the initial atmospheric water content is set to approximately 10 pr-μm globally averaged. There is no initial sub-surface ice, however water is allowed to permeate the soil if the surface is wet. Vertical transport of water through the soil depends on infiltration, runoff, gradient diffusion, and gravity (See Oleson et al., 2004 for details of the soil component). The prescribed cap extends from 82°N to the pole, and acts as an infinite source of water. Of course, Mars presently also has a permanent ice cap in the southern hemisphere. As will be shown in

the results, not including a water-ice cap at the South Pole does not significantly affect the annual water cycle in comparison to observations, as water quickly migrates from the north to the south to form a water reservoir, and the cold temperatures of the permanent CO_2 ice cap inhibit sublimation from the water ice.

Water sublimates from any surface ice into the first atmospheric layer unless the layer is saturated. The thermal and radiative properties of the Martian water ice caps are given in Table 3.1.

Parameter	**Model Value**	**Source**
RH_{min}	0.8	
T_0	273 K	
Gravity	3.72 m s^{-2}	
Viscosity of Air	1.45e-5 Pa s	Pang, 2005
Density of Water Ice	0.917 g cm^{-3}	
Ice emissivity	0.97	Oleson et al., 2004
Ice thermal conductivity	2.29 W m^{-1} K^{-1}	Oleson et al., 2004
Ice specific heat capacity	2.11727e3 J Kg^{-1} K^{-1}	Oleson et al., 2004
Critical cloud mmr for coalescence *(l_0)*	10^{-3} g g^{-1}	Lin et al., 1983
Level for 1 µm cloud particles	Above 100 Pa	Clancy et al., 2003
Level for 4.5 µm cloud particles	Above 300 Pa	Clancy et al., 2003
Level for 10 µm cloud particles	Below 300 Pa	Whiteway et al., 2009

Table 3.1. Model Parameters.

Heat transfer through the ice is calculated using the same method as through soil, with the thermal properties for soil replaced with ice values. It assumes transfer via thermal conduction (Eq. 3.2; F_s is the heat flux (positive upwards), λ is the thermal conductivity, T is the soil temperature, and z is the vertical direction (positive downwards)) through 10 layers of increasing thickness, with the bottom layer approximately 2.8 m below the

surface. The heat flux of the top layer is in balance with the heat flux from the overlying atmosphere (solar radiation, longwave radiation, sensible heat flux, and latent heat flux), and the bottom layer boundary condition is zero heat flux. The heat flux is found at each layer interface using a tridiagonal matrix to solve for the energy balance. These fluxes are used to calculate the subsurface temperatures by assuming energy conservation between the heat flux and temperature change (Eq. 3.3; *T* is the temperature, *t* is time, and *c* is the soil/ice volumetric heat capacity).

$$F_s = -\lambda \, \partial T/\partial z \quad F_s = -\lambda \frac{\partial T}{\partial z} \quad (3.2)$$

$$c \, \partial T/\partial t = -\partial F/\partial z \quad (3.3)$$

3.3.3 Cloud physics

Atmospheric water can remain in gas form and be advected throughout the atmosphere, or it can form clouds and be advected in condensed form. CAM has an extensive cloud physics package that we have adopted largely unmodified from the original implementation, which primarily follows the model of Sundqvist (1988). The model includes a bulk condensation and evaporation scheme described by Rasch and Kristjansson (1998), and Zhang et al. (2003), in which condensation and evaporation are determined from the large-scale tendencies of water vapor, temperature, and cloud condensate. This scheme provides the model with the amount of condensed liquid and ice from which precipitation is formed. The following provides a conceptual model for the parameterization involved. Collins et al. (2004) provide a more detailed description.

One drawback to any GCM is the coarse horizontal resolution required for reasonable use of computational resources. Our typical simulation has a horizontal resolution of 4°x5° (lat x lon). This corresponds approximately to 240 x 300 km at the equator (240 x 50 km at 80°) on Mars. Because of the large grid cells, parameterization of sub-grid scale physics is important to take into consideration. This is done in the cloud physics routines by assigning cloud coverage fractions for grid cells, and adjusting the model in-cloud water paths according to this fraction. This fraction is calculated as:

$$C=\{(RH - RH_{min}) / (1 - RH_{min})\}^2 \quad (3.4)$$

Here, the cloud fraction C has a maximum value of 1, RH is the relative humidity of the grid, and RH_{min} is a minimum relative humidity below which C is zero (Slingo, 1987). RH_{min} is a model parameter that represents the variability of cloud formation on the sub-grid scale. For example, grid cells over large terrain, as opposed to over flat surfaces, tend to have a lower value for RH_{min} because the sub-grid scale variations in topography and surface properties can lead to pockets of high relative humidity even when the grid averaged relative humidity is much less than 1. Comparisons with terrestrial observations lead to a value of RH_{min} that typically ranges between 0.8-0.9 (Slingo, 1987; Zhao et al., 1997). The value 0.8 has been used in this work because of the lack of oceans on Mars, and the large topographical variation.

The original version of the model assumed clouds form when some critical humidity is reached, but supersaturation was not allowed. The current version has been slightly altered to allow for supersaturation by modifying the saturation specific humidity by a temperature-dependent critical saturation ratio. Detailed observations of the vertical profile of water vapor reveal that supersaturation of water vapor is a significant process in

the hydrologic cycle on Mars. Recent observations from the SPICAM (Spectroscopy for the Investigation of the Characteristics of the Atmosphere of Mars) instrument aboard Mars Express, obtained via solar occultations, show water vapor to be supersaturated by more than a factor 10 between 20-50 km (Maltagliati et al., 2011). While supersaturations in the Earth's lower atmosphere are generally less than 50%, very high superaturations like those on Mars are believed to occur in the mesosphere in seasons when noctilucent clouds occur (e.g. Bardeen et al., 2010). Temperatures in the noctilucent cloud regions are around 150K or less. The cause of the supersaturation on Mars is not well understood, however it is likely related to a low condensation efficiency due to the small surface areas of cloud particles, which in turn is due to a low concentration of dust nuclei (Montmessin et al., 2004), and to the low temperatures of the upper Martian atmosphere (Trainer et al., 2009; Iraci et al., 2010). Laboratory experiments on ice nucleation rates for temperatures below 180 K have shown that the critical saturation ratio for nucleation can be significantly higher than 1, contrary to classical nucleation theory based on ice contact parameters close to unity, which predicts supersaturation values between 1-2 (Maattanen et al., 2005). The Trainer et al. (2009) results show an exponential temperature dependence for the contact parameter *m*, which corresponds to a relation of surface free energies between the substrate, nucleating solid, and the vapor (Eq. 3.5).

$$m = 0.94 - 6005e^{0.065T} \quad (3.5)$$

This parameter can vary between -1 to 1, where a value of -1 signifies no surface wetting, and 1 means complete surface wetting. The exponential dependence of *m* on temperature suggests that at very low temperatures, it may become exponentially more difficult to form cloud particles. In fact, the experiment, which extended down to 153 K, showed that

when nucleating onto 1 μm particles, the critical saturation ratio could reach up to 30. In the model, we use *m*, and Eqs. (3), (4), (8), and (9) from Trainer et al. (2009) to derive the temperature dependent critical saturation ratio (S_{crit}), and use this value as the criteria for condensation. Specifically, RH_{min} is multiplied by S_{crit} so that $RH_{min}{}^{*}=S_{crit}*RH_{min}$, preventing cloud formation until sufficient supersaturation is reached. However, this method alone does not suppress cloud formation at high summer latitudes to the degree that is observed, because it is relatively warm in the summer polar region so the S_{crit} value from Eq. 3.5 is quite low. Therefore, some simulations also include an ad hoc assumption of high S_{crit} at the latitudes in question in order to match the observed hydrologic cycle. More discussion of this assumption is provided in the later sections.

Precipitation in the model is determined by parameterizing the conversion of cloud condensate to precipitation. The precipitation rate calculations are separated into liquid processes and ice processes. Liquid water and ice are tracked independently as mass mixing ratios. However, due to the low Martian temperatures, liquid clouds are rare and we will concentrate here on describing the ice precipitation processes. The auto-conversion rate of cloud ice to precipitation is found using the method of Lin et al. (1983). This method uses a temperature-dependent rate coefficient to parameterize the collision-coalescence efficiency of ice crystals to form snow, and the collection efficiency of ice crystals onto snow. The latter also depends on the assumed size-distribution of the snow particles, which is derived from terrestrial observations.

$$E_i = C_i\, e^{0.025(T-T0)} \quad (3.6)$$

Equation 2.6 is the original form of the temperature-dependent rate coefficient found in Lin et al. (1983), where C_i is 10^{-3} for coalescence, and 1 for collection. In coalescence,

this coefficient multiplied by the ice content results in a precipitation rate (s^{-1}) used to modify the cloud mass. Because coalescence can only occur when there are a significant amount of particles, a heavyside step function is also included so that some critical mass mixing ratio (l_0) must be achieved for this process to occur. For collection, the coefficient is multiplied by the ice content adjusted for the size distribution of the snow particles to result in a precipitation rate. The precipitation rates are summed to find a total rate, which is then used to calculate cloud mass loss due to precipitation. Here, T is the ambient temperature, and T_0 is the freezing point of water. The default version of the model does not include the temperature dependence, and instead assumes a constant rate coefficient for both cases; assuming it to be 10^{-3} for coalescence, and 1 for collection. This essentially assumes local temperature changes to have minimal effect on the auto-conversion rate. This does not have a serious impact in the terrestrial case, where temperatures do not vary greatly. In the Martian case however, atmospheric temperatures in the troposphere can range anywhere between 140-240 K (corresponding to an order of magnitude change in E), which led to the decision to reintroduce the temperature-dependence of the auto-conversion rate to the model.

Clouds are assumed to sediment with the Stokes-Cunningham fall velocity for a sphere, given as:

$$\nu = (2/9)\,(\rho g R^2/\eta)(1 + \alpha Kn) \quad (3.7)$$
$$\alpha = 1.246 + 0.42e^{(-0.87/Kn)}$$

Where ρ is the ice density, g is gravity, R is the particle size, η is the dynamic viscosity of air, Kn is the Knudsen number, α is a correction factor, and the air density is assumed to be small compared to the particle density. Gravity and air viscosity have been scaled appropriately to Martian values. A summary of these and other parameters is given in

Table 3.1. Precipitation is assumed to fall almost instantly to the ground. It is not exactly instant because as the precipitation falls, it is free to interact with the lower levels. If the layer it enters is not saturated, the precipitation will sublimate until saturation is reached. If the layer already contains a cloud, then the precipitation will not sublimate and will continue to fall. Any precipitation that remains in the bottom-most level is assumed to fall on the ground, at which point it can melt or accumulate to form snow layers.

3.3.4 Radiative transfer

We use the Toon et al. (1989) correlated-k two-stream model as adapted to Mars by Colaprete and Toon (2003) to calculate the radiative transfer in the atmosphere, and have added the effects of collision-induced absorption by CO_2 by the method of Wordsworth et al. (2010). For the radiation through clouds, we use the optical constants of water and ice (Segelstein, 1981; and Warren and Brandt, 2008 for water and ice, respectively) together with Mie theory to compute the cloud radiative properties (extinction efficiency, scattering efficiency, backscatter coefficient). CAM provides liquid water and ice water content for each model layer. We then assume fixed particle sizes to interpret the scattering and absorption by the clouds and to determine the optical depth, which is linearly related to the ice content, and inversely related to the particle radius. We choose spheres of radius 1-10 μm for water and ice clouds depending on height since typical Martian water cloud particle size tends to range from 1-30 μm (Whiteway et al., 2009; Clancy et al., 2003). This is a crude way to parameterize the effective cloud particle size that should be improved on in the future. A better method

would be to compute the cloud particle size from first principles, which is possible in the newest version of CAM5. However, this remains a difficult problem even on Earth, because of uncertainty in how ice particles form.

The wavenumber-dependent optical depths are found from the equation:

$$\tau_{ext} = 3\, M_c Q_{ext} / 4\rho R \quad (3.8)$$

Where M_c is the cloud mass in the layer (g m^{-2}), Q_{ext} is the wavenumber dependent extinction efficiency, ρ is the cloud particle density, and R is the effective cloud particle size. The single-scattering albedo and asymmetry parameter are weighted with gas and Rayleigh values in the two-stream model to compute the total absorption and scattering.

Fractional cloud coverage and cloud overlap is considered using the Monte Carlo Independent Column Approximation (McICA) method described by Pincus et al. (2003). This stochastic method approximates the contributions of cloud fraction and overlap by treating each individual spectral interval as a column, and designating the interval as cloudy or clear depending on the cloud fraction. It is inherently less accurate compared to the full Independent Column Approximation method (Cahalan et al., 1994), which calculates a weighted average over all possible cloud states. However it is less computationally expensive by orders of magnitude (the number of calculations required will scale with the number of cloud states), and is more flexible than other methods that make ad hoc assumptions about the cloud states (Stephens, 1988; Oreopoulos and Barker, 1999; etc.). The error introduced (through random noise) by this method is typically within 10%. However the error is random, unbiased, and will be suppressed in the limit of the many calculations done over a typical simulation. For each level, random numbers are generated for the spectral intervals and compared to the grid cloud fraction to

determine the cloud states. Cloud overlap is a key part to any cloud radiation scheme, as the radiation spectrum below a cloud will be very different from the clear-sky spectrum. In this model, overlap is treated in one of three ways. In maximum overlap mode, the same random seed is used in all levels, meaning that whenever clouds are present in multiple levels, they will always overlap. In random overlap mode, a new seed is generated in every level, so the chance that clouds in different levels overlap is totally random. The third method, called maximum-random overlap mode, is the preferred method. In this mode, the same seed is used when two or more consecutive levels contain clouds, but a new seed is generated when there are one or more levels between clouds. This is equivalent to saying that very thick clouds that span two or more levels should overlap, but detached clouds will have a random chance of overlapping.

3.4 Present Climate Simulations

3.4.1 Model Initial Parameters for Hydrological Cycle Simulations

The model's ability to simulate the Martian hydrologic cycle was validated by comparing model results to observations of the annual water vapor distribution and cloud opacities. For these simulations, the sources of water are an initial atmospheric water vapor content of 10 pr-μm and a prescribed water ice cap above 82°N, summarized in Table 3.2.

Parameter	**Value for present day**	**Value for ancient climate**
Solar constant	590 W m^{-2}	75% of present day
Average Surface Pressure	6.5 mb	500 mb

Column water vapor	10 pr-μm	Varying
Ground ice	None	None
Permanent CO_2 cap	None	None
Permanent water ice cap	North of 82°N	North of 82°N
Dust optical depth	0.3	0.001

Table 3.2. Initial conditions.

There is no permanent CO_2 ice cap, and dust is prescribed as non-varying with a globally averaged optical depth of 0.1. We have also conducted sensitivity tests to water ice albedo, and examined the effects of forcing supersaturation to certain latitudes, summarized in Table 3.3. In all cases, the model was initialized from a previously performed 10 Mars year run (with base case parameters), then run for an additional 4 Mars years, with the results coming from the fourth year. Water was allowed to move freely during the initialization run, and there was a net deposition of water ice at the South Pole, indicating an imbalance of water in the current climate.

Simulation	**Water-ice cap albedo**	**Forced supersaturation**
Base case	0.4	None
Best-fit with no forced supersaturation	0.57	None
Best-fit with forced supersaturation	0.55	40°N to pole

Table 3.3. Parameters for present climate simulations.

3.4.2 Simulation Results

The simulation results of the base case scenario are presented in Fig. 3.1 for the fourth year of the run.

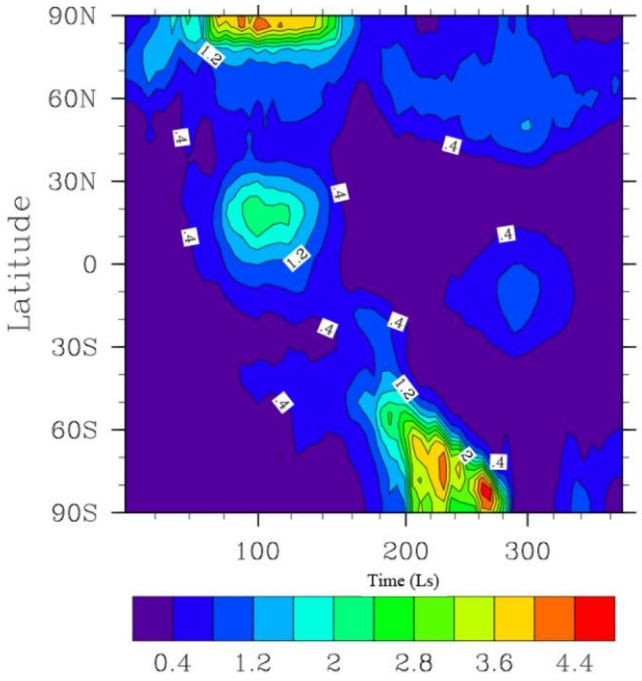

Figure 3.1a. The base case simulation results. Zonal average cloud absorption opacity between 800-875 cm^{-1} vs. L_s.

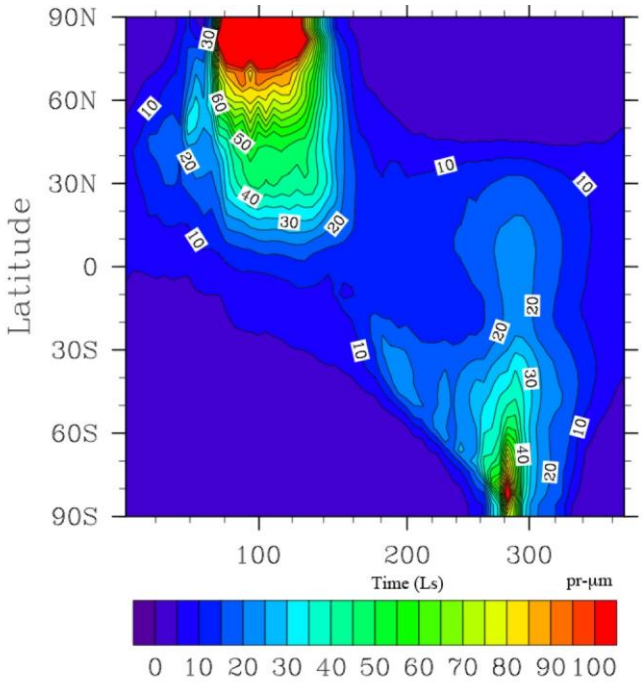

Figure 3.1b. The base case simulation results. Zonal average water vapor column abundance in precipitable microns (pr-µm) vs. L_s.

The polar water-ice cap albedo was set to 0.4 (Paige et al., 1994) and only the Trainer et al. (2009) temperature dependent critical supersaturation was assumed (i.e., no forced supersaturation at high summer latitudes). Figure 3.1a shows the zonally averaged values for cloud absorption optical depth in the 800-875 cm^{-1} waveband versus L_s, and Fig. 3.1b shows the total water vapor column mass in pr-μm. The absorption optical depth is chosen for comparison to Smith (2008) TES observations, which reported the absorption optical depth. The relevant parameters of the simulations are presented in Table 3.3.

The pattern for water vapor in Fig. 3.1b is in general agreement with TES observations (Fig. 3.2a, 3.2b), with a peak in the northern hemisphere around L_s=120°, and a smaller peak in the southern hemisphere around L_s=300°.

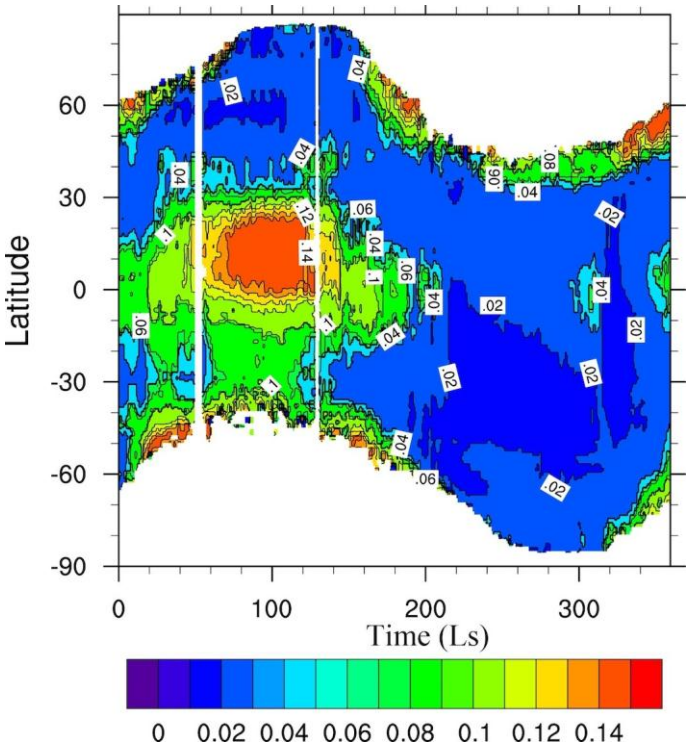

Figure 3.2a. Smith (2008) TES observations of zonal average vs. L_s for cloud absorption opacity at 825 cm^{-1}.

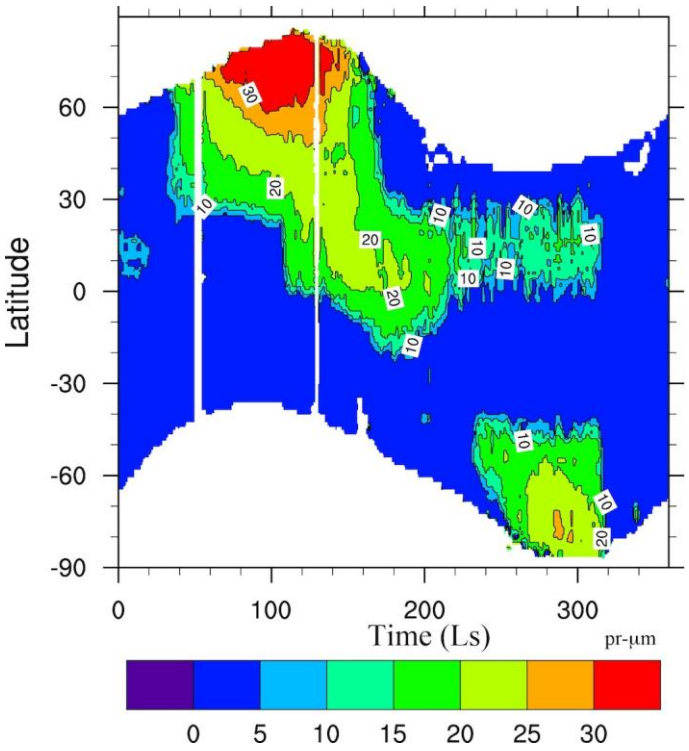

Figure 3.2b. Smith (2008) TES observations of zonal average vs. L_s for water vapor column abundance in precipitable microns (pr-μm).

Although we did not start the model with a permanent ice cap in the southern hemisphere, water migrates from the north to the south in the model, so a polar winter reservoir is quickly established. However, the simulated total water vapor content is much higher than observations, with a peak value of more than 200 pr-μm. Unlike the water vapor, which matches observations in pattern but not magnitude, there is a large discrepancy between the model (Fig. 3.1a) and observations in the water-ice opacities (Fig. 3.2a; Smith, 2008). Although the model reproduces the aphelion cloud belt the optical depths are about a factor of 10 greater than those observed. The model also predicts that a thick cloud layer will form above the summer hemisphere pole that is not observed. During northern summer, the total cloud opacity above the pole can reach as high as 2.5 in the model, while TES shows almost no water-ice opacity at these same times of year. Clouds

also form over the southern pole during southern summer, which are optically thicker than the clouds that form over the northern pole at L_s=120°. The clouds are optically thicker in the south than the north even though the concurrent water vapor column is less than half of the value over the northern pole during northern summer because of different cloud particle size. During southern summer, the planet is near perihelion, causing the southern summer temperatures to be warmer than the northern summer temperatures over the respective poles. This temperature difference causes the level at which clouds form to be higher during southern summer compared to northern summer, which in turn causes clouds with smaller particles because of our assumptions (Table 3.1). As the particle radius can vary by up to a factor of 10 with altitude in the model, the opacity can be two or three times higher for the southern clouds even if the cloud mass is only half, because the optical depth is proportional to column mass divided by radius.

Two main conclusions about the model's performance can be drawn from the base case scenario. First, that the model releases too much water from the cap when assuming an average albedo of 0.4. This could be due to the spatial distribution of the cap in the model being uniformly water-ice above 82°N, while in reality the cap extension varies with longitude. Also, while the model assumes a constant albedo for all surface ice, the actual cap albedo varies (Paige et al., 1994). Both factors could contribute to the excessive water found in the model. In the end, this is an issue with the rate of water release from the cap, and can be addressed in the model by raising the cap albedo, or shrinking its size. The second conclusion is that the model fails to take into account some process that occurs at high latitudes in the summer hemisphere that suppresses cloud formation and observed opacities. Observations by Maltagliatti et al. (2011) discussed

earlier, suggest this process is supersaturation. Observations of the water vapor column abundance show a maximum of about 70 pr-μm over the pole at the times in question. Assuming that the water vapor is uniformly mixed, then it is equivalent to a partial pressure of approximately 0.26 Pa. For comparison, typical Martian temperatures above these locations range between 180-200 K, with corresponding saturation vapor pressures of 0.005-0.16 Pa. This suggests that the atmosphere is supersaturated by at least a factor of 1.6, and possibly up to a factor of 50 depending on the vertical distribution of the water. Similar supersaturations occur in the mesosphere on Earth, where terrestrial noctilucent clouds form (Bardeen et al., 2010). A possible contributor to the supersaturation could be a low ice nuclei concentration. Low particle densities can permit supersaturation because a very small number of ice crystals, with a low surface area, will be ineffective in reducing the supersaturation by growth. Additionally, a limited number of nuclei will lead to larger ice particles being formed. Larger cloud particles yield smaller cloud opacities, due to the inverse relation between opacity and size. It is possible to force high supersaturation in the model by raising the critical saturation ratio to a high number.

To test the sensitivity of the hydrologic cycle to cap albedo, multiple simulations were performed with increasing albedo from the base case of 0.4, up to 0.57, at which point the maximum water vapor column abundance decreased to 65 pr-μm, which is in the range of the observations. Figure 3.3 shows the cloud opacities and water vapor column abundances for the albedo = 0.57 simulation.

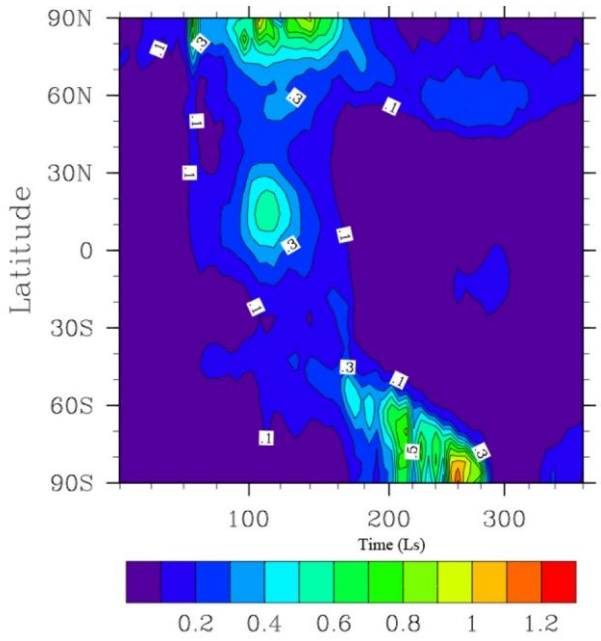

Figure 3.3a. Same plot as Figure 3.1a, for the cap albedo = 0.57 case.

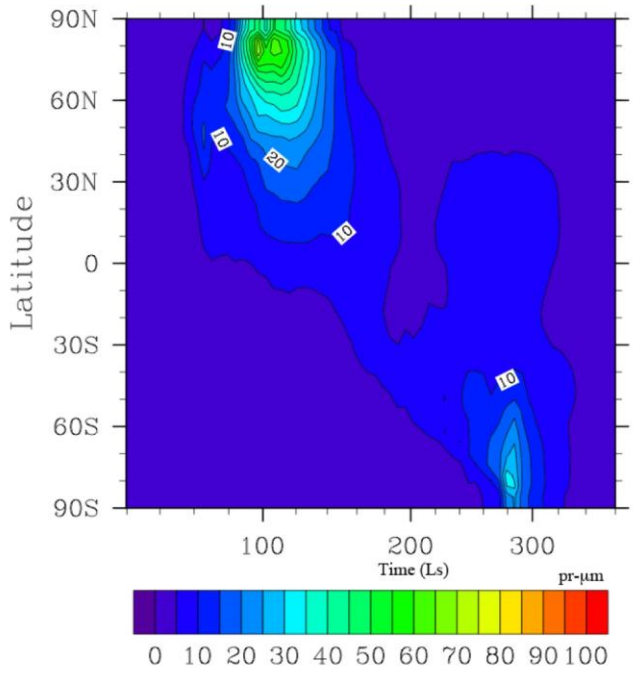

Figure 3.3b. Same plot as Figure 3.1b, for the cap albedo = 0.57 case.

As expected from a higher albedo cap, the total amount of water vapor is significantly reduced compared to the base case. However, while the total amount of water vapor is reduced, relatively thick clouds are still present above the pole during the summer time.

To achieve the relatively high water vapor abundance concurrent with optically thin clouds, we performed simulations where the critical supersaturation ratio was set to 100 (almost completely preventing cloud formation) poleward of a critical latitude for between L_s=60°-180° in the north, and L_s=240°-360° in the south. Outside of these ranges, the critical supersaturation was derived from the local atmospheric temperature following Trainer et al. (2009). Figures 3.4 and 3.5 show the results for simulations where the critical latitude was set to 75°, and 40° respectively, and the cap albedo was set to 0.57, which gave the best water vapor agreement in the "no forced supersaturation" scenario.

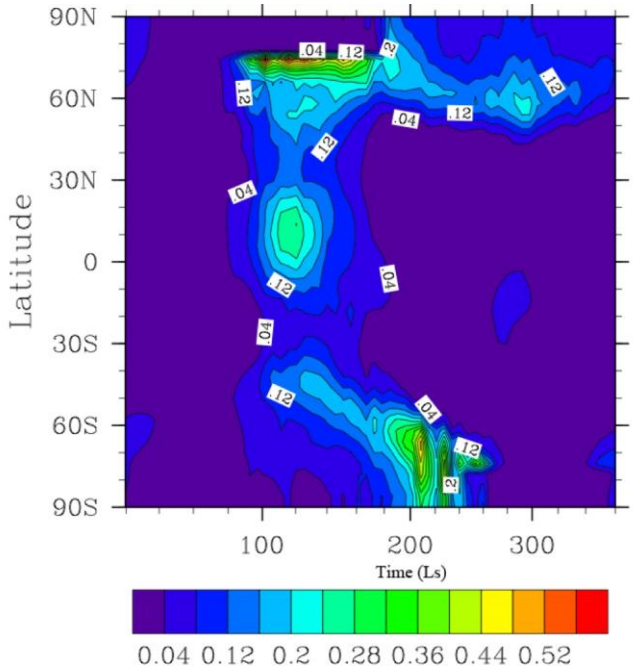

Figure 3.4a. Critical saturation latitude = 75°, cap albedo = 0.57 case, showing cloud absorption opacity.

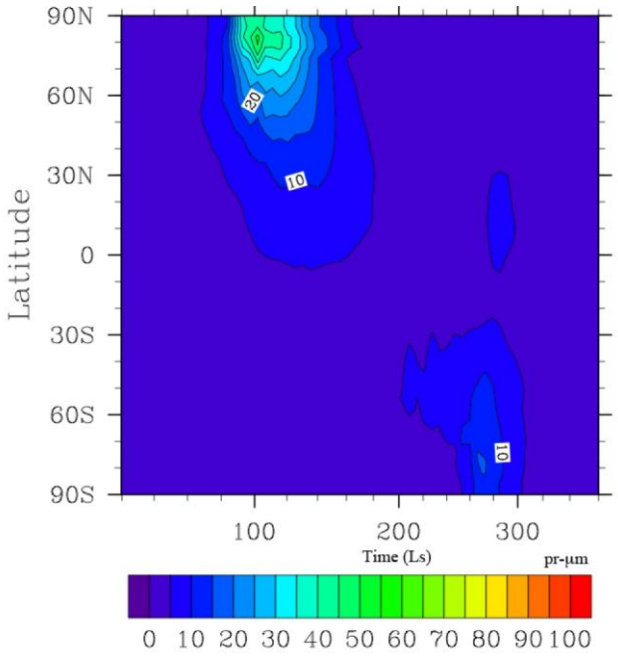

Figure 3.4b. Critical saturation latitude = 75°, cap albedo = 0.57 case, showing water vapor column abundance (pr-µm).

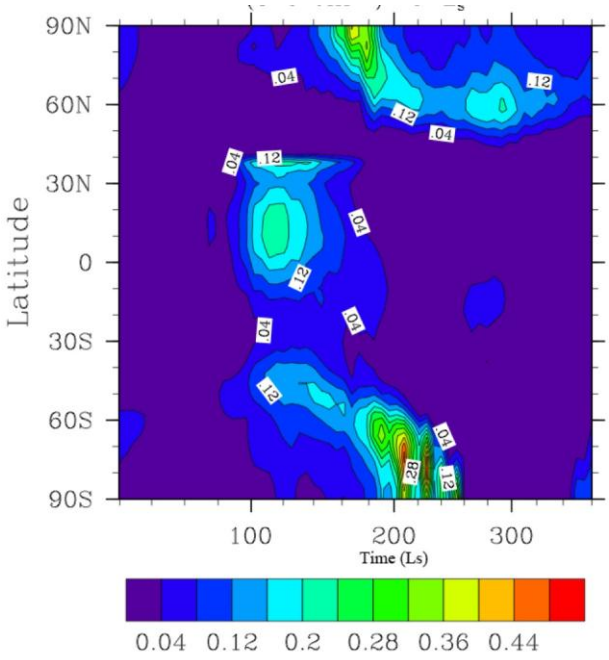

Figure 3.5a. Critical saturation latitude = 40°, cap albedo = 0.57 case, showing cloud absorption opacity.

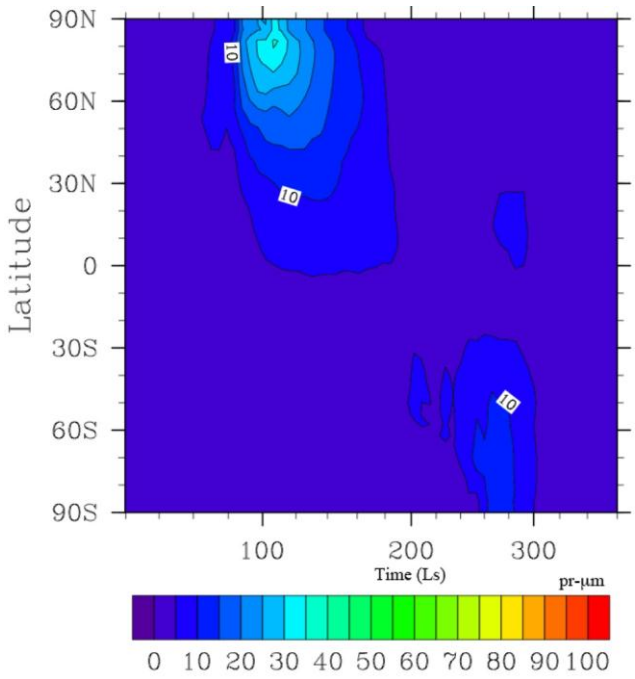

Figure 3.5b. Critical saturation latitude = 40°, cap albedo = 0.57 case, showing water vapor column abundance (pr-µm).

In each case, only optically thin clouds were formed in the "forbidden" region, and were accompanied by an optically thicker band of clouds just south of the critical latitude during northern summer. Curiously, something similar appears in the TES observations near 40°N (Fig. 3.2a). Whether the two features are related will require further investigation into the cause of high supersaturation, which could be either limited ice nuclei, or something about the physics of ice nucleation.

While forcing supersaturation to be high improved the simulated cloud optical depths, and decreased the opacity of clouds over the summer pole, it also decreased the total amount of water vapor in the atmosphere. The peak value fell from 65 pr-µm to 35 pr-µm in the critical latitude = 40° case. The main reason for this reduction of the water column is that the clouds that formed over the pole in the "no forced supersaturation"

scenario caused warming, which led to an increase in the amount of water released from the cap. The altitude at which these clouds formed is of particular interest. Clouds that form near the surface will tend to cool the surface by reflecting sunlight, but they radiate as much infrared to space as the surface did. High, cold clouds radiate little energy to space, which warms the atmospheric column and the surface. The zonally averaged cloud water path (g cm^{-3}) for the "no forced supersaturation" scenario at L_s=120° is shown in Fig 3.6. Here it is apparent that the polar cloud is thickest near 350 Pa, which is approximately 5 km above the surface, where the air temperature is 180 K. Given this air temperature and the ground temperature of 220 K, Eq. 3.1 indicates that the cloud should cause local warming.

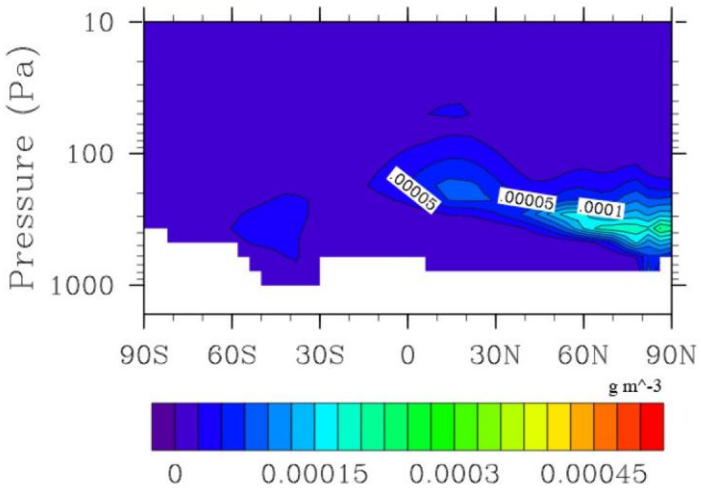

Figure 3.6. Zonally averaged cloud water concentration (g m^{-3}) for the "no forced supersaturation" scenario at L_s=120°.

Forcing supersaturation in the model improved the cloud opacities and water vapor in the model, leading to a hydrologic cycle that resembles TES observations. We have shown that raising or lowering the albedo primarily affects the total amount of water released into the atmosphere, and has little effect on the cloud distribution. Currently, the

"best-case" in terms of matching the magnitude and pattern of the water column and ice cloud opacity observations corresponds to a cap albedo of 0.55 (Fig. 3.7), and a forced supersaturation from the pole to 40° in the summer hemisphere.

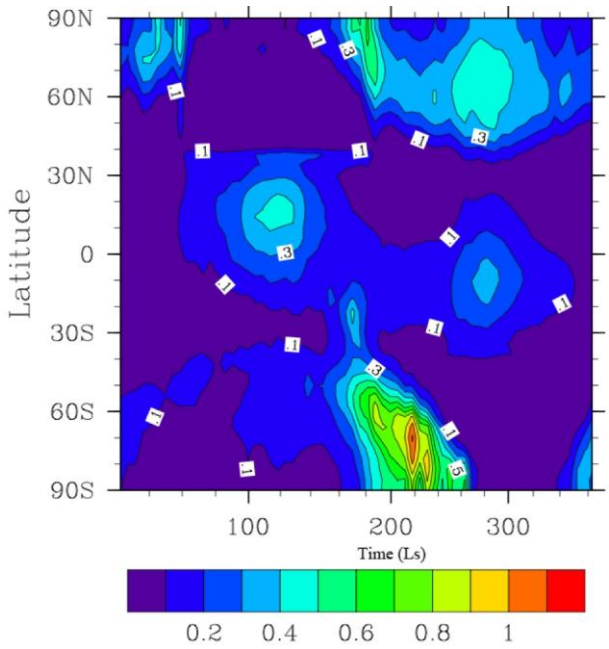

Figure 3.7a. "Best-case" scenario with critical saturation latitude = 40°, cap albedo = 0.55, showing cloud absorption opacity.

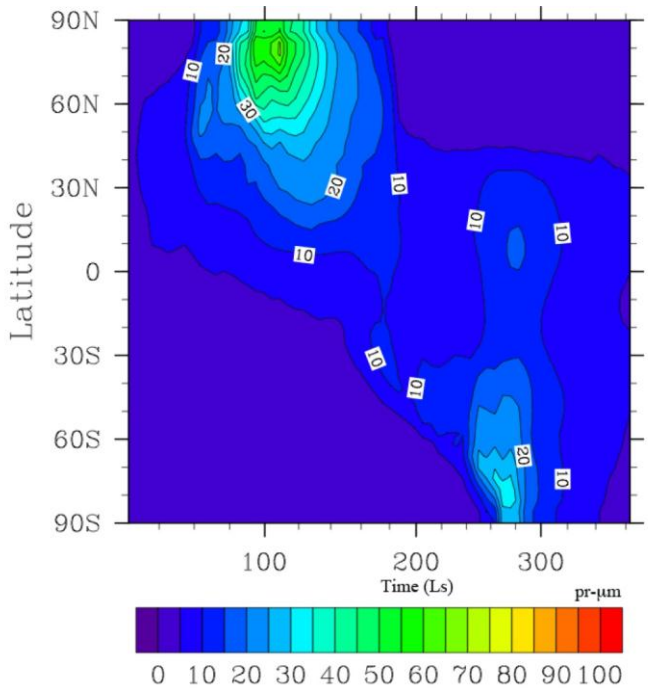

Figure 3.7b. "Best-case" scenario with critical saturation latitude = 40°, cap albedo = 0.55, showing water vapor column abundance (pr-µm).

The small albedo change between the simulations in Fig. 3.5 and 3.7, illustrates the high sensitivity of the water vapor cycle to the polar cap albedo. The peak water vapor column abundance is approximately 65 pr-µm, and few clouds occur in the summer hemisphere at high latitudes. Some clouds form in the tropics in the model during southern summer that are not observed, however this is likely due to the model's time-invariant dust distribution. Dust storm activity increases during southern summer, increasing atmospheric temperatures and thus the saturation vapor pressure for water over ice, which would lower cloud amount.

3.4.3 General impact of clouds on the Martian climate

Although the water ice clouds on Mars are relatively optically thin, their radiative impact on the climate is actually quite significant. The effects on temperature of including radiatively active clouds are presented in Figs. 3.8-3.11.

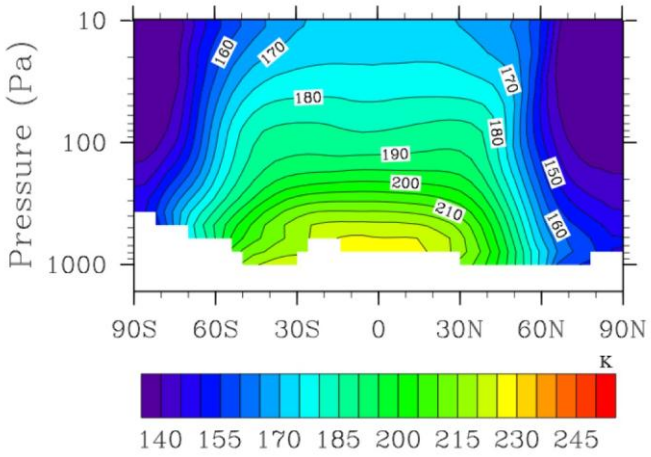

Figure 3.8a. Zonally averaged values at L_s=0° for temperature for the "Best case."

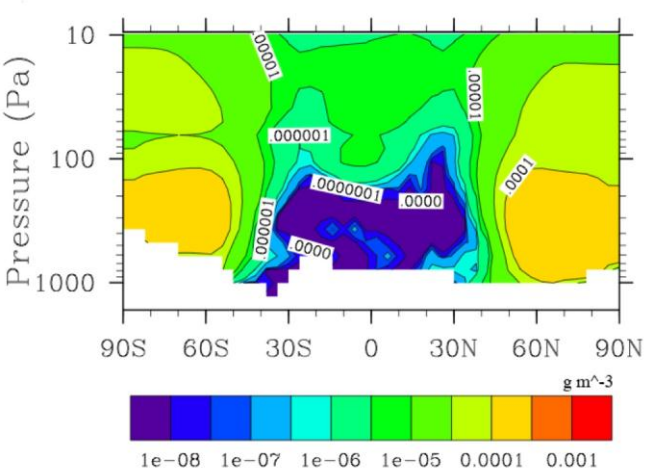

Figure 3.8b. Zonally averaged values at L_s=0° for cloud water concentration (g m^{-3}) for the "Best case."

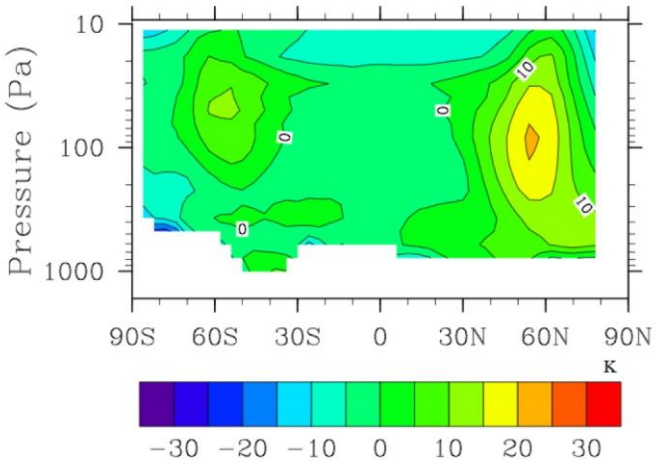

Figure 3.9a. Model minus TES zonally averaged temperature difference at L_s=0° for non-radiatively active clouds.

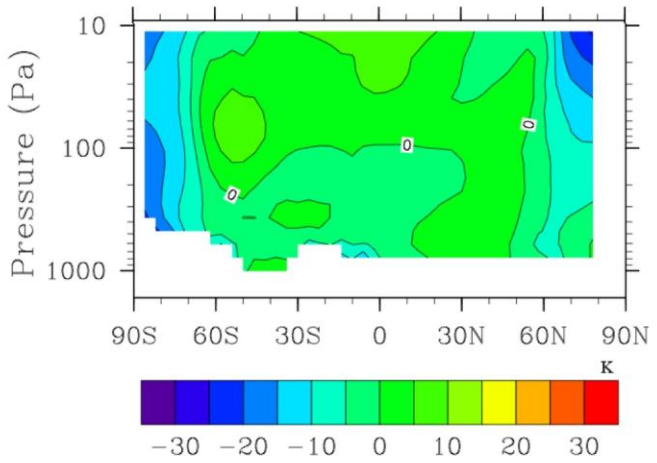

Figure 3.9b. Model minus TES zonally averaged temperature difference at L_s=0° for radiatively active clouds with fractional and overlapping clouds.

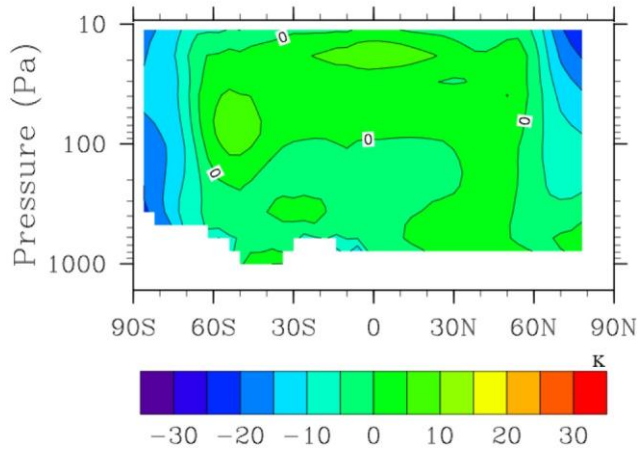

Figure 3.9c. Model minus TES zonally averaged temperature difference at L_s=0° for radiatively active clouds with full-grid clouds.

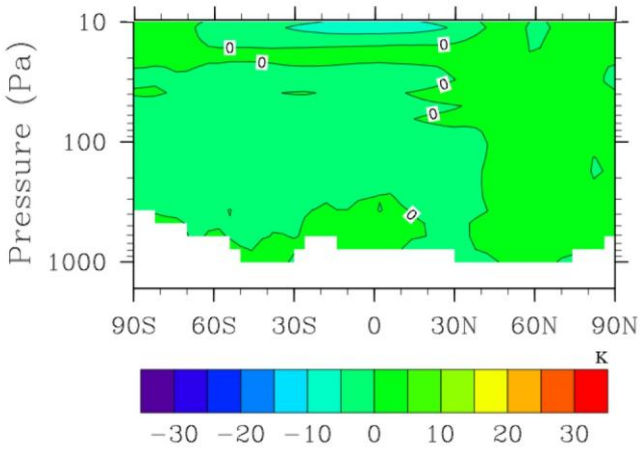

Figure 3.9d. Model zonally averaged temperature difference at L_s=0° for difference of (3.9b) minus (3.9c).

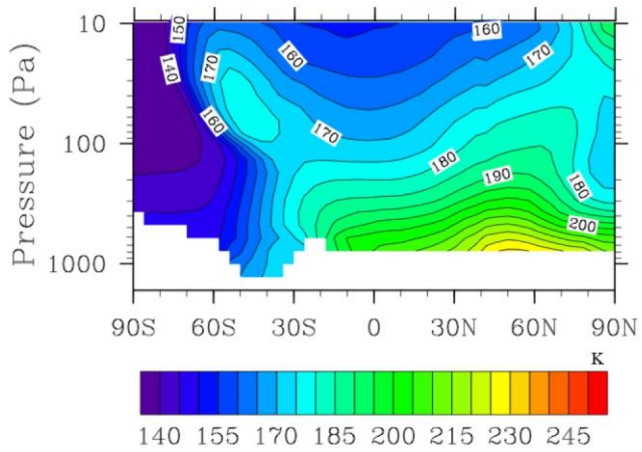

Figure 3.10a. Zonally averaged values at L_s=90° for temperature for the "Best case."

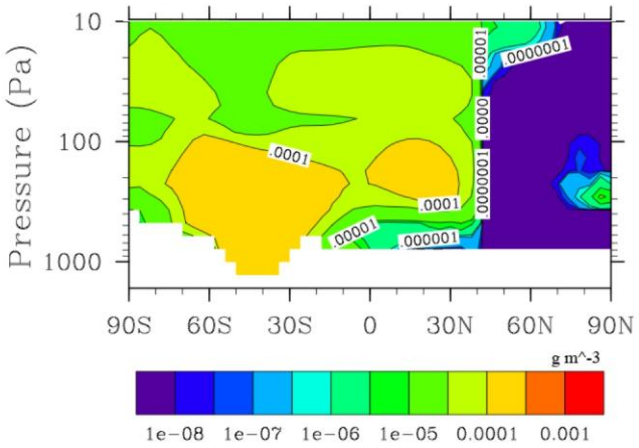

Figure 3.10b. Zonally averaged values at L_s=90° for cloud water concentration (g m^{-3}) for the "Best case."

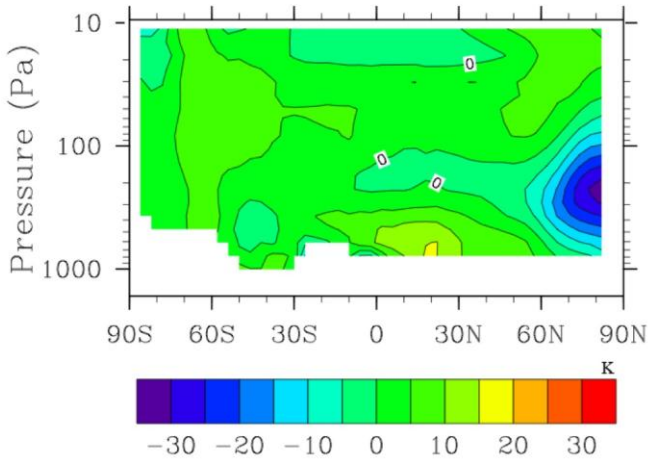

Figure 3.11a. Model minus TES zonally averaged temperature difference at L_s=90° for non-radiatively active clouds.

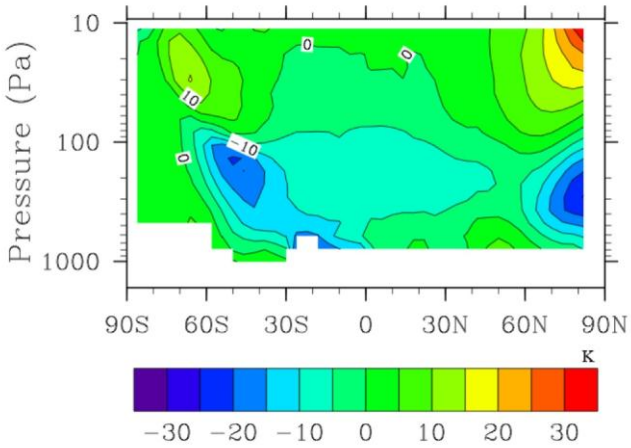

Figure 3.11b. Model minus TES zonally averaged temperature difference at L_s=90° for radiatively active clouds with fractional and overlapping clouds.

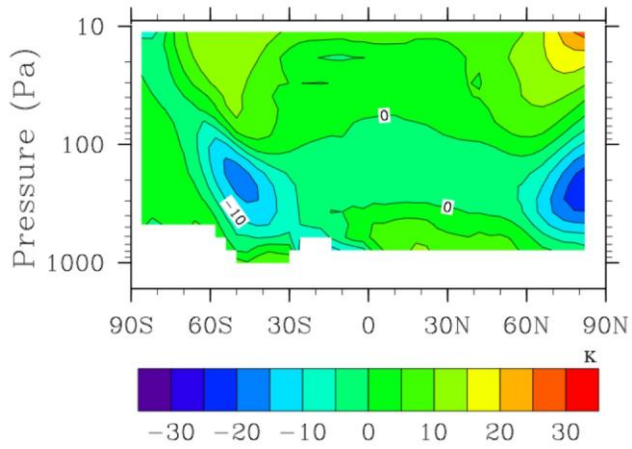

Figure 3.11c. Model minus TES zonally averaged temperature difference at L_s=90° for radiatively active clouds with full-grid clouds.

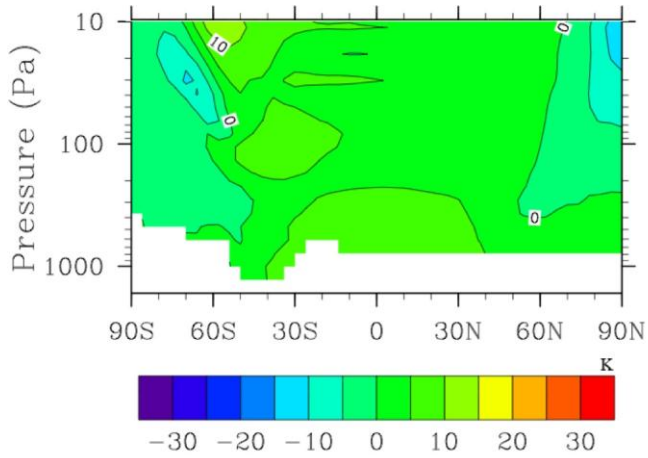

Figure 3.11d. Model zonally averaged temperature difference at L_s=90° for difference of (3.11b) minus (3.11c).

Figure 3.8a shows the zonally averaged temperature, while Fig. 3.8b shows cloud water concentration in g m^{-3} profiles at L_s=0º. Figure 3.9 shows the difference between model and TES observations at L_s=0º of the zonally averaged temperatures for non-radiatively active clouds (3.9a), radiatively active clouds with grid-fractional clouds and McICA overlap (3.9b), and radiatively active clouds with full-grid saturated clouds, where cloud

coverage is either 0 or 1 (3.9c). Figure 3.9d shows the difference between Fig. 3.9b and 3.9c, which represents the changes due to different ways of representing cloud coverage. Figures 3.10-3.11 show the same profiles at L_s=90º.

Comparing Fig. 3.9a with 3.9b or 3.9c shows that allowing the clouds to be radiatively active tends to warm the upper troposphere in the tropics, and cool the lower troposphere above the poles, improving the model's performance in these regions. With non-radiatively active clouds, the temperature at high altitude over the tropics was up to 15 K below observations. The greatest temperature difference with radiatively active clouds was 25 K high above the North Pole, with most of the atmosphere within 5-10 K. Just above the poles, the temperature was up to 10 K above observations with non-radiatively active clouds, but within 5 K of observations with radiatively active clouds. This difference in the sign of the effect of adding clouds in different locations is caused by the vertical distribution of the clouds in each region. Over the tropics, the clouds are tenuous and high above the surface, and therefore cause local heating. Over the poles, the clouds are thicker and closer to the ground, causing local cooling.

At L_s=90º (Figs. 3.10-3.11), the equatorial clouds (Fig. 3.10b) are thicker, and closer to the ground compared to at L_s=0º (Fig. 3.8b). This change in cloud properties results in the cooling of the lower troposphere in the cloudy case (Fig. 3.11b or 3.11c) compared to the non-cloudy case (Fig. 3.11a). The effect is most drastic between 30ºS - 60ºS, where the clouds result in temperatures up to 20K below observations. However, the tropical clouds tend to improve the lower tropospheric temperatures, which were up to 20 K warmer than observations without radiatively active clouds. The cause for the strong cooling in the southern hemisphere is the strong latitudinal temperature gradient

(and weak vertical gradient) present at this time of year in the southern hemisphere. Since much of the atmosphere is close to the ground temperature, Eq. 3.1 suggests that most clouds that form will cause cooling, indicating that there is an excess of clouds at these latitudes in the model. Unfortunately, the observations do not show cloud observations during the polar night (Fig. 3.2), so no definitive conclusions can be made about the cloud behavior at this time of year.

Altering the cloud fraction also impacts the cloud radiative effects. The difference between the TES observations and simulations with fractional clouds (3.9b, 3.11b) or clouds covering a grid cell (3.9c, 3.11c) is typically within 5 K, with little difference between the two cloud cases (3.9d, 3.11d). The difference is small because the clouds are thin enough that differences in cloud fraction do not significantly impact the radiative transfer. However, this is not necessarily true when thick clouds are present, as on Earth, or in our ancient Mars simulations discussed below.

3.5 Thick Atmosphere Simulation

3.5.1 Model Initial Parameters

We have performed simulations of the Martian climate with a thick carbon dioxide atmosphere, and a reduced solar constant (Table 3.2). As details of dust in the ancient climate are not well known, a reduced background dust field was used to minimize warming effects from dust. All other parameters, including topography, obliquity, surface albedo, and thermal inertia, have been left the same as present day,

although the thermal inertia would have been larger due to the contribution from the thicker atmosphere. Since the processes behind the forced supersaturation required to fit the present day hydrologic cycle are not well understood, high critical supersaturation is not included. Indeed since we are trying to obtain high surface temperatures, modest supersaturations below 50%, which occur in Earth's atmosphere are to be expected. However, cloud properties might be impacted by the possibly small number of cloud condensation nuclei on ancient Mars.

The model was initialized with a globally averaged surface pressure of 500 mb of CO_2, and varying amounts of initial water vapor content ranging from ten precipitable microns up to a precipitable meter. The initial atmosphere and ground temperature were isothermal, equivalent to the temperature the saturation water vapor pressure was calculated at, in order to avoid significant supersaturation in the first model step. We also tested sensitivity of the resulting climate to the polar cap albedo, cloud particle sizes, and the efficiency to convert cloud water into precipitation. The factor B in Table 3.4 controls the rate of conversion of cloud water to precipitation as discussed below. In each simulation, the model was allowed to spin up for 3 Martian years, and the results are taken from subsequent model years. Water clouds are radiatively active in all simulations. Additionally, cloud fraction was set to unity in the radiative transfer calculations in some simulations to investigate its importance. In these cases, a computed cloud fraction was still allowed in the cloud water physics, so that clouds that do not saturate their respective grids can evaporate, reducing precipitation, and prolonging the lifetime of atmospheric water.

3.5.2 Simulation Results

A summary of the conditions and results of our simulations of the "faint young sun" climate on Mars is shown in Table 3.3. The results are categorized in Table 3.4 into three groups: cold climates that end with CO_2 condensing to form a polar cap, and a globally averaged surface temperature near 215 K; mild climates that end with a temperature near 245 K; and warm climates that end with a temperature near 265 K.

Case name	**Initial temperature**	**Initial water (pr-μm)**	**Cap albedo**	**Auto-conversion factor (*B*)**	**Cloud particle sizes**	**Fractional clouds in RT**	**Result**
Base	230 K	1000	0.4	1.0	1-10 μm	Yes	Cold
1	273 K	1e5	0.4	1.0	1-10 μm	Yes	Cold
2	300 K	5.4e5	0.4	1.0	1-10 μm	Yes	Cold
3	230 K	1000	0.4	1.e-2	1-10 μm	Yes	Cold
4	300 K	5.4e5	0.4	1.e-2	1-10 μm	Yes	Cold
5	230 K	1000	0.4	1.0	10 μm	Yes	Cold
6	300 K	5.4e5	0.4	1.e-1	10 μm	Yes	Cold
7	180 K	1	0.4	1.e-2	10 μm	Yes	Mild
8	200 K	15	0.4	1.e-2	10 μm	Yes	Mild
9	230 K	1000	0.4	1.e-2	10 μm	Yes	Mild
10	273 K	1e5	0.4	1.e-2	10 μm	Yes	Mild
11	300 K	5.4e5	0.4	1.e-2	10 μm	Yes	Mild
12	230 K	1000	0.4	1.0	10 μm	No	Cold
13	230 K	1000	0.4	1.e-1	10 μm	No	Mild
14	180 K	1	0.4	1.e-2	10 μm	No	Warm
15	200 K	15	0.4	1.e-2	10 μm	No	Warm
16	230 K	1000	0.4	1.e-2	10 μm	No	Warm
17	300 K	5.4e5	0.4	1.e-2	10 μm	No	Warm
18	230 K	1000	0.4	1.e-2	1-10 μm	No	Cold
19	180 K	1	0.6	1.e-2	10 μm	No	Cold
20	200 K	15	0.6	1.e-2	10 μm	No	Cold

21	230 K	1000	0.6	1.e-2	10 μm	No	Warm

Table 3.4. Parameters and results for ancient climate simulations.

Plots of typical results for the annually averaged surface temperature for each case are shown in Fig. 3.12.

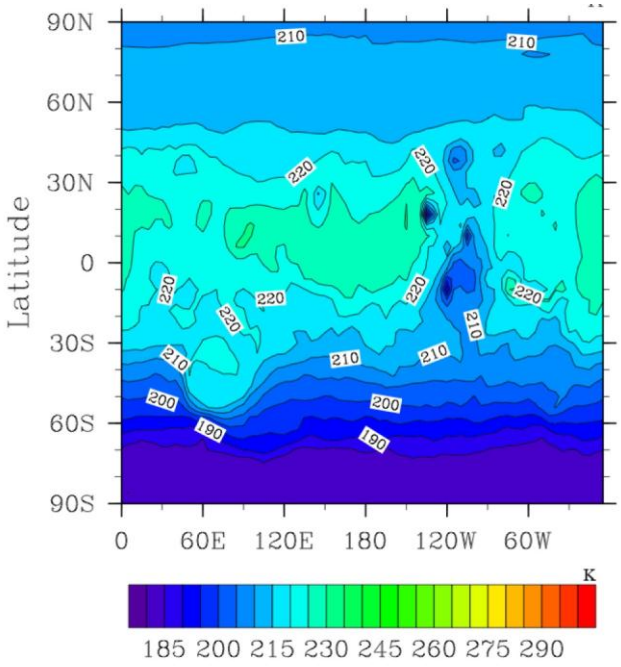

Figure 3.12a. Annually averaged surface temperature for cold (case 5) simulations.

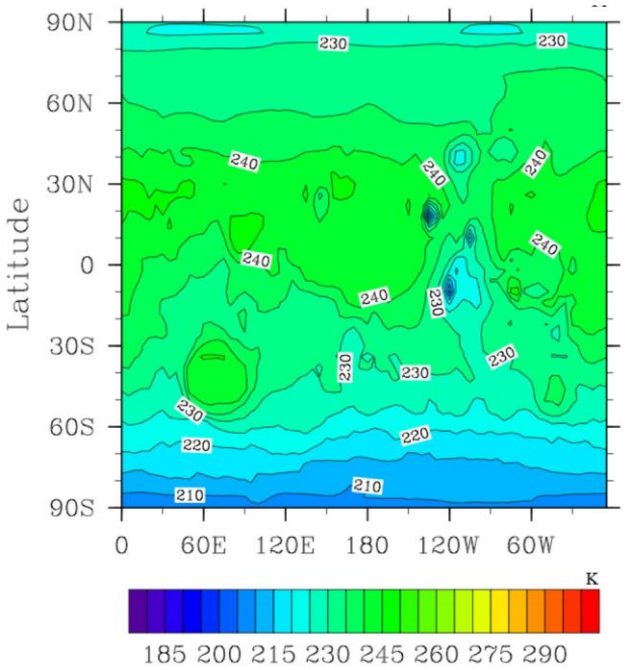

Figure 3.12b. Annually averaged surface temperature for mild (case 9) simulations.

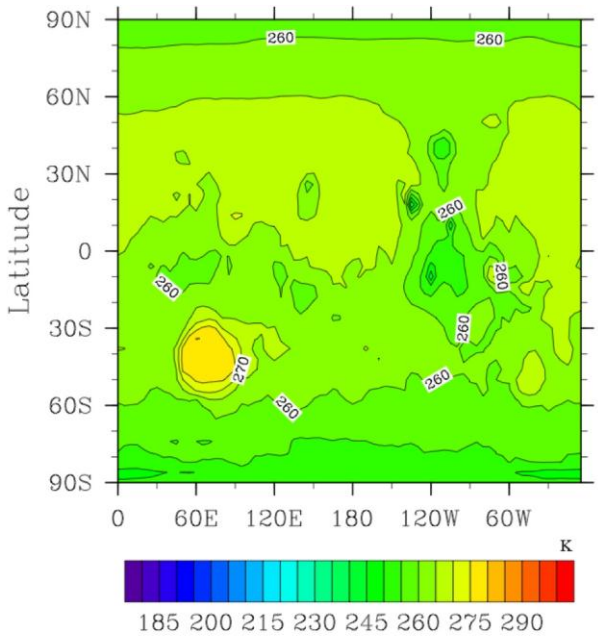

Figure 3.12c. Annually averaged surface temperature for warm (case 17) simulations.

In the cold cases (Fig. 3.12a is an example from Case 5 of Table 3.4) the maximum annually averaged surface temperature at any location is about 220 K,

decreasing as permanent polar caps form, the atmosphere collapses, and more of the planet is covered in CO_2 ice. The mild climates (Fig. 3.12b is an example from Case 9 of Table 3.4) are stable to atmospheric collapse, but only have maximum annually averaged surface temperatures near 245 K. In the warm cases (Fig. 3.12c is an example from Case 17 of Table 3.4), the globally averaged surface temperature is several degrees below the melting temperature of ice, but several areas of the planet, including the Hellas region and the tropics have annually averaged temperatures near melting.

There are three conditions that favor warm solutions, as well as special initial conditions. The needed initial conditions are that the planet start with a substantial amount of water in the atmosphere, or with surface ice that has a high temperature, for example because it has low albedo. We will discuss these conditions further in the conclusion to this paper.

The first condition favoring warm temperatures is ice crystals sizes around 10 μm, rather than being smaller. The typical radius of optically thin cirrus on Earth is about 10-20 μm (Davis et al., 2010). Smaller particles increase the visible optical depths of the clouds relative to their infrared optical depths and cause them to reflect more sunlight to space, which makes them less likely to warm the planet.

The second condition that leads to warm temperatures is low auto-conversion efficiency, or in other words a slow conversion of cloud to precipitation. This effectively increases the lifetime of water in the atmosphere, allowing thicker clouds to form. In order to produce significant clouds in this dry model we have adjusted the precipitation rate to be very low by using the factor B (Table 3.4), to reduce the auto-conversion factors discussed previously. The lifetime of water vapor is discussed further below.

The third condition favoring warm temperatures occurs when the fractional cloud cover is assumed to be near unity in the radiative transfer model. Spreading the cloud water over a large area reduces the cloud albedo, and also prevents "radiative windows to space," which would cool the planet. On Earth thin cirrus clouds are often continuous over vast areas, and occur with high frequency, though they are often too faint to see visually. These clouds are generally poorly represented in numerical models because they are often only hundreds of meters thick in the vertical, though they may extend thousands of kilometers horizontally. The following section will discuss the results for warm Mars in more detail, and describe the conditions required for a warm climate.

The model we are considering is inherently dry, because there are limited water reservoirs, for instance there are no lakes or seas. Table 3.5, and Fig. 3.13 illustrate the components of the Martian hydrological cycle for the cases considered here, and for current Mars.

Simulation	Current	Cold (Case 5)	Mild (Case 9)	Warm (Case 17)
Initial Atmospheric Water (kg)	1.44E+12	1.44E+14	1.44E+14	7.80E+16
Water Vapor (A) (kg)	9.95E+11	7.20E+12	4.25E+13	1.40E+15
Cloud Mass (A) (kg)	1.09E+11	5.08E+11	5.84E+12	3.23E+13
Surface Water (A) (kg)	1.44E+15	1.51E+15	1.49E+15	6.56E+15
Precipitation (T) (kg/yr)	2.24E+13	1.33E+13	3.39E+13	1.82E+15
Precipitation (T) (cm/yr)	0.015	0.009	0.023	1.26
Surface Evaporation (T) (kg/yr)	2.19E+13	1.38E+13	3.69E+13	1.56E+15

Runoff (T) (kg/yr)	1.88E+11	8.69E10	1.88E+11	1.79E+14
Drainage (T) (kg/yr)	~0.0	~0.0	~0.0	3.01E+14
Atmospheric Water Lifetime (days)	33	389	955	515

Table 3.5. Annual averages (A) or annual totals (T) for water per Mars year.

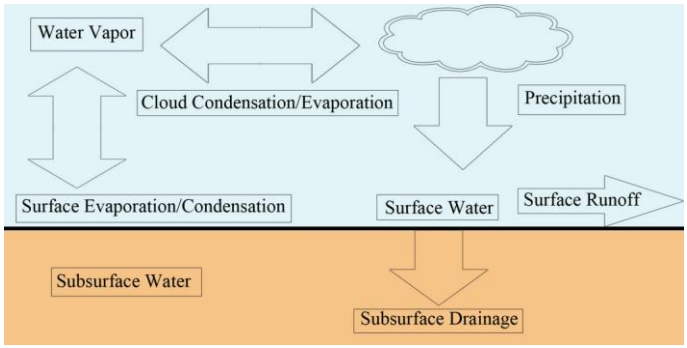

Figure 3.13. A diagram of the reservoirs, sources, and sinks of water in the model.

The reservoirs and sinks are: surface and subsurface water, including polar caps, seasonal snow, and soil water, providing an initial global water reservoir of approximately 4.5×10^{15} kg; surface runoff; subsurface drainage; water vapor; and clouds. Surface water always dominates, followed by water vapor. Clouds have 1-10% of the water vapor mass. Because the polar caps do not decrease in mass by assumption, they can provide an infinite source of water.

The processes that move water between the reservoirs are: evaporation from the surface reservoirs, including from the polar caps; precipitation; condensation to and from clouds; runoff; and drainage. The surface evaporation in Table 3.5 represents the net sublimation and condensation from surface reservoirs (positive represents net sublimation). At equilibrium, the annual surface evaporation would equal precipitation.

Water is free to infiltrate the soil, and is transported by diffusion. Some subsurface water is lost in the model through drainage out of the bottom of the soil. Water can also be lost when runoff occurs. Runoff occurs in the model when liquid water reaches the surface in the form of precipitation, or as melt water from the bottom of snow packs. Runoff can also occur when the snow water equivalent exceeds 1000 kg m^{-2}, which is a model constraint. This constraint is imposed because the snow model only contains 5 vertical levels, with the top 4 levels having a maximum thickness of approximately 40 cm, so the bottom level can become very thick. Runoff can be negative when there is a net loss of water at the polar cap. Since the polar cap is assumed to be an infinite source of water, negative runoff is used to represent a replenishment of the cap mass. This allows the hydrologic cycle to be closed.

The lifetime of the water in the atmosphere in steady state is equal to the total amount of water vapor plus cloud divided by the production rate of water vapor (mainly by sublimation from the polar caps), or divided by the precipitation rate. For the cases in Table 3.5, the production rate and precipitation rate are very close, suggesting the model is in steady state. The production rate of water is controlled primarily by the temperature of the evaporating polar cap, although the net production rate can be reduced by the condensation of water vapor in the polar night directly onto the ice. The loss rate of water is controlled by the precipitation rate as snow and rain. Table 3.5 lists the lifetimes of water for the various cases. On Earth it is about 8 days, but in all of the warm cases for Mars the lifetime is longer.

Table 3.5 also shows the precipitation rates for the various cases considered. On Earth the precipitation rate is about $5x10^{17}$ kg/yr, which is equivalent to a layer of

thickness about 1 m per Earth year. The annual precipitation in Case 17 is less that 0.5% of the terrestrial precipitation, even though the Martian year is about twice as long as the Earth year. However, due to the smaller size of Mars, the precipitation is more than 1% of the average rainfall per unit area on Earth.

3.5.3 Base Case

First we describe the base case simulation, whose parameters are given by the first entry in Table 3.3, and whose surface temperatures are given in Table 3.4, and in Fig. 3.12a. This simulation, along with all simulations that include fractional clouds in the radiative transfer, ends in the cold state. Our simulations indicate that this climate is not stable to atmospheric collapse due to CO_2 condensation. An extended 60 Mars year run (Fig. 3.14) shows that the atmosphere is collapsing onto the polar caps, which could continue until the pressure is well below that currently on Mars since the solar constant is lower in these runs than on current Mars, or until the planet is covered in CO_2 ice, and a balance is met between the CO_2 frost temperature, the atmospheric CO_2, and the solar insolation.

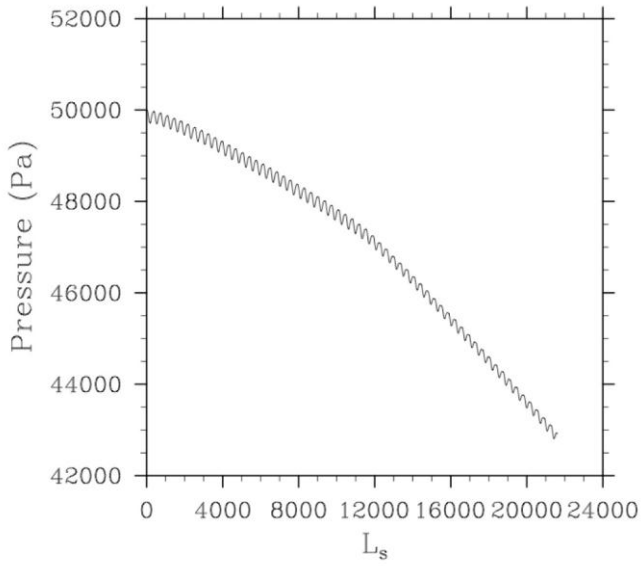

Figure 3.14. Globally averaged surface pressure vs. time (L_s) for the base case scenario.

At equilibrium the global average surface temperature should reflect the solar insolation. The balance equation would then be $(1\text{-}A)*S=\sigma T_s^4$. Where S is the solar insolation averaged over the planet, A is the albedo of ancient Mars, and T_g is the ground temperature. Assuming an albedo of 0.25, and a globally averaged insolation of 110 W m^{-2}, solving for T_g yields an equilibrium ground temperature of 195 K. For a CO_2 snowball Mars and an albedo of 0.6, the equilibrium ground temperature is 167 K, with a corresponding saturation vapor pressure of 70 mb, approximately 10 times the current surface pressure.

3.5.4 Warm solutions

Segura et al. (2008) used a 1D model to show that the energy and water released by large impacts could sustain a warm climate for extended periods of time from

greenhouse warming from water alone, without clouds. We performed tests with increased amounts of initial water in the atmosphere to see if a warm solution could be approached. These tests differed from the simulations of Segura et al. (2008), because we did not assume that the injected water was hot, nor was there a hot debris layer on the surface. Therefore, we did not have a warm period while the atmosphere and hot impact debris layer radiated away the impact energy. We found that simulations of up to a precipitable meter of initial water at 300 K did not yield stable warm climates. The surface temperature would initially be warm at just above 300 K, but the temperature quickly fell to 210-215 K during the second year.

Segura et al., (2008) also showed that the presence of radiatively active water ice clouds could lead to a stable climate with temperatures near 250K. Clouds then become the next obvious stage of the hydrologic cycle to test. To better understand the effects of clouds, three parameters were varied: the auto-conversion efficiency of cloud mass to precipitation (controlled by the B parameter in Table 3.4), cloud particle size, and allowing or forbidding cloud fractional grid saturation in the radiative transfer. Various combinations of these three factors were tested, and the results are summarized in Table 3.4.

Little is known about the precipitation process on Mars due to lack of data. It is possible that coalescence and collection are less efficient on Mars because of extremely low temperatures, low pressures, and especially low numbers of cloud particles due to the relatively small number of ice nuclei in the atmosphere. In the simulations performed, the auto conversion rate defined in Eq. 3.6 was reduced by up to a factor (B in Table 3.4) of 100 to examine the sensitivity to precipitation rates, so that $E_i^* = B * E_i$.

For clouds, whether they heat or cool the surface is very sensitive to the particle size, especially in the region between 1-10 μm. Since cloud opacity varies inversely with particle size, the clouds with smaller particles will have higher opacities compared to clouds with larger particles. If visible wavelength opacities are high a larger fraction of the incoming solar radiation is either scattered or reflected, resulting in less energy reaching the surface, and thus more cooling. Since ice is absorbing in the infrared, even small optical depths at infrared wavelengths can efficiently alter the long wave radiation balance. All simulations that ended mild or warm had cloud particle sizes of 10 μm.

Figure 3.15 shows zonally averaged values for cloud water concentration (3.15a), atmospheric temperature (3.15b), and total grid average cloud optical depth in the 800-875 cm^{-1} waveband (3.15c) at L_s=120° from Case 17 in Table 3.4, one of the warm simulations. L_s=120° was chosen because cloud forcing has the greatest impact at around this time (the ground temperature for this run was shown in Fig. 3.12c).

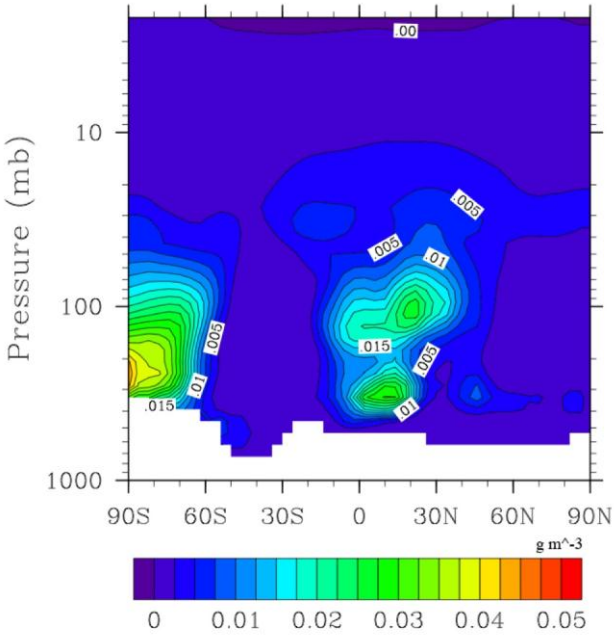

Figure 3.15a. Zonally averaged cloud water concentration (g m^{-3}) at L_s=120° for case 17 of Table 3.4.

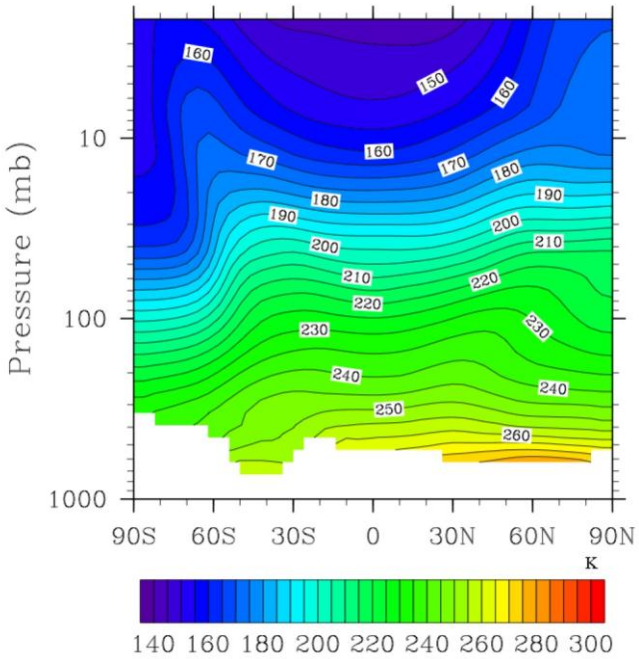

Figure 3.15b. Zonally averaged temperature at L_s=120° for case 17 of Table 3.4.

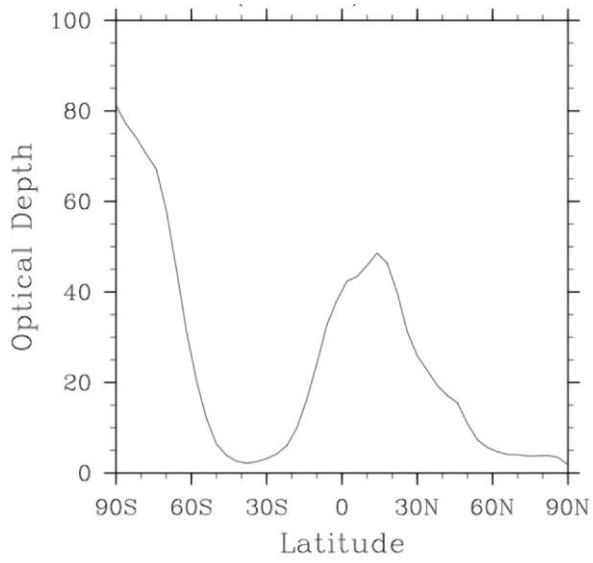

Figure 3.15c. Zonally averaged cloud optical depth between 800-875 cm^{-1} at L_s=120° for case 17 of Table 3.4.

The thickest clouds are low and found over the South Pole, which is coming out of winter, and these warm the polar surfaces by radiating infrared light down to the ground. However, the equatorial clouds also have a large effect on the cloud forcing, and these are very high in the atmosphere. The atmospheric temperature where the clouds are thickest is approximately 200 K. At similar temperatures on Earth, ice particles are typically 10-20 μm in size (Jensen et al., 1996), making this not an unreasonable assumption.

Whether or not sub-grid effects of clouds are considered in the radiative transfer seems to be a key factor in achieving warm temperatures in the model. All of the stable warm climates required the assumption that clouds always fill the grid. Figure 3.16 shows a comparison between the globally averaged cloud forcing calculated for grid-fractional clouds (3.16a, Case17 of Table 3.4) and full-grid clouds (3.16b Case 17 of Table 3.4) over the year.

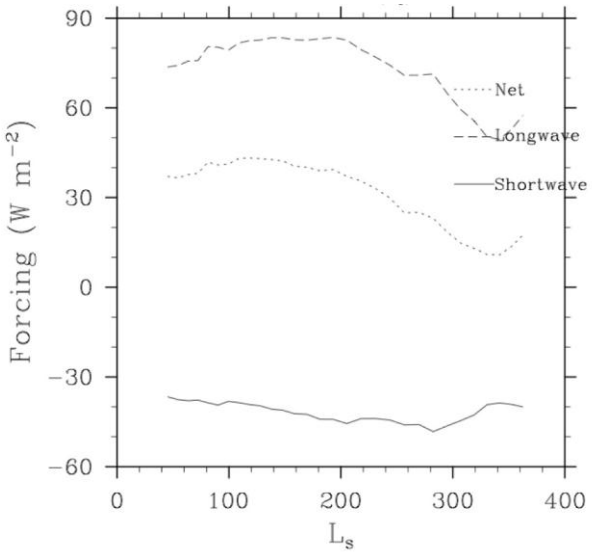

Figure 3.16a. Globally averaged cloud forcing vs. time (L_s) for case 17 of Table 3.4 for grid-fractional clouds.

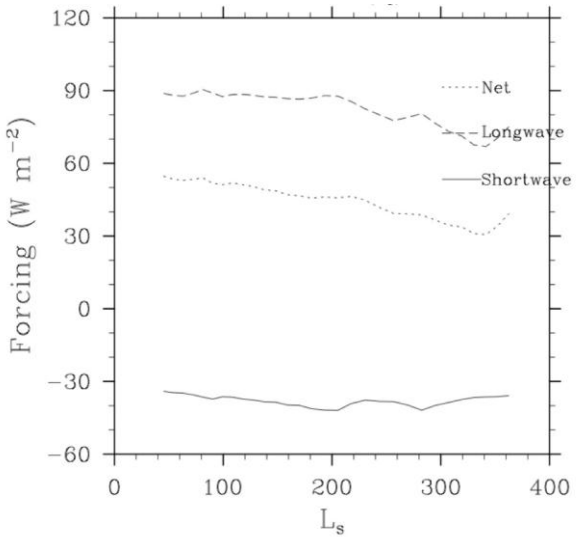

Figure 3.16b. Globally averaged cloud forcing vs. time (L_s) for case 17 of Table 3.4 for full-grid clouds.

In both cases the clouds produce a positive net forcing. The net forcing is consistently between 30-50 W m^{-2} throughout the year for full-grid clouds, compared to only 10-40 W m^{-2} for fractional clouds, a difference of 60-90% (of the full-grid cloud forcing) in the net cloud forcing from the fractional clouds to the full-grid clouds. Figures 3.15a and 3.17a show the zonally averaged cloud water concentrations (g m^{-3}) at L_s=120° and L_s=300°, which represents two transition seasons in terms of cloud forcing, for Case 17 of Table 3.4.

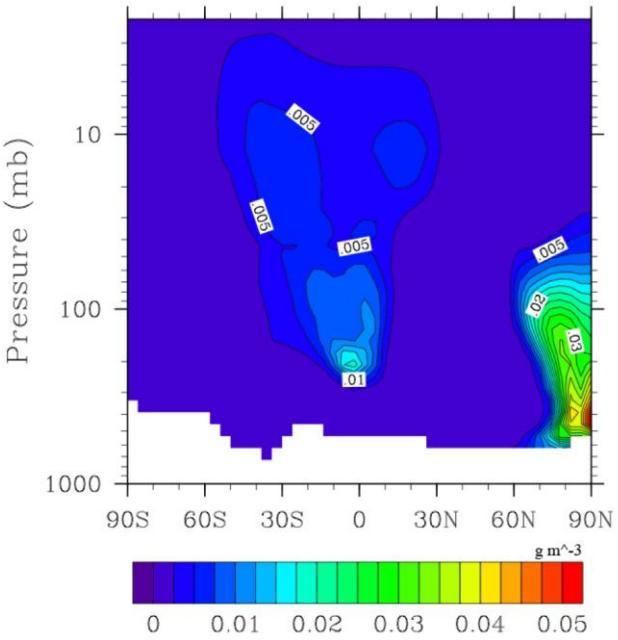

Figure 3.17a. Zonally averaged cloud water concentration (g m^{-3}) at L_s=300° for case 17 of Table 3.4.

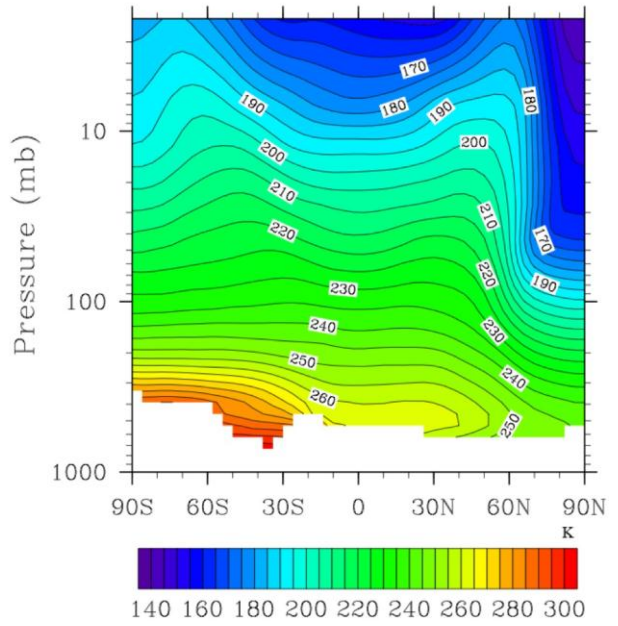

Figure 3.17b. Zonally averaged temperature at L_s=300° for case 17 of Table 3.4.

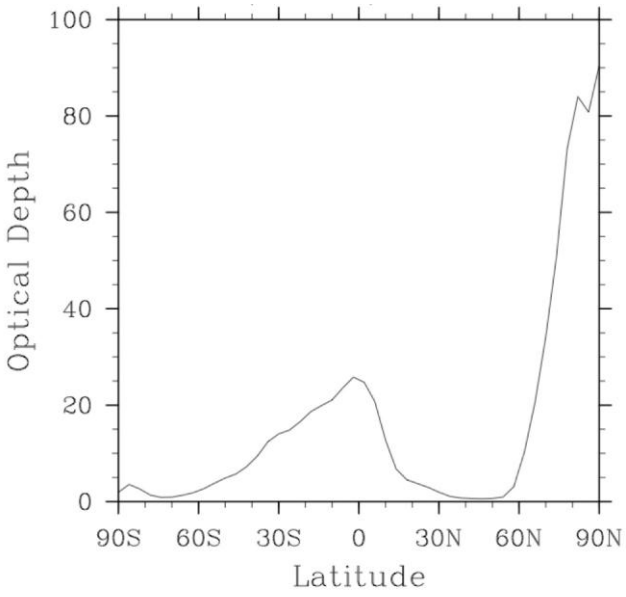

Figure 3.17c. Zonally averaged cloud optical depth between 800-875 cm^{-1} at L_s=300° for case 17 of Table 3.4.

Figures 3.17b,c further illustrate the temperature, and cloud optical depth at Ls=300. These plots, accompanied by the zonally averaged cloud forcing versus time (Fig. 3.18) show how the cloud distribution affects the global cloud forcing averages.

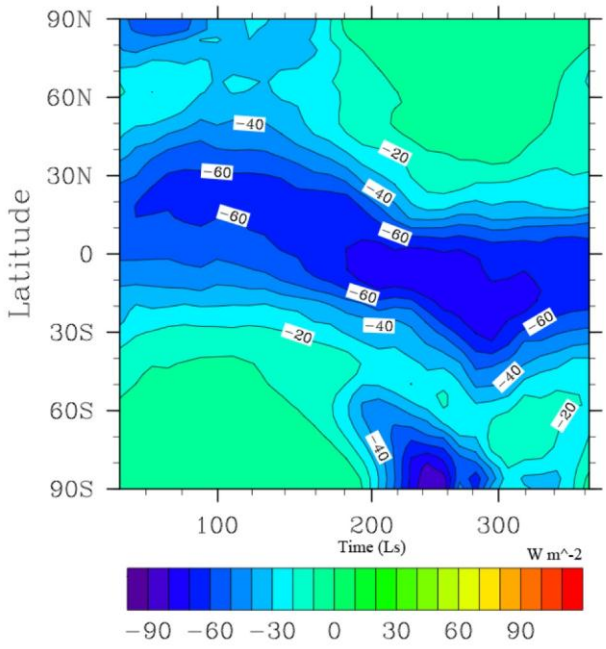

Figure 3.18a. Zonally averaged full-grid cloud forcing vs. time (L_s) for case 17 of Table 3.4 in the shortwave cloud forcing.

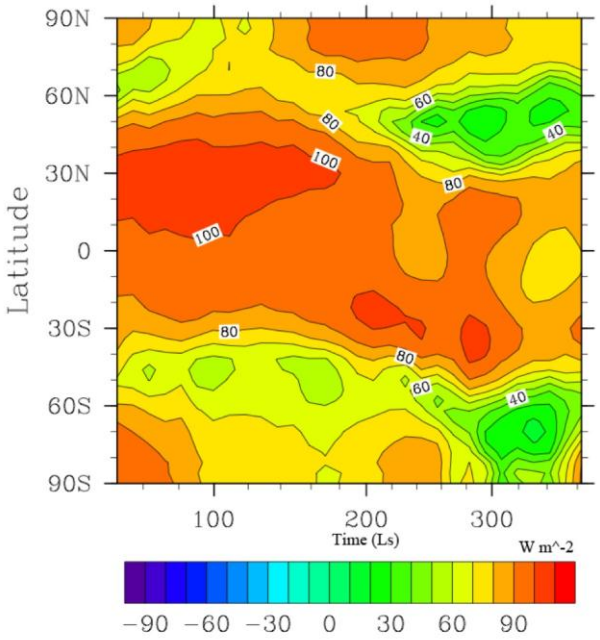

Figure 3.18b. Zonally averaged full-grid cloud forcing vs. time (L_s) for case 17 of Table 3.4 in the longwave cloud forcing.

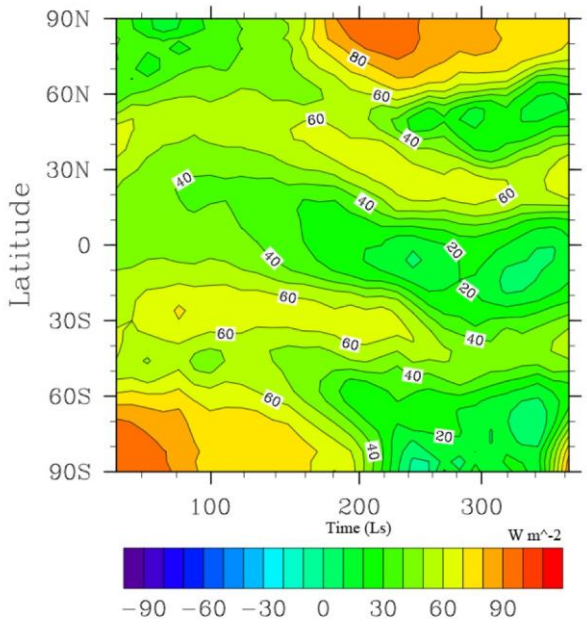

Figure 3.18c. Zonally averaged full-grid cloud forcing vs. time (L_s) for case 17 of Table 3.4 in net cloud forcing.

At both times of year, a thick cloud is present near the surface above the winter pole, and another thick cloud is present high in the atmosphere in the tropics. The polar clouds, which contribute greatly to the longwave cloud forcing (Fig. 3.18b, up to 90 W m^{-2} warming), have very little impact on the shortwave cloud forcing (Fig. 3.18a) due to being formed during polar night. The tropical clouds contribute to the shortwave cloud forcing (up to 70 W m^{-2} cooling), but their optical depths and altitudes are such that the longwave warming is always larger than the shortwave cooling, leading to net warming by clouds (Fig. 3.18c).

The difference in cloud forcing between fractional clouds and full clouds is significant under these warm conditions. Figure 3.19 describes the zonally averaged cloud forcing difference between the two radiative cases (full – fractional, Case 17 of Table 3.4) versus time in the shortwave (Fig. 3.19a), longwave (Fig. 3.19b), and the net (Fig. 3.19c) forcing.

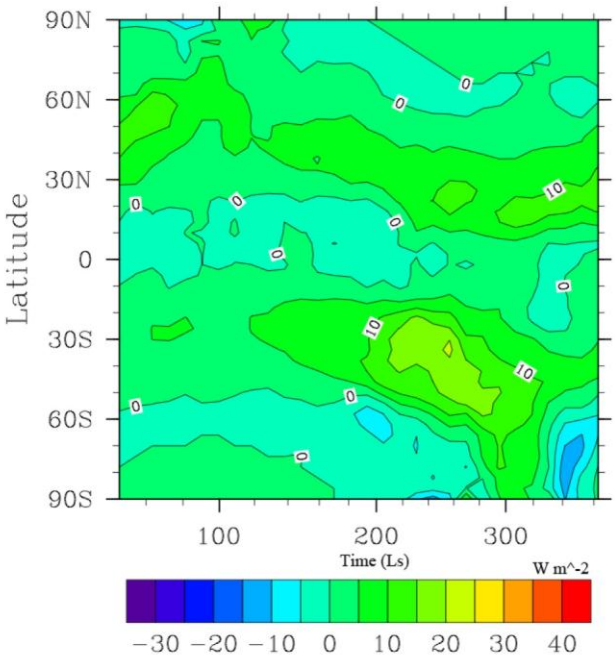

Figure 3.19a. Zonally averaged full-grid cloud forcing difference (full - fractional) vs. time (L_s) for case 17 of Table 3.4 in the shortwave cloud forcing.

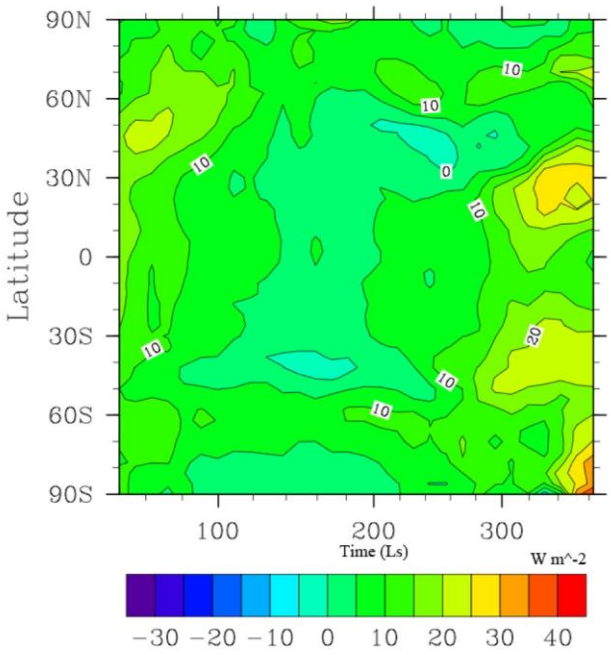

Figure 3.19b. Zonally averaged full-grid cloud forcing difference (full - fractional) vs. time (L_s) for case 17 of Table 3.4 in the longwave cloud forcing.

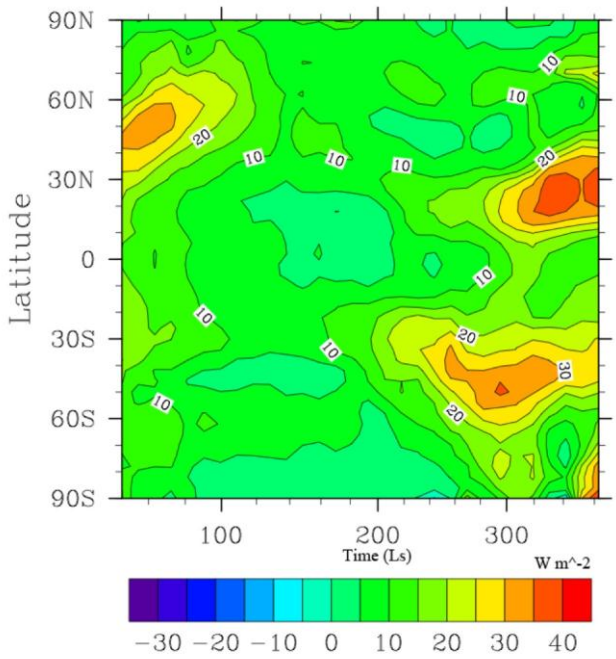

Figure 3.19c. Zonally averaged full-grid cloud forcing difference (full - fractional) vs. time (L_s) for case 17 of Table 3.4 in net cloud forcing.

These values were calculated during the same simulation, calculating the radiative transfer through the clouds assuming fractional clouds, and full-grid clouds for comparison, using the heating rates calculated with the full-grid clouds in the model. In both shortwave and longwave, the full clouds tend to provide more positive forcing compared to the fractional clouds, leading to a higher net forcing in the full case of approximately 20 W m^{-2}. The increased cloud forcing in the longwave can simply be explained by the fact that clouds filling a cell will interact with all radiation passing through the level; and since clouds are efficient absorbers in the longwave, less radiation can escape to space even if clouds are thinner. The full-grid shortwave cloud forcing is less than the grid-fractional forcing because the albedos are not as high for lower optical depth clouds, which occur when the cloud mass is distributed over the grid cell.

A comparison of the zonally averaged cloud optical depth between 800-875 cm^{-1} vs. L_s for cases 5, 9, and 17 are shown in Fig. 3.20.

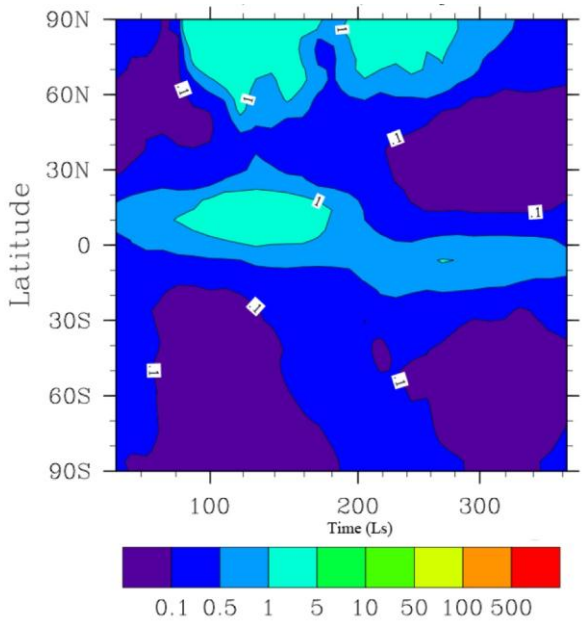

Figure 3.20a. Zonally averaged cloud optical depth between 800-875 cm^{-1} vs. time (L_s) for case 5 of Table 3.4.

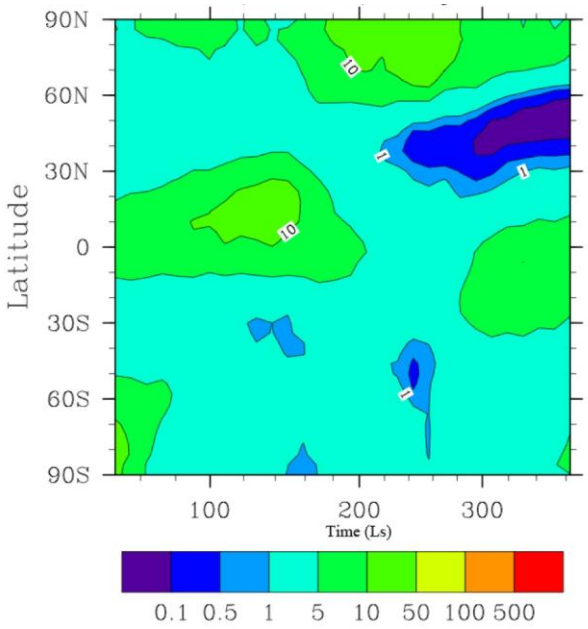

Figure 3.20b. Zonally averaged cloud optical depth between 800-875 cm^{-1} vs. time (L_s) for case 9 of Table 3.4.

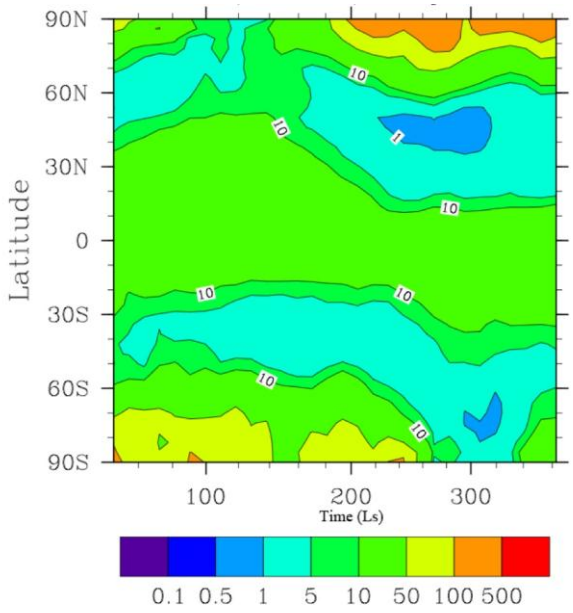

Figure 3.20c. Zonally averaged cloud optical depth between 800-875 cm^{-1} vs. time (L_s) for case 17 of Table 3.4.

In the cold Case 5 (Fig. 3.20a), the atmosphere is dry, with a maximum cloud optical depth of 1-5 during northern summer. In the mild Case 9 (Fig. 3.20b), the maximum cloud optical depth is above 10, and the minimum optical depth during northern summer is 1-5, equivalent to the maximum in Case 5. In the warm Case 17 (Fig. 3.20c), the tropics are covered by clouds of optical depth greater than 10 throughout the year, and the poles have clouds of optical depth greater than 50 during the wintertime. Table 5 shows that reducing *B* from 1.0 to 0.01 between Cases 5 and 9 increased the atmospheric water lifetime by a factor of 2.5. The resulting clouds were optically thicker by about a factor of 10, which warmed the surface, allowing more sublimation from the polar cap. Comparing the cloud forcing to the cloud optical depths for Case 17 (Fig. 3.18c, 3.20c), it is apparent that the thick polar clouds provide significant warming to the poles during the wintertime. This results in warmer temperatures over the cap, so that the polar temperatures rarely fall below the CO_2 frost point, allowing water sublimation from the water-ice cap

throughout the year. Over the rest of the planet, the most warming occurs when the cloud optical depth is between 5-10, typically in the subtropics. In the tropics, where the cloud optical depths are greater than 10, there is still a positive net forcing, but it is smaller than compared to the subtropics. These subtropical clouds are also where the difference between the fractional and full-grid clouds has the most significant impact on the net cloud forcing and planetary albedo. Figure 3.21 shows planetary albedo for Case 17 and the difference between the planetary albedos for the full-grid clouds and fractional clouds for Case 17.

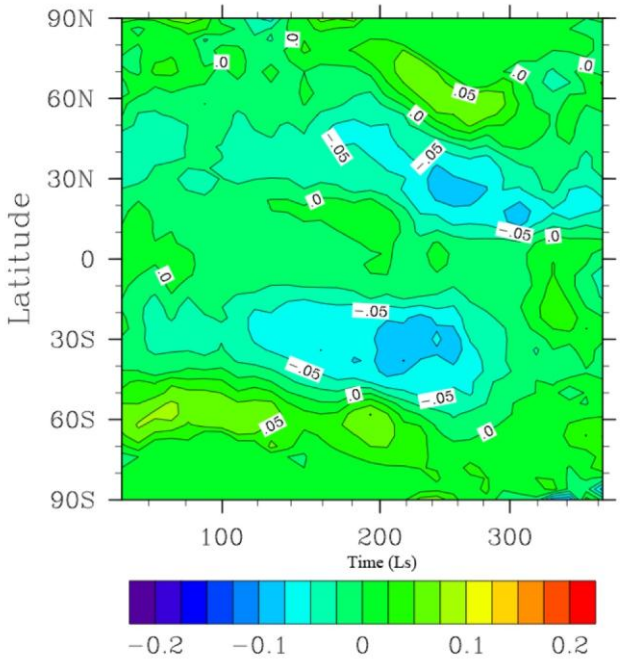

Figure 3.21. Zonally averaged planetary albedo difference (full - fractional) vs. time (L_s) for case 17 of Table 3.4.

Comparison of Fig. 3.21 with Fig. 3.20c shows that the sub-gridscale radiative effects of clouds make the most impact when the cloud optical depth is between 1-10. Below this, the clouds are tenuous enough that they have little impact on the radiation, and above this,

the clouds are massive enough to fill the grid. The reason why the stable warm state cannot be achieved with the fractional clouds, is because polar clouds tend to dissipate during the summer, and subsequently cannot grow to be very optically thick during the winter due to the diminished amount of warming from the fractional clouds, and reduced sublimation from the polar cap. This reduces the yearly total amount of water released into the atmosphere, which in turn leads to less water available for clouds across the globe.

The additional forcing of 20 W m^{-2} provided by the full clouds is what tips the system into the warm climate. Figure 3.22 is a compilation of the globally averaged net cloud forcing versus time for selected cases (5, 9, 12-14, 17-20 in Table 3.4), including results from cold climates, mild climates, and warm climates.

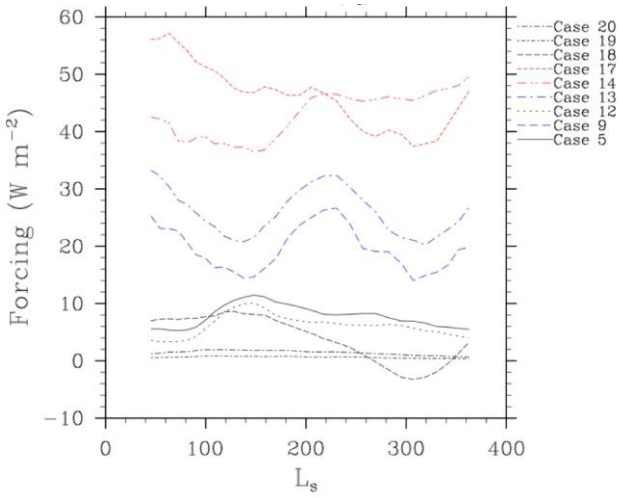

Figure 3.22. Comparison of globally averaged net cloud forcing vs. time (L_s) for various cases.

The lines are designated by the Case numbers in Table 3.4. Each regime, cold, mild, and warm, clearly separates into three distinct groups of net cloud forcing. The cold climates have globally averaged cloud forcing values of less than 10 W m^{-2}. The mild climates

have cloud forcing values of 20-30 W m^{-2}. Finally, the warm climates tend to have cloud forcing values greater than 40 W m^{-2}. This indicates that there is a critical amount of forcing (between 30-40 W m^{-2}), that when reached, can create a stable, warm climate.

3.5.6 Effects of Initial Atmospheric Pressure

The previous section described how Mars could potentially have had a warm climate sustained by the hydrologic cycle and the resulting cloud forcing, even with a reduced solar constant. However, the present Martian climate is cold and dry, despite a higher solar constant than in the past. Therefore the thicker CO_2 atmosphere must assist the warming in some way. It will directly warm the planet through the increased greenhouse warming from the thicker atmosphere. It will also indirectly support warming because a denser atmosphere will have a higher volumetric heat capacity, meaning that once clouds have formed, more energy is required to warm the atmosphere to the point where the clouds will dissipate, and perhaps more importantly the atmosphere can more easily carry heat to the poles from the tropics. Increased cloud lifetimes will lead to increased cloud forcing, and thus more warming, and warmer poles will lead to more water vapor entering the atmosphere.

The plots in Fig. 3.23 show the annually averaged surface temperatures after 4 years for surface pressures of 50 mb, 100 mb, 250 mb, and 1000 mb, all with 1000 pr-μm initial atmospheric water, and assuming cloud fraction 1 (comparable to Case 16 of Table 4).

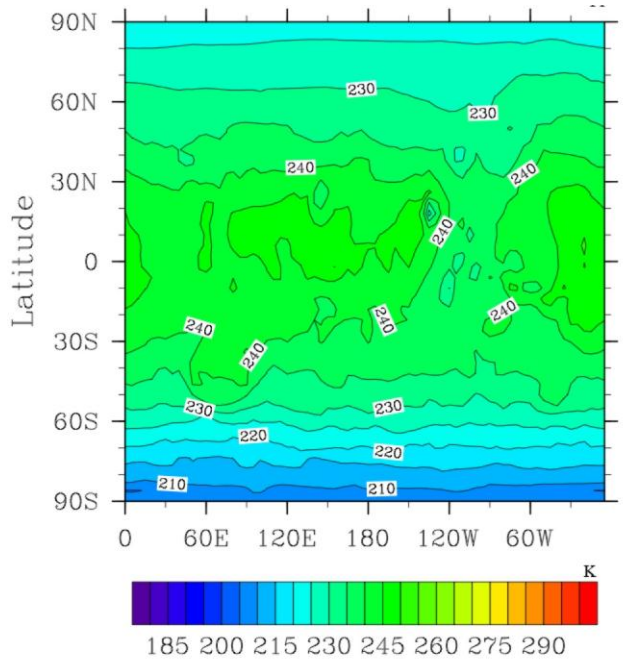

Figure 3.23a. Annually averaged surface temperature with 50 mb of CO_2.

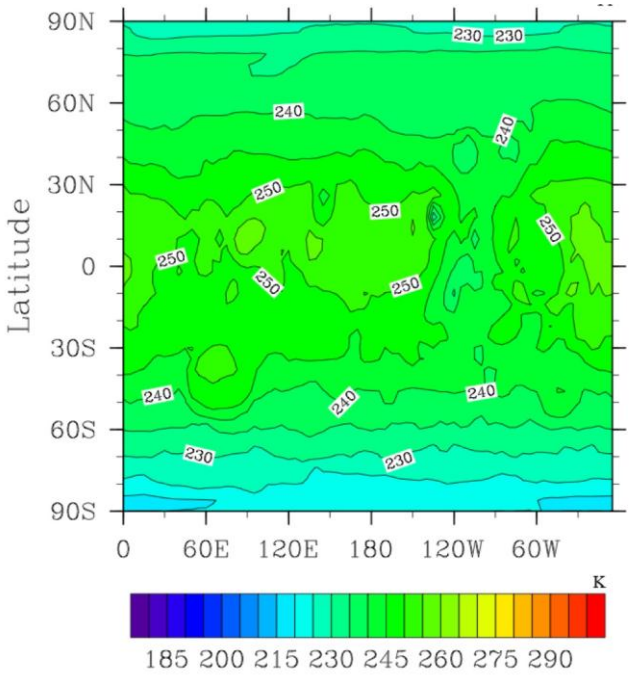

Figure 3.23b. Annually averaged surface temperature with 100 mb of CO_2.

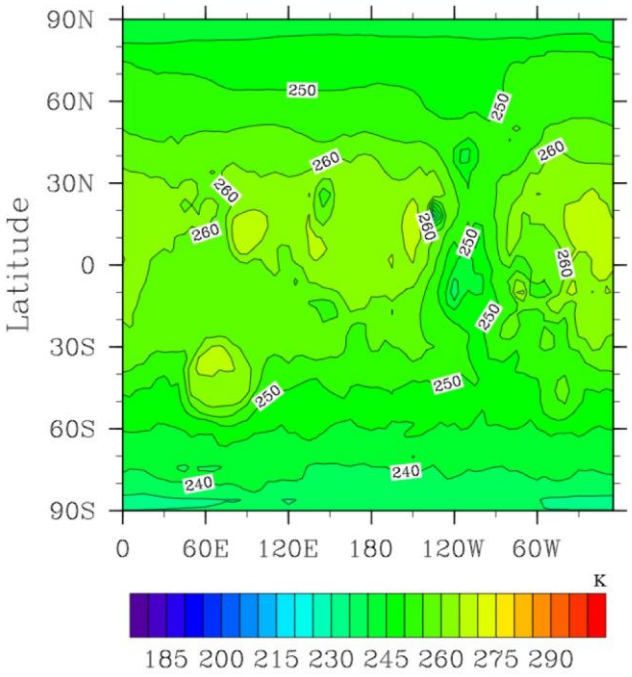

Figure 3.23c. Annually averaged surface temperature with 250 mb of CO_2.

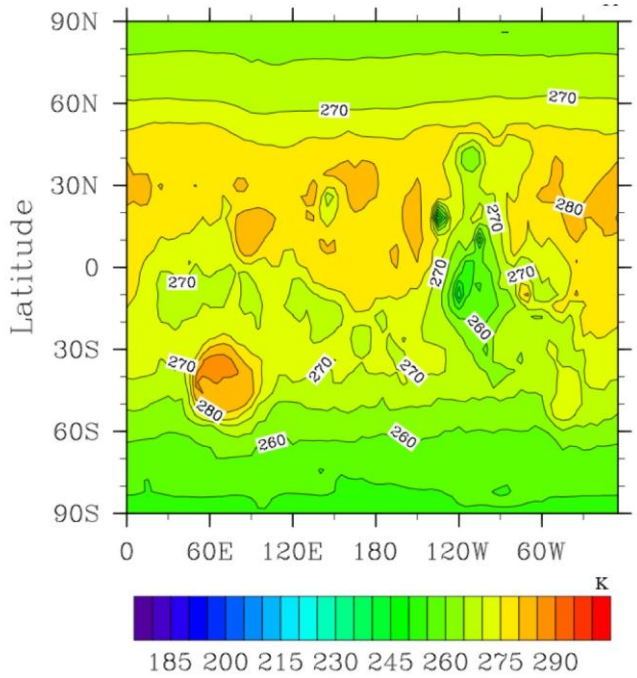

Figure 3.23d. Annually averaged surface temperature with 1000 mb of CO_2.

As expected, the temperatures are warmer than the 500 mb case discussed previously with 1000 mb, and cooler for less CO_2. With 1000 mb of CO_2, the highest annual surface

temperatures are 285 K, with most of the tropics above 275 K. In contrast, at and below 250 mb of CO_2, the annual temperatures are never above 270 K, indicating that the minimum surface pressure required for annual surface temperatures above freezing is between 250-500 mb.

The critical surface pressure is related to there being less CO_2 to act as a greenhouse gas, as well as the atmosphere not having enough mass to transport a significant amount of heat from the equator to the pole in order to sustain the water vapor. This can be seen in a comparison of the zonal mean surface temperature at L_s=300°, which is during northern winter (Fig. 3.24).

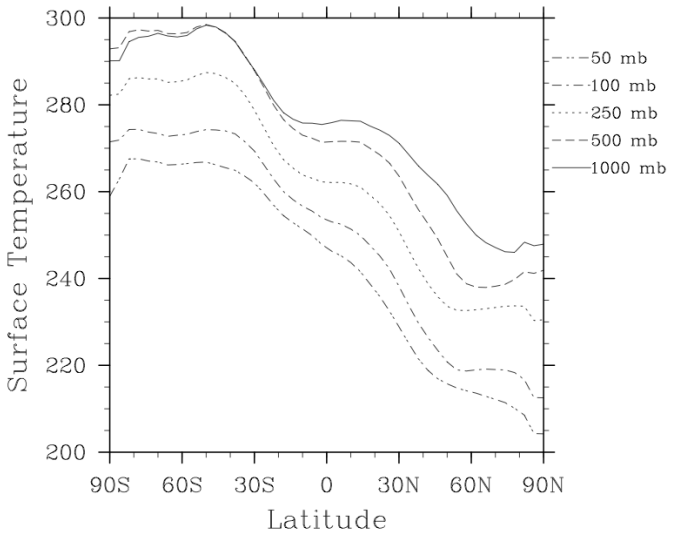

Figure 3.24. Zonal mean surface temperature (K) at various pressures for L_s=300°.

Figure 3.24 shows that for pressures below 250 mb, the equator to pole temperature gradient is approximately 10 K greater, and the polar temperatures are more than 20 K lower than at higher pressures. Colder polar temperatures cause the

sublimation rate of water to be lower, making it difficult to supply the atmosphere with water.

3.6 Conclusions

Urata and Toon (2012a) introduced a new Martian general circulation model, Mars CAM, adapted from the terrestrial NCAR Community Atmosphere Model. In this paper we discuss its hydrologic cycle, including the radiative effects of water-ice clouds. The most significant changes to the terrestrial CAM model for the hydrological cycle consisted of using a saturation vapor pressure equation for water over ice valid for typical Martian temperatures, adding fractional cloud and overlap consideration to the radiative transfer, as well as allowing the critical saturation for cloud formation to be larger than one, and to vary with temperature. The only sources of water were a prescribed water-ice polar cap, and an initial atmospheric water vapor content of 10 precipitable microns globally averaged for the current climate, and varying for the ancient climate.

Comparisons to TES observations (Smith, 2008) revealed that for the present climate while the water vapor column abundances could be reproduced by tuning the polar cap albedo, it was impossible to simultaneously duplicate the observed cloud opacities in the high summer latitudes without allowing for high supersaturation. In the "best-case" scenario (Fig. 3.7b), the peak water vapor column abundance was 65 pr-μm during northern summer, and few clouds were formed because we forced a high supersaturation poleward of 40° during summer (Fig. 3.9). The ability to reproduce

observations by changing a single parameter suggests that the problem of forming clouds that are too thick over the pole stems from overlooking a process on Mars that makes cloud formation significantly more difficult at these times and locations, and not a fundamental issue with the transport of water itself (vapor or condensed). Similar high supersaturations are thought to occur on Earth at low temperatures (<180K), and moderate supersaturation does occur on Earth near 200k when nuclei are limited, or cloud surface areas are small. The question as to what might cause the supersaturation must be addressed with a cloud microphysical model that takes into account factors such as nucleation rates, growth rates, and nuclei concentration. Understanding nuclei concentration requires a temporally and horizontally varying dust field, and perhaps consideration of micrometeorites. However, understanding nucleation rates may require laboratory studies.

The simulations of a hypothetical ancient Martian climate (500 mb CO_2 atmosphere, 75% solar constant) show that the climate is very sensitive to the radiative effects of water-ice clouds. Differences in the assumptions about cloud particle sizes, auto-conversion rates, and sub-grid effects can drastically alter the climate over a range from very cold with carbon dioxide condensing to form a permanent polar cap, to warm, with some locations with annual average temperatures above the freezing point of water.

In the model for present day Mars, cloud particles are assumed to have a size between 1-10 μm that varies with height based on observations. For the 500 mb atmosphere simulations, the clouds form at high altitude where temperatures are near 200 K, a temperature at which terrestrial cloud particle radius values are observed to be larger than 10 μm. Using these larger particle sizes results in warmer temperatures.

The model we considered here has very limited sources of water, basically just the polar caps. In order to enhance the optical depth of clouds for such a dry atmosphere the rate of conversion of cloud mass to precipitation was reduced from terrestrial values. An increase of water lifetime (Table 3.5) can be sufficient to jumpstart a warm climate by providing greater cloud forcing. A microphysical model should be used to investigate both particle size and precipitation rate to better constrain their values.

One significant factor in creating a warm climate is the cloud cover fraction. Assuming a cloud fraction of 1 instead of a fractional cloud cover can result in a net cloud forcing difference of 10-20 W m^{-2} throughout the year, and significant warming. A cloud fraction of 1 allows less longwave radiation to escape freely to space, and reduces the cloud optical depth and albedo, allowing more sunlight to reach the surface. This increased surface radiation can make a significant difference over the ice cap during polar winter when the unity cloud fraction leads to enhanced warming of the surface compared to the lesser cloud fraction case. The warmer temperatures allow increased water sublimation, increasing the global atmospheric water content, and increasing the greenhouse warming provided by the hydrologic cycle. Cirrus clouds have been observed to extend horizontally up to 1000 km on Earth (Pfister et al., 2001), so high cloud fractions are not impossible. Simulations at higher resolution, for which the assumption of a cloud fraction of 1 is reasonable, could be performed to further investigate the relevance of the cloud fraction.

It is also noteworthy that appropriate initial conditions are needed to reach a warm climate. For example, starting with significant water in the atmosphere, which would happen after a large impact, can lead to a stable warm climate. Possibly water injections

from volcanic activity could also lead to a warm climate, but it is not clear that enough water could be injected rapidly enough. Having a dark polar cap could also lead to a warm climate, although it is not clear what mechanism would darken the cap. Possibly having a higher obliquity may lead to a warm climate by exposing polar ice to more sunlight, although we have not simulated that case. We have not yet considered the case of extensive oceans, or lakes. Lakes in the tropics could provide warm sources for water vapor, which might speed up the hydrological cycle. Oceans may also supply more water vapor, but if they freeze over the high albedo of the sea ice might cool the planet. We have also not considered the effects of CO_2 clouds. Forget and Pierrehumbert (1997) suggested that such clouds could also provide substantial warming in an early Martian climate. It is possible that CO_2 clouds, in conjunction with H_2O clouds could provide sufficient warming to relax some of the constraints found in this work.

There are several processes that might end the warm temperature climates we have discussed here. These include loss of the carbon dioxide to levels below 250 mb, transfer of water to subsurface reservoirs so that surface reservoirs cannot supply the atmosphere with sufficient water vapor, or perhaps changes in the orbital parameters leading to very cold polar temperatures.

We have shown here that it is possible to create above-freezing annual average temperatures over a wide region of the Martian tropics with greenhouse agents, water vapor and clouds, that are known to be present. This is the first time that any three dimensional model has yielded temperatures above freezing using a plausible value for carbon dioxide concentrations, and a self-consistent hydrological cycle. Future studies

should include more detailed cloud microphysics with full nucleation and precipitation, and at least some treatment for the sub-grid radiative effects of clouds.

In this study we investigated an inherently dry Martian climate, with only polar water sources. Geologic evidence suggests that Mars may have had a much more geographically widespread hydrological cycle. The widespread presence of surface water sources at equatorial and middle latitudes, possibly triggered by impacts, volcanic eruptions or perhaps high obliquity conditions, may allow a water vapor-cloud greenhouse to produce a much more vigorous hydrological cycle. Future studies of precipitation patterns in climate models in comparison with geologic data on the distributions of river systems would be of value.

Chapter 4. Effects of Oceans and High Obliquity on the Ancient Martian Climate

4.1 Noachian Valley Networks

As described in Chapter 3, the Noachian valley networks (Di Achille and Hynek, 2010) and the possible paleolakes they fed (Fassett and Head, 2008a) provide evidence for extensive surface fluvial activity and precipitation during the Late Noachian to Early Hesperian, approximately 3.5-3.9 Ga (Fassett and Head, 2008b; Hoke and Hynek, 2009). These valley networks extensively cover the Noachian terrain from 25°N near Arabia Terra, to 60°S below the Tharsis Rise, indicating global scale precipitation (Hynek et al., 2009; Di Achille and Hynek, 2010) during this period. Formation timescale estimates for the valley networks typically range between 10^5-10^8 years (Craddock and Howard, 2002; Hoke and Hynek, 2011), with corresponding annual precipitation rates between 10-100 cm per terrestrial year.

A problem with the requirement for precipitation at these latitudes is that under low to moderate obliquities (<40°), water is most stable at the poles, so that any precipitation that reached the surface would quickly sublimate back into the atmosphere and return to the cold pole (Toon et al., 1980; Jakosky et al., 1995; Mellon and Jakosky,

1995). However a solution to this problem is that the Martian obliquity may have been higher in the past. The Martian obliquity has been shown to be chaotic, and could have been as high as 60° in the past (Ward et al., 1979; Laskar and Robutel, 1993; Touma and Wisdom, 1993; Laskar et al., 2004). During such periods of high obliquity (>40°), climate models have shown that ice becomes stable at the surface at non-polar latitudes, and could accumulate to potentially melt at a later time when the tropics become warm (Toon et al., 1980; Jakosky and Carr, 1985; Jakosky et al., 1995; Richardson and Wilson, 2002; Mischna et al., 2003; Haberle et al., 2003). Observations of the ice table depth also suggest the migration of water from the poles to lower latitudes (e.g. Head et al., 2003; Holt et al., 2008).

An alternate hypothesis to explain the presence of fluvial erosion features at tropical and sub-tropical latitudes is the existence of large bodies of water near the observed features to provide localized sources of water for precipitation. These have been proposed to be lakes (McKay and Davis, 1991; Kite et al., 2011), or possibly an ocean in the northern hemisphere (Di Achille and Hynek, 2010). The possibility of oceans on Mars has been a topic of discussion since the observations of the large deltas, outflow channels, and other fluvial features (Parker et al., 1989; Baker et al., 1991; Parker et al., 1993). Subsequent spacecraft observations by the Mars Orbiter Laser Altimeter (MOLA; Head et al., 1999; Di Achille and Hynek, 2010), and the Gamma Ray Spectrometer (GRS; Dohm et al., 2010) have provided further evidence for an ancient ocean (Clifford and Parker, 2001; Carr and Head, 2003; Fairen et al., 2011). Parker et al. (1989, 1993), and Clifford and Parker (2001) have suggested multiple possible shorelines for the ocean based on observations of boundaries between geologic units. Two of the identified

shorelines that suggest northern hemispheric oceans are the Deuteronilus shoreline, with a mean elevation of -3792 m, and the Arabia shoreline, with a mean elevation of -2090 m (Carr and Head, 2003). Head et al. (1999) preferred the Deuteronilus shoreline to the Arabia shoreline, because the features associated with the Arabia shoreline showed kilometers of variation in elevation, while the Deuteronilus shoreline had a much smaller range of hundreds of meters. However, recent analyses of the delta deposits linked to the valley networks show remarkable consistency with the Arabia shoreline when considering only deltas that are not contained in closed basins (Di Achille and Hynek, 2010). This revised shoreline, with a mean elevation of -2540 m, had a standard deviation of 177 m, which is within the expected range of variation on a global scale.

In this work, we use a Mars general circulation model (Urata and Toon, 2012a,b) to examine precipitation rates and patterns under various conditions with a thick CO_2 atmosphere, and a reduced solar constant. The varied conditions include the planet's obliquity, and the presence of oceans within the Arabia shoreline, Hellas basin, and Argyre basin.

4.2 Model description and Initial Conditions

We use the general circulation model for Mars described in Urata and Toon (2012a). This model was adapted to Mars from the terrestrial Community Atmosphere Model (CAM) of the National Center for Atmospheric Research (NCAR; Collins et al., 2004). The modifications made for Mars include changing planetary parameters such as gravity, atmospheric composition, topography, albedo, thermal inertia, etc.; as well as

orbital parameters such as eccentricity, obliquity, and longitude of perihelion. Radiative transfer calculations are performed with a two-stream correlated-k model (Toon et al., 1989), with water vapor and carbon dioxide assumed to be the only absorbing gases. Absorption and scattering by dust and water clouds are also considered, assuming Mie scattering. The radiative effects of carbon dioxide clouds are not included at this time, however the thermal effects are included by assuming that the atmospheric temperature does not fall below the CO_2 condensation temperature, which affects the lapse rate near the model top as the mesosphere is approached.

For model runs that include an ocean, we use the Slab Ocean Model (SOM) of CAM. The SOM couples an ocean model including a thermodynamic sea ice component to the atmosphere through the ocean mixed layer temperature. The ocean mixed layer temperature (T_o) is calculated as

$$\rho_o c_o h_o(\partial T_o/\partial t) = (1\text{-}A)F + Q + AF_{oi} + (1\text{-}A)F_{frz} \quad (4.1)$$

where ρ_o is the ocean water density, c_o is the ocean water heat capacity, h_o is the annual mean mixed layer depth, A is the fraction of ocean covered by sea ice, F is the net atmosphere to ocean heat flux, Q is the internal ocean mixed layer heat flux which parameterizes seasonal deep water exchange and horizontal oceanic heat transport, F_{oi} is the heat exchanged between the sea ice and ocean through basal melting, side melting, and transmitted solar radiation, and F_{frz} is the latent heat gained from sea ice growth. As the values for a Martian ocean are not known, we assume terrestrial ocean values for density (ρ_o = 1026 kg m^{-3}), heat capacity (c_o = 3930 J kg^{-1} K^{-1}), and mean layer depth (h_o=10-200 m depending on season and latitude), and set the internal ocean mixed layer heat flux (Q) to zero. The mean layer depth values were determined from terrestrial

observations, using the dataset's standard measure of salinity $\sigma_t = (\rho_s - 1) \bullet 10^3$ (Levitus, 1982), where ρ_s is the density of water for a specified salinity, and determining where the equality $\sigma_t(h_0) - \sigma_t(surface) = 0.125$ was satisfied. On Earth, this leads to shallow tropical layers (10-30 m), and large seasonal variations at high latitude (10-200 m), where the oceanic salinity will change due to the freezing and melting of the caps. On Mars, using these values would cause the high latitude oceanic response times to slow down during the summer even if the ice cap is not melting. However, the simulations discussed below will show that even at low latitude (where the layer depths are assumed to be shallow) and high incident solar flux, the oceans will form thick layers of ice at the surface, suggesting that the mixed layer depths will not have a large impact on the final outcome. The ocean water salinity is not directly specified, but is implied by the ice salinity, which is assumed to be zero at the ice surface, and increases to the terrestrial value 3.2 ‰ at the bottom (approximately 10% of the ocean salinity). Higher values of salinity would lower the freezing temperature of the ocean, resulting in liquid oceans down to colder temperatures. Since the liquid ocean has a much lower albedo than the sea ice, there could be a salinity for which a liquid ocean is stable.

The thermodynamic sea ice model is a 4-layer model that calculates heat transfer through the sea ice after sea ice has formed. In addition to heat transfer, this also includes precipitated snow accumulation, melt, and conversion to sea ice. New sea ice is assumed to form when the surface temperature falls below freezing after being updated, and contributes to F_{frz}.

To simulate the ancient climate, the model was initialized with a 500 mb CO_2 atmosphere and a reduced solar constant of 75% the present day value. Each simulation

was run for 4 Mars years, and results are taken from the last model year. The ocean simulations assume oceans below -2540 m including the Arabia shoreline, Hellas basin, and Argyre basin, and begin with 1000 pr-μm of atmospheric water vapor. Since we were interested in the precipitation rates and pattern in a warm climate, we have assumed the conditions discussed in Chapter 3 that led to warm, stable climates. Namely, 10 μm cloud particles, full grid cloud coverage where clouds are present, and a low auto-conversion efficiency of cloud mass to precipitation, which significantly increased the atmospheric water lifetime. Although whether or not these assumptions are realistic has yet to be fully examined, they provide a self-consistent climate for modeling precipitation. The parameters for the various simulations are summarized in Table 4.1.

Case Name	**Pressure (mb CO_2)**	**Initial Water (pr-μm)**	**Ocean**	**Obliquity**
1	500	1000	No	0°
2	500	1000	No	25°
3	500	1000	No	45°
4	500	5.4e5	No	0°
5	500	5.4e5	No	25°
6	500	5.4e5	No	45°
7	500	5.4e5	No	65°
8	500	1000	Yes	0°
9	500	1000	Yes	25°
10	500	1000	Yes	45°
11	500	1000	Yes	65°
12	1000	1000	Yes	0°
13	1000	1000	Yes	25°
14	1000	1000	Yes	45°
15	1000	1000	Yes	65°

Table 4.1. Simulation parameters.

4.3 Simulation Results

4.3.1 No Oceans

With no oceans, the only sources of water are the initial atmospheric water content, and the prescribed polar ice cap in the north. In order to determine if the conditions are suitable for river valley formation, two things must hold true. First, the surface temperatures must be above the freezing point of water for an extended period of time, and precipitation must fall in or near the areas where the river valleys are observed. Figure 4.1 shows the mean annual surface temperature for case 2 of Table 4.1.

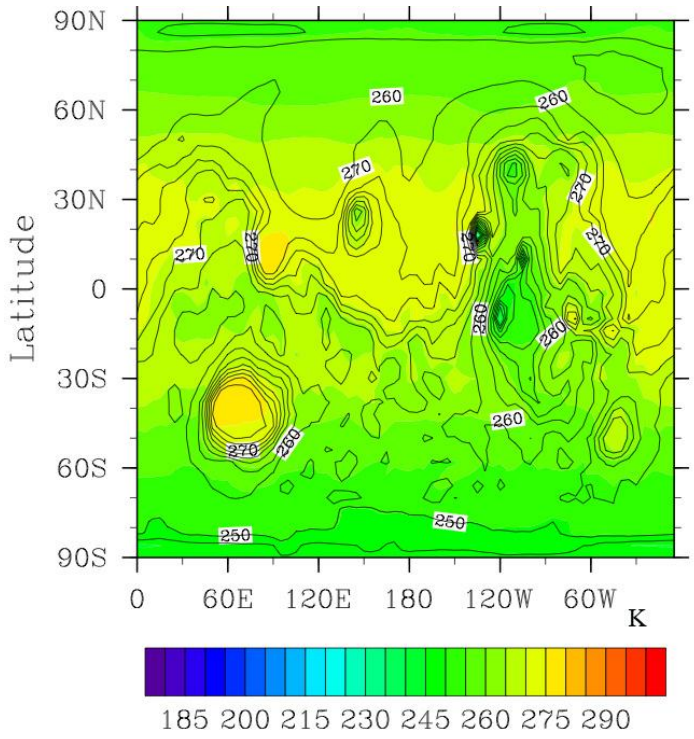

Figure 4.1. The mean annual surface temperature for case 2 of Table 4.1, overlain on the Martian topography.

As is apparent in Fig. 4.1, the mean annual surface temperature can reach near or above freezing near the equator, and in Hellas basin. However, the mean annual surface

temperature across much of the valley forming areas is 10-15 degrees below freezing. This is not necessarily an issue of concern, as the mean annual temperatures of the Antarctic Dry Valleys are approximately 20 degrees below freezing, but form seasonal streams during the summer. Therefore, a shorter timescale is more appropriate for determining if the temperatures are conducive to river valley formation. Figure 4.2 shows the maximum mean 10-day surface temperature over the year, which is more indicative of the summer temperatures.

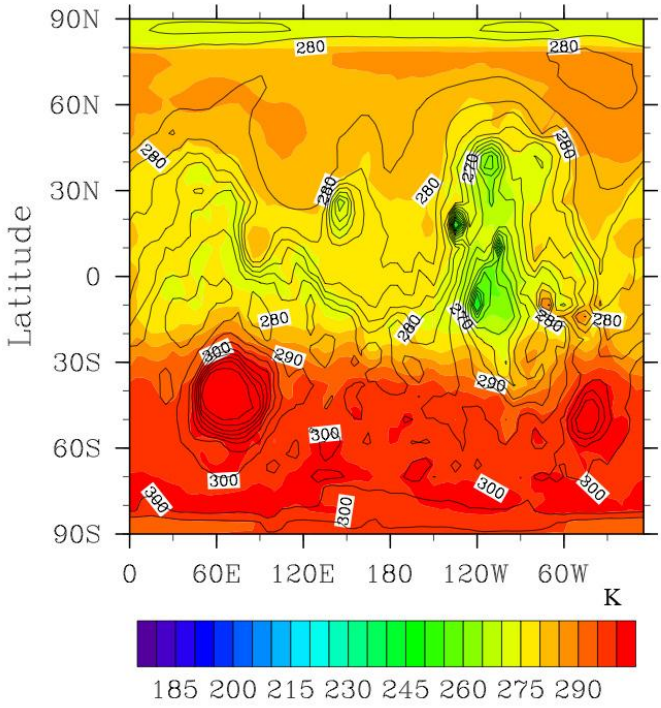

Figure 4.2. The maximum mean 10-day surface temperature for case 2 of Table 4.1.

The mean 10-day surface temperatures show that seasonally, most of the planet will rise above the freezing temperature of water. The hemispheric asymmetry is due to the eccentricity of the orbit, causing the southern summer to be warmer than northern

summer. These temperatures suggest that if precipitation reaches the surface and can remain stable there for up to a year, it should melt during the summer, and possibly contribute to river valley formation. Figure 4.3 shows the annual precipitation (cm), summed over a Mars year, for case 2.

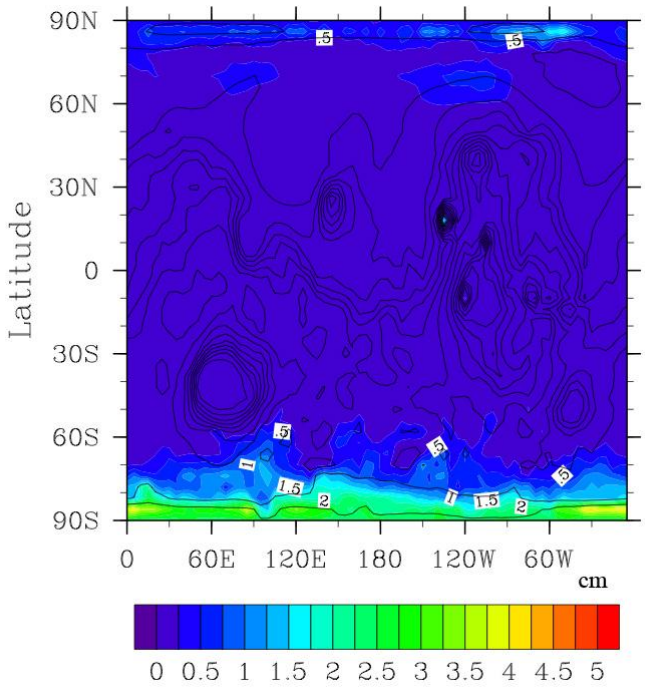

Figure 4.3. Annual precipitation (cm) for case 2 of Table 4.1.

In this simulation, there little annual precipitation in the river valley areas (less than 0.25 cm), and most of the precipitation is located at the poles, where the water is stable. This precipitation distribution is to be expected in a dry climate with relatively low obliquity, as much of the precipitation will evaporate back into the atmosphere in the tropics before reaching the ground because the relative humidity is low. At higher obliquities, the summer temperature in the tropics decreases, allowing precipitation to reach the ground

and accumulate. The seasonal maximum temperatures and precipitation patterns for case 3 with an obliquity of 45° are shown in Figs. 4.4a and 4.4b.

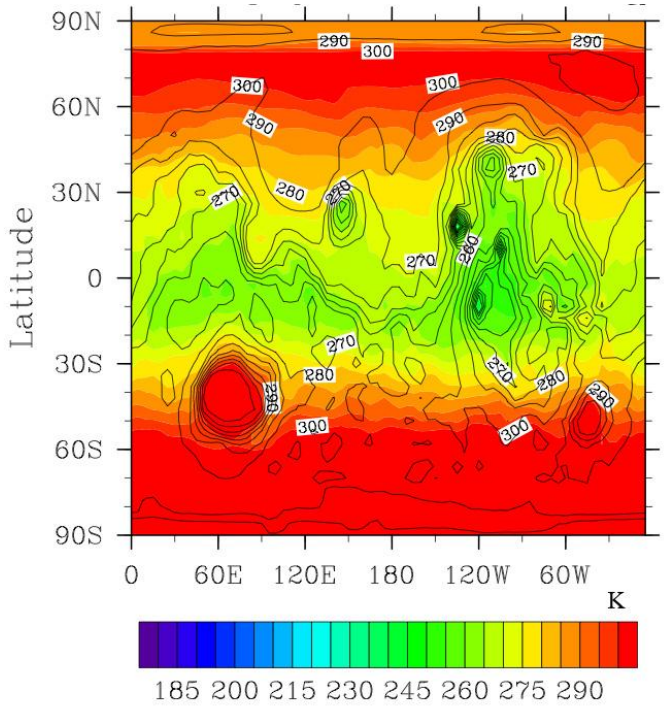

Figure 4.4a. Maximum mean 10-day surface temperature for case 3.

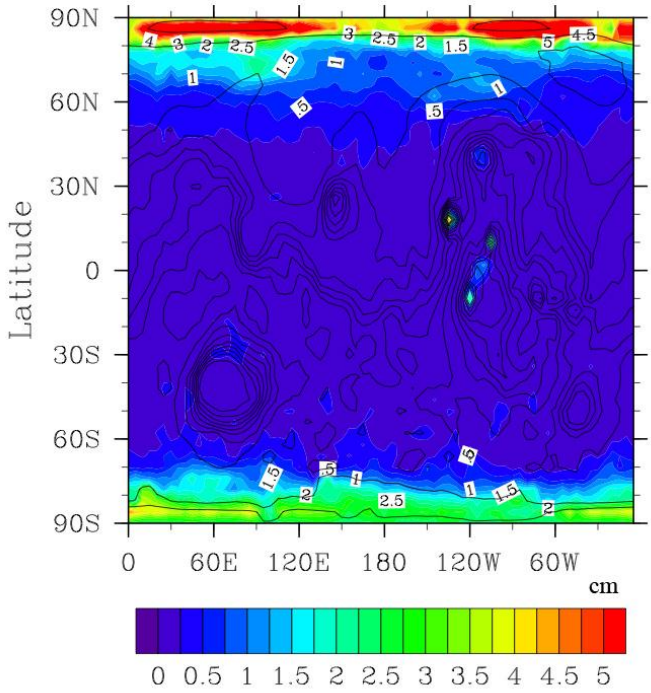

Figure 4.4b. Annual precipitation rates (cm) for case 3.

At a higher obliquity, the seasonal high temperatures in the tropics fell by 10-15 K relative to low obliquity, while rising by approximately the same amount at high latitudes. This temperature shift is accompanied by an increase in overall precipitation due to higher polar temperatures during the summer that increase the amount of water released from the caps. However, the precipitation that reaches the surface in the tropics is still small due to the inherently dry climate that promotes the rapid evaporation and sublimation of water.

Precipitation in the tropics is limited if the only source of water is the polar caps. An enhanced tropical water source can be achieved either by having snow or ice at or near the surface, or by having large bodies of water, such as oceans, to act as sources. Cases 4-7 are simulations with snow coverage and no ocean, and cases 8-15 are

simulations that contain oceans. A summary of the total precipitation in a Mars year for each simulation is presented in Table 4.2.

Case	Global GEL Precip (cm/yr)	Valley GEL Precip (cm/yr)	Global Total Precip (kg/yr)	Valley Total Precip (kg/yr) (30N-60S)	Valley Total Precip (kg/yr) (land only)	Valley (30N-60S) / Global Precip Ratio	Valley (land only) / Global Precip Ratio	Valley Total Rain (cm/yr)	Valley GEL Runoff (cm/yr)
1	3.60E-03	0.00	5.21E+12	0.00	---	0%	---	0	2.11E-06
2	7.12E-02	9.98E-03	1.03E+14	1.44E+13	---	14%	---	7.68E-04	6.56E-05
3	0.210	3.74E-02	3.03E+14	5.41E+13	---	18%	---	3.83E-03	2.02E-04
4	0.544	0.243	7.87E+14	3.51E+14	---	45%	---	9.95E-03	3.08E-02
5	0.398	0.169	5.77E+14	2.45E+14	---	42%	---	7.65E-03	9.47E-03
6	1.35	1.10	1.96E+15	1.59E+15	---	81%	---	3.67E-02	4.01E-03
7	1.36	0.897	1.97E+15	1.30E+15	---	66%	---	3.14E-02	2.17E-03
8	1.27	0.614	1.85E+15	9.04E+14	8.90E+14	49%	48%	4.36E-02	1.67E-02
9	1.56	1.02	2.26E+15	1.55E+15	1.48E+15	68%	66%	6.04E-02	3.70E-02
10	1.48	0.896	2.14E+15	1.40E+15	1.30E+15	66%	61%	6.04E-02	2.32E-03
11	1.62	0.671	2.34E+15	1.05E+15	9.72E+14	45%	41%	4.90E-02	7.05E-04
12	1.70	1.09	2.46E+15	1.62E+15	1.58E+15	66%	64%	1.67E-01	1.68E-01
13	1.64	1.24	2.37E+15	1.81E+15	1.79E+15	77%	76%	1.23E-01	7.78E-02
14	1.89	1.28	2.74E+15	2.06E+15	1.85E+15	75%	68%	1.51E-01	8.76E-02
15	2.39	0.966	3.45E+15	1.47E+15	1.40E+15	42%	40%	1.32E-01	1.83E-02

Table 4.2. Global and Valley region annual total precipitation, rain, and runoff rates given as Global Equivalent Layers of water (GEL) in cm per Mars year, and total precipitation mass per Mars year.

The precipitation rates for each case are given in Table 4.2 as global equivalent layers of water (GEL; cm yr^{-1}) and as total mass (kg yr^{-1}) for the global annual precipitation, and over the latitudes where the river valleys are observed (30°N - 60°S). The global equivalent layers were calculated using the following method. First the mean annual precipitation rates for each grid cell (kg m^{-2} s^{-1}) were multiplied by the area of each cell (m^2) and length of a Martian year (s yr^{-1}), and then summed over the planet to find the global rates (kg yr^{-1}). These were then converted to global equivalent layers (cm yr^{-1}) by dividing by the density of water (1000 kg m^{-3}) and the Mars global surface area ($1.448x10^{14}$ m^2), with a unit conversion from meters to centimeters. In the cases of the river valley rates, the precipitation rates were only summed over the specified latitudes (30°N - 60°S) and then converted to global equivalent layers. For the simulations containing oceans, the precipitation that occurs over land only is also included. The next columns contain the ratio of precipitation that occurs in the river valley latitudes to the global precipitation, with a separate column for precipitation over land only. The table also includes the annual rain rates (most precipitation falls as snow, not rain) and runoff rates in the river valley latitudes. Note that while the rain rates and runoff rates are low, they are not distributed uniformly over the valley network area. Local rainfall rates can reach cm/yr as discussed below. Runoff is lower than rainfall and precipitation because most of the liquid seeps into the ground. Runoff requires that liquid is present on ground that is saturated. The soil model parameterizes the grid cell averaged runoff as a weighted mean between the fraction of saturated soil and unsaturated soil based off of the average soil water content (Oleson et al., 2004). Possibly running the model for much longer time

periods may have led to the soil being saturated over a wide region, and subsequently more runoff.

Cases 4-7 were initialized with 50 cm of precipitable water in the atmosphere, which quickly snowed out to create an extensive layer of snow on the surface. This subsequently acted as a local reservoir of water, humidifying the atmosphere, and allowed a significant increase in the precipitation in the tropics. In fact, up to 81% of the precipitation occurs between 30°N - 60°S depending on obliquity. The maximum mean 10-day temperatures and annual precipitation rates for obliquity=25° (case 5), and 45° (case 6) are shown in Figs. 4.5 and 4.6.

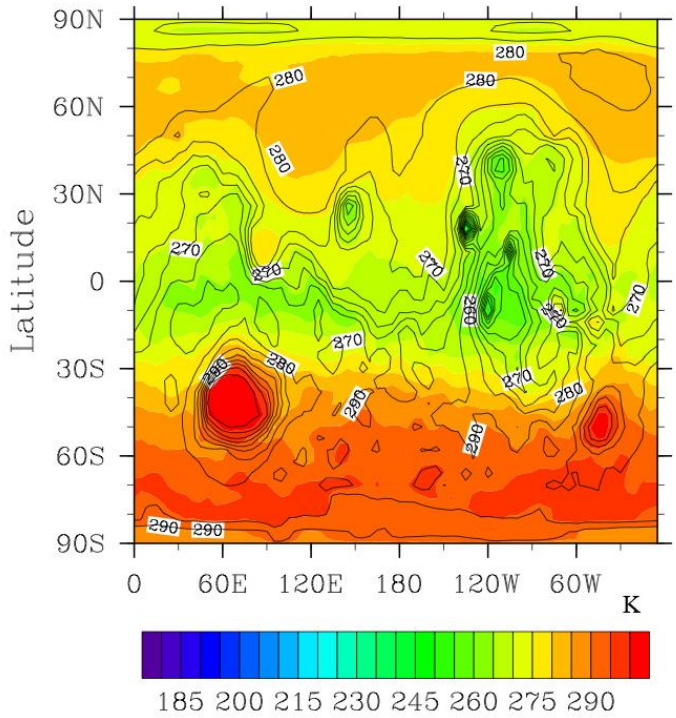

Figure 4.5a. Maximum mean 10-day surface temperature for case 5.

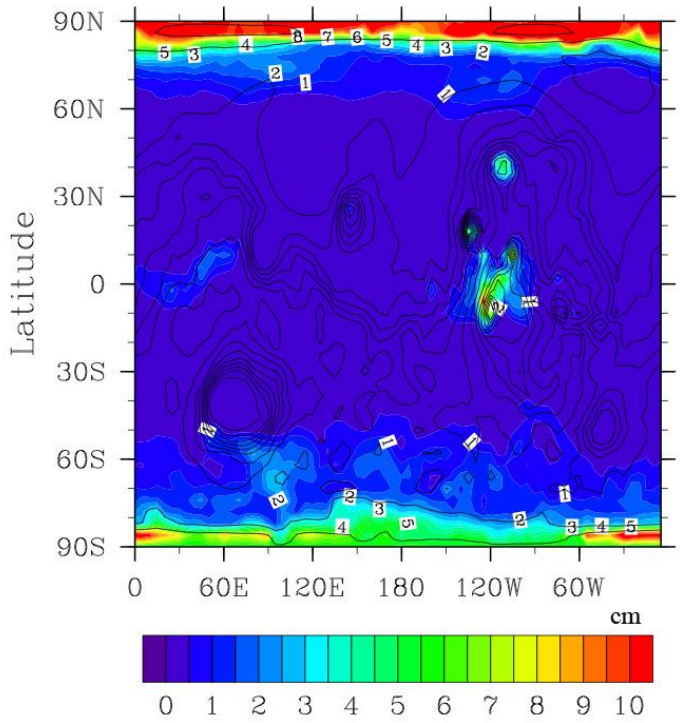

Figure 4.5b. Annual precipitation for case 5.

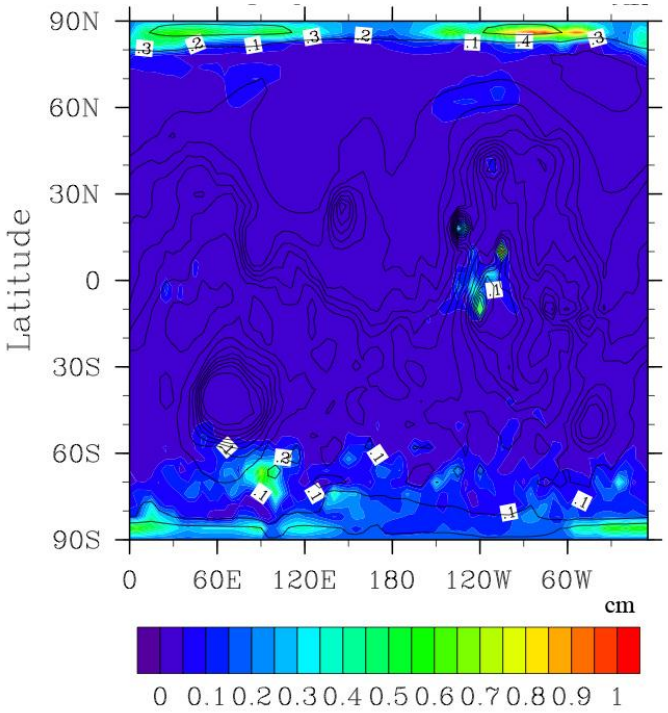

Figure 4.5c. Annual rain for case 5.

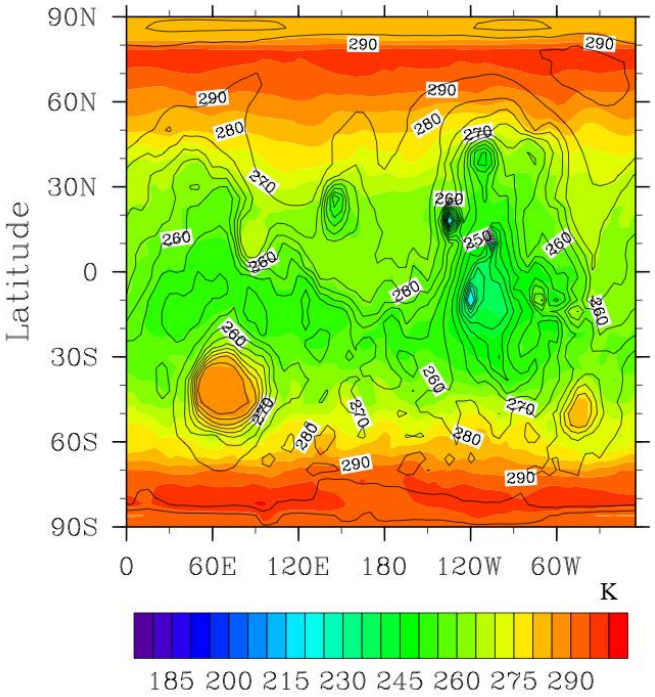

Figure 4.6a. Maximum mean 10-day surface temperature for case 6.

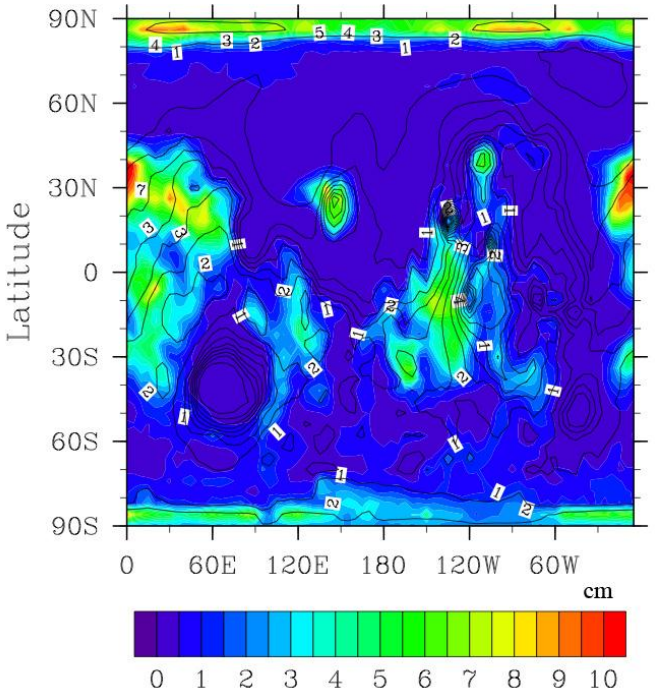

Figure 4.6b. Annual precipitation for case 6.

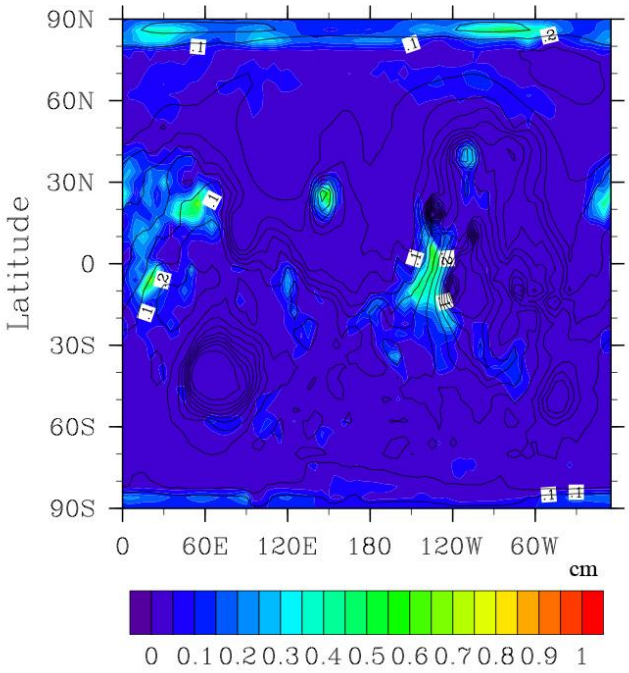

Figure 4.6c. Annual rain for case 6.

Comparing Fig. 4.5b to 4.6b, the increase of precipitation in the tropics corresponding to the increase in obliquity is immediately clear. However, although the precipitation in the tropics is increased at high obliquity, the seasonal high temperatures have decreased, suggesting that precipitation that reaches the ground would accumulate during such high obliquity periods, and may not melt on an annual basis to form streams. Figures 4.5c and 4.6c show that the annual rain rates (the total precipitation is snow + rain) are 1-5% of the total precipitation. The tropical temperatures, at roughly 260 K, are fairly close to the melting temperature of water though, so it is possible that greenhouse contributions from sources other than CO_2, water vapor, and water clouds may warm the planet enough to form seasonal streams.

4.3.2 Oceans

Similar to cases 4-7 in which there are snowfields in the river valley area, the presence of large bodies of water puts water near the regions of river valley formation where it is normally not stable against sublimation or evaporation. The oceans tend to completely freeze over within the first year or so, raising the albedo, and resulting in cooler atmospheric temperatures. The annually averaged sea ice thickness after the fourth year for case 10 is shown in Fig. 4.7. Even after this relatively short time, the northern ocean is covered by meters of ice, and the southern seas are freezing as well. However, despite the oceans being covered in ice, they can still act as sources of water for precipitation, as will be shown in this section.

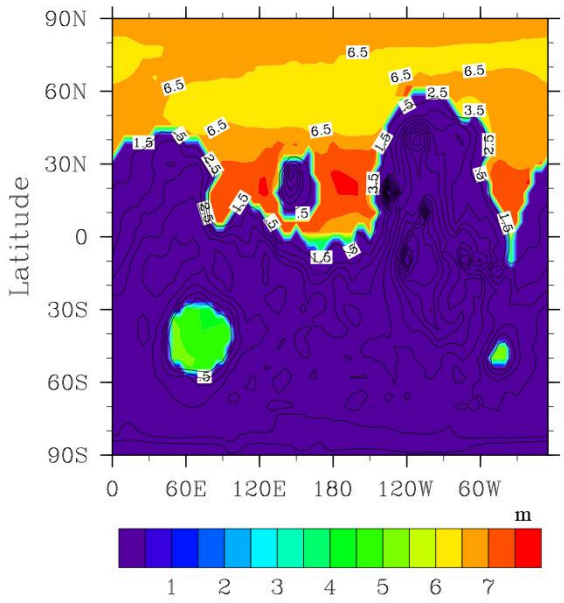

Figure 4.7. Annual average sea ice thickness for case 10 of Table 4.1.

We have not fully explored the evolution of the oceans in these simulations. We imagine that one result of planet-wide mobilization of water by a large impact would be the creation of temporary seas, lakes and oceans. These results show that even with a

relatively warm planet the oceans soon freeze over. After four Mars years, the ice is 3-5 meters thick and continuing to thicken. Possibly they will freeze completely and form glaciers. Or possibly the bodies of water will remain liquid in some regime of salinity. However, as with the snow fields discussed earlier, the presence of large bodies of exposed ice at low latitudes will lead to a large supply of water vapor as the ice slowly migrates back to the polar latitudes.

The higher humidities in the presence of tropical ice let clouds form closer to the surface, and precipitation reach the ground before evaporating or sublimating back into the atmosphere, as in shown in Fig. 4.8. The figure shows a comparison of the zonally averaged cloud mass (g m^{-3}) at L_s=120° for cases 3, 6, and 10. We also performed simulations with 1 bar of CO_2 to see if the increased amount of CO_2 would provide enough warming to significantly change the results, but found that aside from slightly increased surface temperatures and precipitation rates, the general results were mostly unchanged compared to the 500 mb cases. Therefore we will focus on the 500 mb simulations in order for easier comparison to the non-ocean cases.

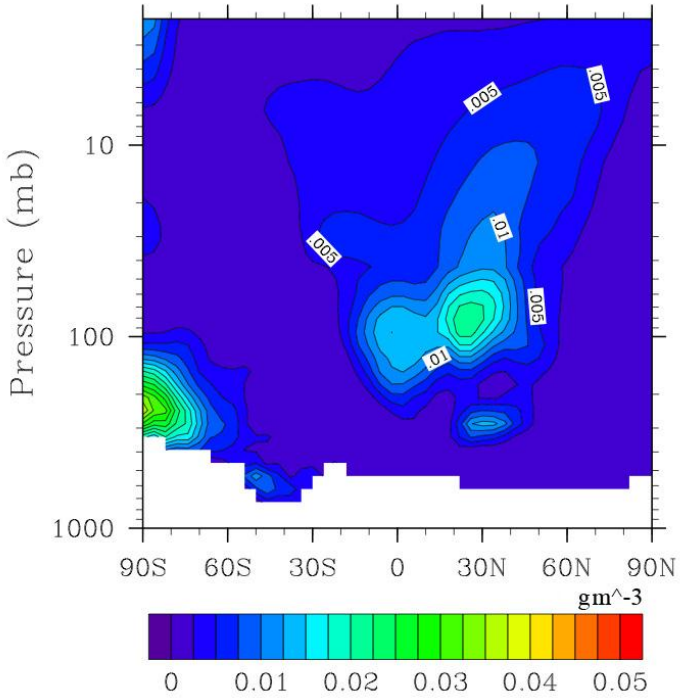

Figure 4.8a. Zonal average cloud mass (g m^{-3}) at L_s=120° for case 3.

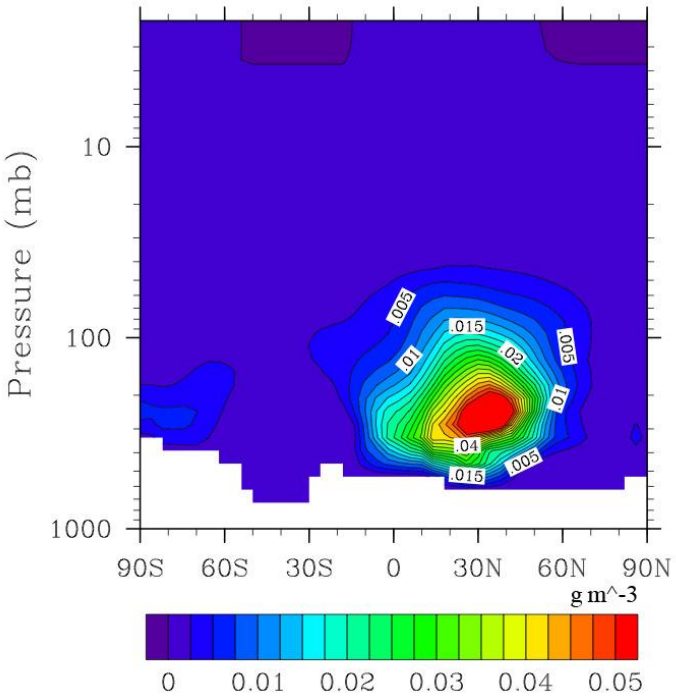

Figure 4.8b. Zonal average cloud mass (g m^{-3}) at L_s=120° for case 6.

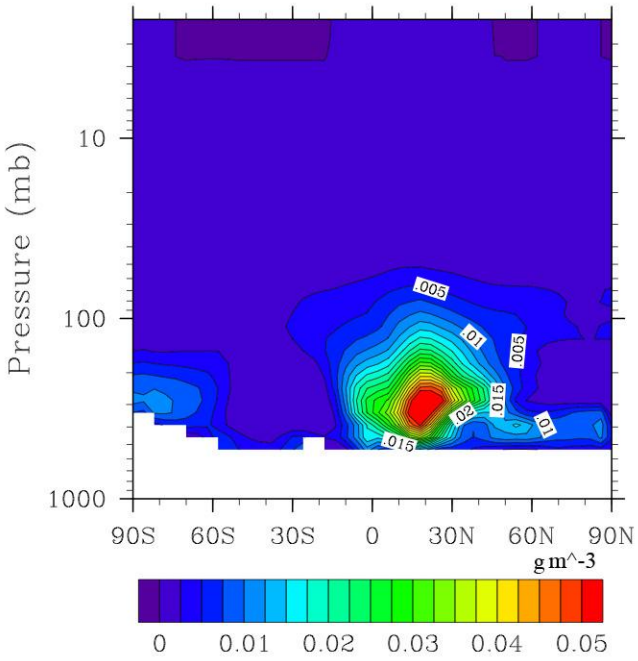

Figure 4.8c. Zonal average cloud mass (g m^{-3}) at L_s=120° for case 10.

Each of the cases in Fig. 4.8 assume obliquity=45°, with the most precipitation in the tropics in the simulations corresponding to Figs. 4.8b, and 4.8c. The latter two (cases 6 and 10) both have water sources at the surface in the form of snow (Fig. 4.8b), or oceans covered in ice (Fig. 4.8c). The plots show maximum cloud mass between 200-300 mb, approximately an altitude of 5-10 km, as opposed to 15-20 km for Fig. 4.8a. The precipitation that falls from these lower altitude clouds results in the increased tropical precipitation seen in Fig. 4.6b, and Fig. 4.9b. Figure 4.9c is the annual rain rate, which shows that the rain is 1-5% of the total precipitation, similar to the no ocean cases.

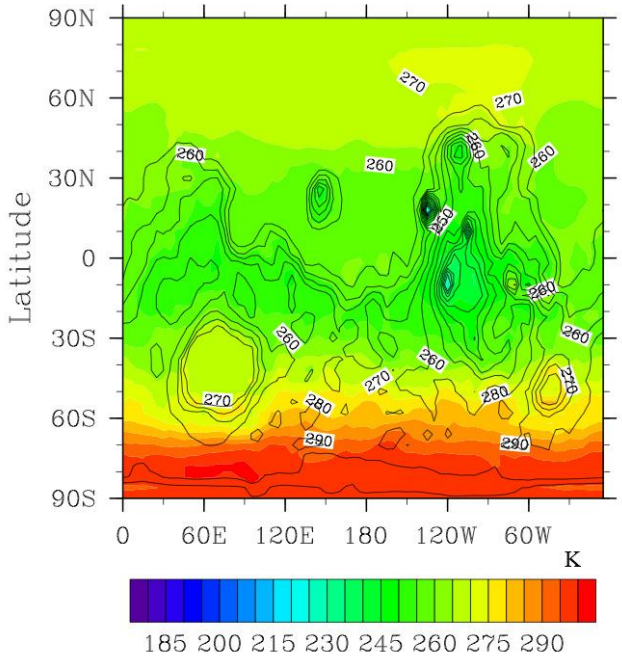

Figure 4.9a. Maximum mean 10-day surface temperature for case 10.

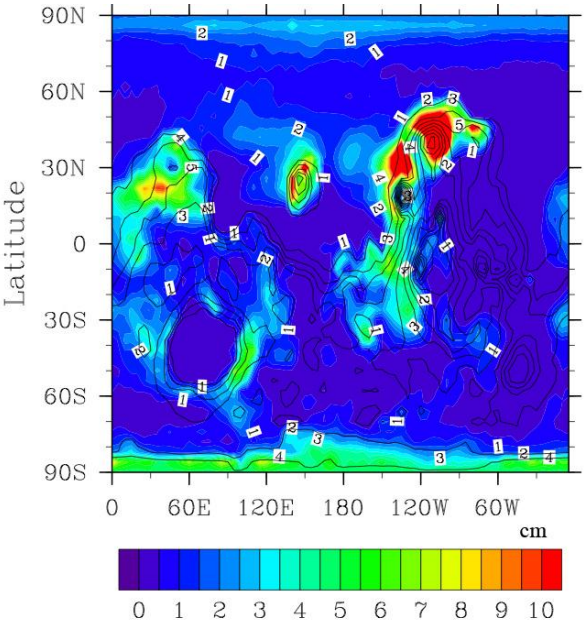

Figure 4.9b. Annual precipitation for case 10.

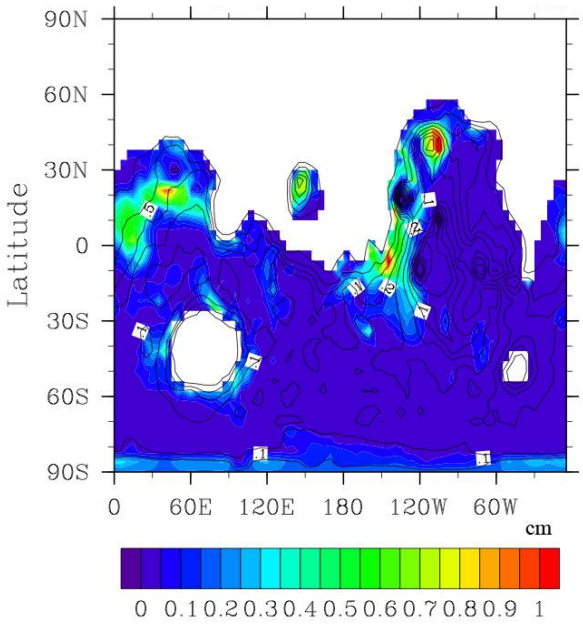

Figure 4.9c. Annual rain for case 10.

An interesting result of including oceans is that precipitation rates of 10 cm per Mars year occur with an ice covered ocean even at the relatively low obliquities of 0° and 25° (Table 4.2, Fig. 4.10).

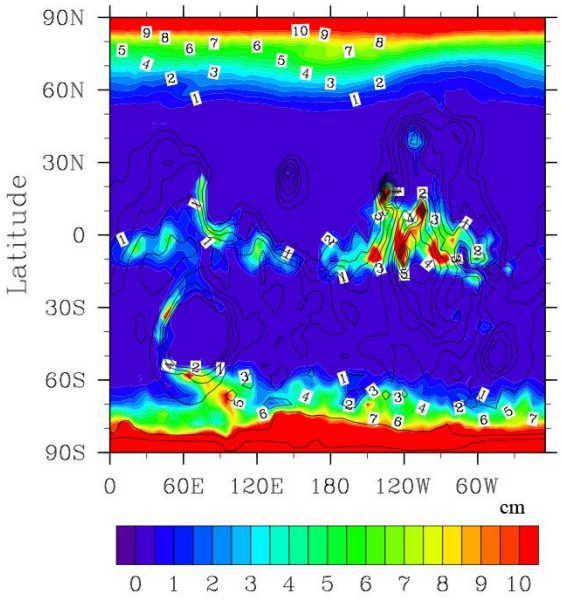

Figure 4.10a. Annual precipitation for case 8 of Table 4.1.

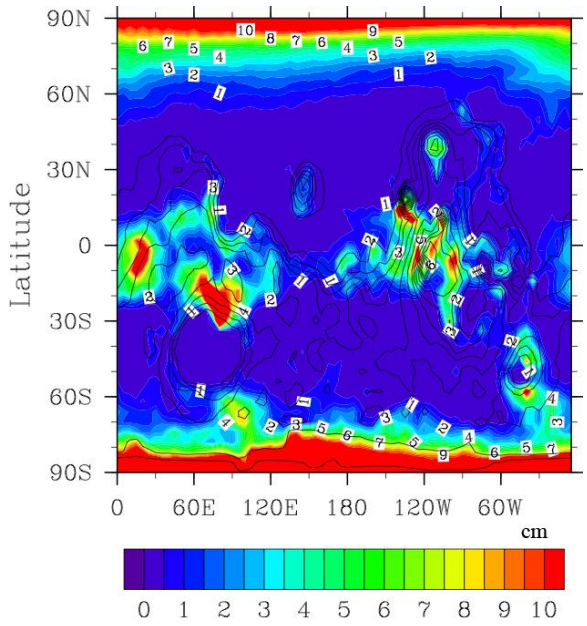

Figure 4.10b. Annual precipitation for case 9 of Table 4.1.

In both cases, most of the non-polar precipitation is found near the shorelines, mainly in the western half of Tharsis, north of Hellas, and around Argyre. The annual precipitation for some areas can be greater than 10 cm even in these low obliquity states. In addition to there being noticeable precipitation during low obliquity states, the latitudes for high precipitation tend to change with obliquity as well. At higher obliquities (Fig. 4.9b), precipitation is seen near the northern edge of Tharsis, around Arabia Terra, and along the eastern and western shores of Hellas. The large tropical precipitation for cases with sea ice covered oceans (Fig. 4.10) is in contrast to the non-ocean cases (Figs. 4.3-4.6), where precipitation is widespread at high obliquity but well below 1 cm per Mars year.

If ice covered oceans and large bodies of water were the source of low latitude water, one might expect to see correlations between fluvial activity and latitude on the timescales of obliquity change. Unfortunately, current dating methods are not accurate enough to find precise ages of all the observed features, and since the formation

timescales for the river valleys can be larger than the obliquity cycle (~10^5 years), it may not be possible to differentiate between active and dormant periods of fluvial activity without much more detailed (or in situ) observations of the features.

4.4 Discussion

We used a general circulation model for Mars to study a hypothetical ancient climate with a thicker atmosphere and reduced solar constant. Assuming the conditions required for a warm climate found in Urata and Toon (2012b), simulations were done to look at global precipitation patterns and rates. We performed tests to see the effects of obliquity changes, and the possible presence of oceans in the northern hemisphere, Hellas basin, and Argyre basin. Urata and Toon (2012b) found that an initially wet atmosphere (1000 pr-μm) could lead to stably warm climates. However, such warm climates with only the north polar cap as a water source, have very low precipitation at low latitudes where most of the fluvial features associated with surface runoff during the late Noachian are observed, even at very high obliquity.

A local source of water is required for significant precipitation (a few cm/yr) to occur at river valley latitudes. The source could be in the form of a low-latitude layer of snow or an ocean, either of which may develop after a large impact. In the case of a layer of snow on the surface (Fig. 4.11), significant tropical precipitation only happened at high obliquity (>45°), because the tropical temperatures (and relative humidity) were not conducive to low cloud formation at low obliquities.

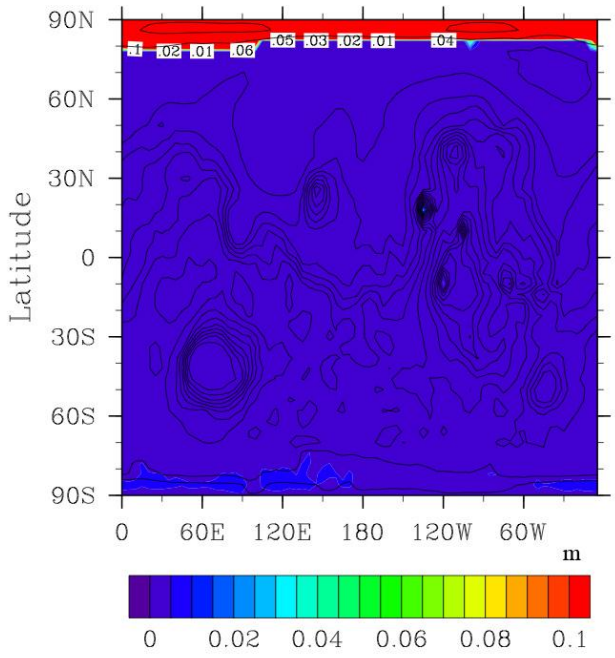

Figure 4.11a. Snow depth (m) for case 2.

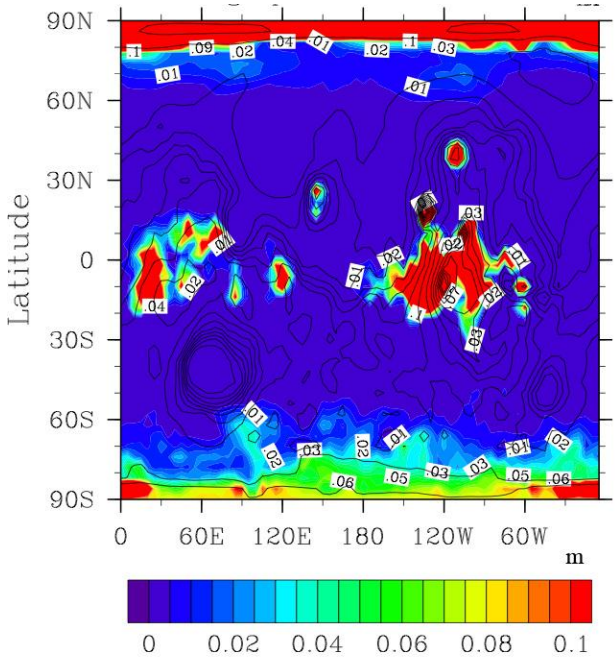

Figure 4.11b. Snow depth (m) for case 5.

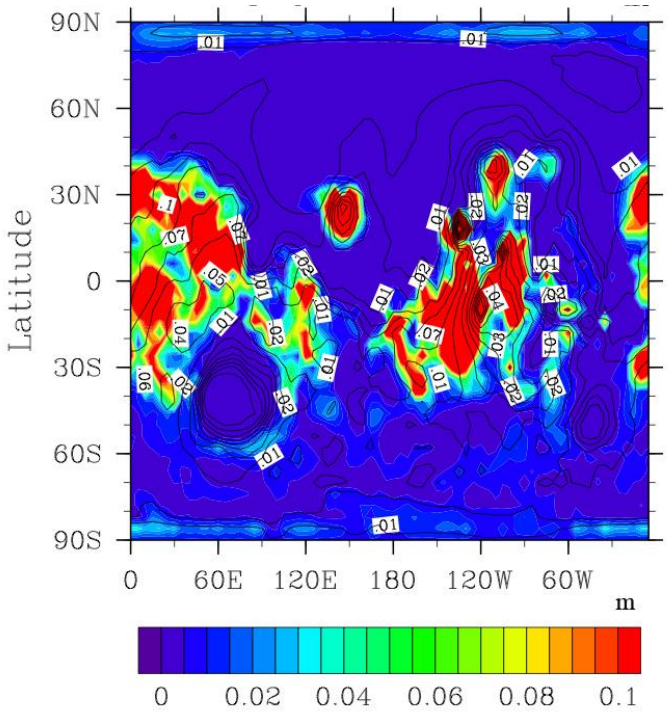

Figure 4.11c. Snow depth (m) for case 6.

Figures 4.11a and 4.11b show the snow depth for cases 2 and 5 of Table 4.1. There is little tropical precipitation in both cases, but there is a significant amount of low-latitude snow, as well as south polar snow in the wetter case 5. Figure 4.11c is the snow depth for case 6 (obliquity = 45°), and shows that at high obliquity the snow covers much more of the planet compared to the low obliquity cases.

However, when ice covered oceans are included, significant precipitation is observed across all obliquities. This is true even when ice sheets that are meters thick cover the oceans. The reason is that the oceans provide a steady source of water spanning a large range of latitudes, keeping the lower atmosphere relatively moist via sublimation. Subsequently, the altitude of cloud formation is lowered, leading to increased precipitation reaching the surface in the tropics.

Although the 10-day mean surface temperatures are lower than the melting temperature of water, suggesting that seasonal streams are not probable, the daytime temperatures do exceed melting, creating some runoff. On present day Mars, the daytime temperatures can also reach above the melting temperature of water, but the pressures are low, so that liquid water is not stable. The amount of runoff in the tropics is typically small, at 10^{-3} cm/yr, up to a few cm/yr at most (Fig. 4.12). This runoff is not enough to account for the river valleys by itself, but it will contribute to their formation. Runoff is lower than rainfall and precipitation because most of the liquid seeps into the ground. Runoff requires that liquid is present on ground that is saturated. Possibly running the model for much longer time periods may have led to the soil being saturated over a wide region, and subsequently more runoff.

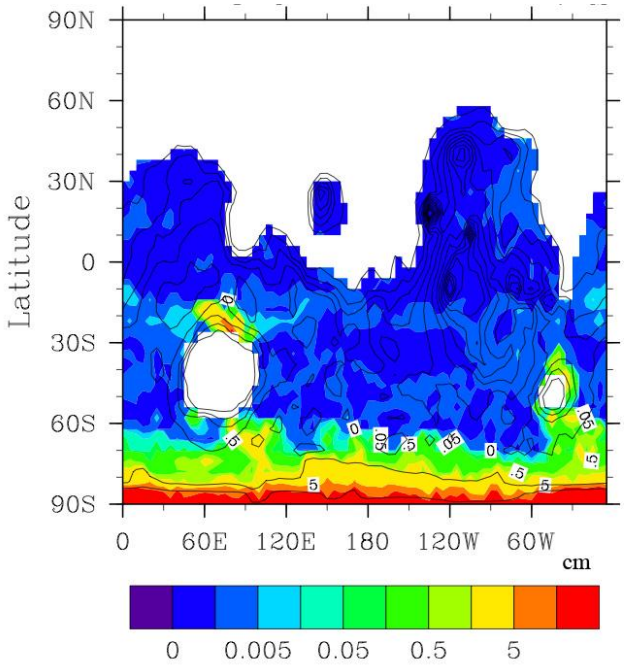

Figure 4.12a. Annual runoff for case 9 on a logarithmic scale.

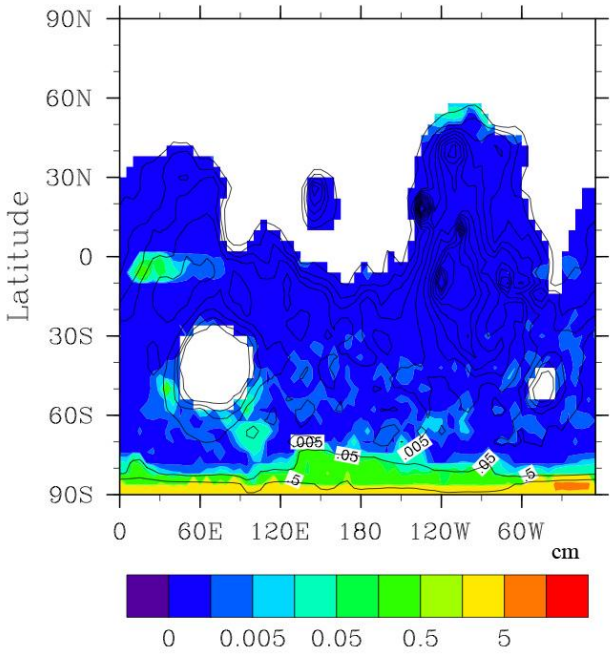

Figure 4.12b. Annual runoff for case 10 on a logarithmic scale.

These modeling results may tend to support the presence of oceans if the view of continuous valley formation is adopted. An alternate source of water that has been discussed is groundwater, which can be released when the water table depth changes with obliquity (Andrews-Hanna and Lewis, 2011). Similarly to oceans, near-surface ground water could provide local sources of water for precipitation. The obliquity cycle appears to play a key role in the formation of the widespread river valley networks, especially if they are assumed to be the result of precipitation. The latitudes at which precipitation tends to fall vary greatly with the obliquity, and a large range of obliquities is required to have precipitation at all of the latitudes where the river valleys are observed. These results depend heavily on the greenhouse effect of clouds, as discussed by Urata and Toon (2012b). More detailed microphysical models will be needed in the future to more

fully determine the precipitation rates and patterns and their relationship to the Martian geological record.

Chapter 5. Conclusions

In this work, we presented a new general circulation model (GCM) for Mars, adapted from the Community Atmosphere Model, a terrestrial model from the National Center for Atmospheric Research (NCAR). In chapter two, we compared model results to spacecraft observations, showing that the model could reproduce observations well, and proving that it can be a useful tool for simulating the Martian climate. We compared the zonally averaged atmospheric temperatures to observations at two different seasons, and found that the model temperatures were generally within +/- 5 K, except for some small regions, where the model diverged by up to 15 K. These areas were later shown in chapter three to be greatly affected by the radiative effects of water ice clouds, where the large divergences mostly disappeared when these effects were included. Comparisons to the surface, and near-surface temperatures showed that the surface model performed well with Martian surface albedos and thermal inertias; and comparisons of the predicted boundary layer heights to observations showed that the parameterization of the near-surface turbulence scales well with the surface pressure.

In chapter three, we used the model to simulate the Martian water cycle, and compared results to observations of the annual water vapor cycle, as well as water-ice clouds. Initially, there were two major issues with the simulation results. First, the model

was too wet, because of high rates of sublimation from the northern polar ice cap during summer. Second, the model produced optically thick clouds over the northern pole during summer, something not currently observed. As the surface temperatures are highly coupled to the clouds and atmospheric water vapor, there is not a single, "magic" parameter that can be changed to solve the problems. For this study, we reduced the rate of sublimation by increasing the polar cap albedo. However, other methods could be used to achieve similar results, for example reducing the size of the polar caps. For the issue of the optically thick clouds in the model that are not in the observations, two possible scenarios exist. Either that there are actually very few clouds present at these latitudes, suggesting that the atmosphere is highly supersaturated, or that the clouds are present, but are optically thin. In order to reproduce the results, we assumed that there was an absence of clouds, and artificially forced supersaturation at high latitudes during the summer time. This suppressed cloud formation, and led to annual patterns for water vapor and cloud opacity similar to the observations. However, we have not considered the possibility of optically thin clouds. In the model, the clouds that form over the pole and at high latitudes were assumed to have particle sizes of 10 μm. The Phoenix Lander, situated at 68.22°N, observed particles with effective radii of 35 μm (Whiteway et al., 2009), almost a factor of 4 larger than the model cloud particles. As the cloud opacity scales inversely with size, such cloud particles would have reduced the model cloud opacities. However, the precise magnitude of the effect is difficult to predict due to the highly coupled nature of the system.

Chapter three also described simulations of the ancient Martian climate under various assumptions of the water cycle, such as the amount of initial atmospheric water,

the polar cap albedo, and the cloud particle sizes. We found that under certain assumptions it was possible to achieve stably warm climates with globally averaged surface temperatures near 265 K, and annual mean surface temperatures above the freezing temperature of water in the tropics. This indicates the possibility for a warm ancient Martian climate sustained by the greenhouse warming by the water cycle. These warm states could be brought on by either a low polar cap albedo (<0.4), or high initial atmospheric water content (>1000 pr-μm). They could be sustained if the cloud particle size was around 10 μm, and if the precipitation rates were sufficiently low, such that the atmospheric water lifetime became very long. The cloud particle size of 10 μm was very important for warming. At this size, the cloud particles are large enough to provide significant IR absorption, and small enough to have a high concentration of particles. Clouds with smaller particles did not have sufficient IR absorption relative to the shortwave, resulting in less energy reaching the surface for similar cloud masses. These cloud parameters led to a feedback effect, where the warming by the clouds released more water from the polar caps, which provided more atmospheric water vapor for warming, and the additional formation of clouds. The amount of atmospheric water vapor in the warm cases was almost 100 times higher than in the cold cases, at thousands of precipitable microns of water vapor, compared to tens.

Questions remain about whether or not the abnormally long lifetimes of water required in the warm states are realistic. It is possible that because the clouds tend to form at very high altitudes, and at very cold temperatures, that it would have been more difficult to remove water from the atmosphere compared to on Earth. Other questions that need to be addressed are how the planet could enter the warm states, and how the warm

states would end. The conditions required in the model to reach the warm states were either a low polar cap albedo, or high initial atmospheric water content. The required albedo of 0.4 is comparable to the present day cap albedo, so it could have been possible if the dust in the past was similar to today. If the albedo were higher, an injection of water to the system would have been needed to jump-start the warm state. The minimum amount of water required was around 1000 pr-μm of water (~1.5×10^{14} kg or about 150 km^3), which could have been provided by a modest sized impact, but is difficult to imagine even for a large volcanic eruption. The simulations at other surface pressures suggest that the warm climates cannot be sustained when the globally averaged surface pressure falls below 250 mb of CO_2. Some of the contributing factors to this include less CO_2 to act as a greenhouse gas, and perhaps even more important, if the surface pressure becomes too small, the atmosphere does not have a high enough volumetric heat capacity (ρc_p) to transport a significant amount of heat from the equator to the pole.

Conditions for maintaining a stably warm climate were found in chapter three. In chapter four, we studied the precipitation rates and patterns for these warm climates under varying obliquities, and with the presence of a northern ocean. In the low obliquity simulations, it was found that while the tropical surface temperatures could be above the freezing temperature of water without the presence of an ocean, average precipitation rates at the latitudes where the Noachian river valleys are simulated to be less than 1 mm/year. Precipitation rates above a few cm/year required snowfields and high obliquity. In contrast, when oceans were added in the northern hemisphere, Hellas basin, and Argyre basin, precipitation rates of 5-10 cm/year occurred at low latitudes even when the obliquity was low (<25°). This leads to two possible scenarios for river valley formation.

In the first scenario, an injection of water into the atmosphere probably via an impact set the climate into a warm state. If the obliquity were high, the water could precipitate across the planet, where it would accumulate and melt when the obliquity returned to a lower value. In the second scenario, the source of water would instead be oceans, probably they themselves created by a large impact. While the oceans would probably freeze at any obliquity, the ice still acts as a large source of water vapor through sublimation, providing water for precipitation at low latitudes. Similar to the non-ocean cases, the resulting precipitation tends to land at latitudes where the seasonal temperatures do not exceed the freezing temperature of water. However, unlike the non-ocean cases, modest precipitation occurs for all obliquities. Consequently, the seasonally warm temperatures at one obliquity tend to correspond to latitudes that see precipitation for other obliquities. This suggests a long-term continuous state, where for any given obliquity, water will precipitate as mostly as snow at certain latitudes, with annual rain and runoff of up to 1 cm per year. As the obliquity changes, the accumulated snow may melt to form streams. However, it is unknown if this snow would sublimate faster than the timescale for obliquity change, preventing the snow from melting and forming rivers. The presence of oceans would probably slow down the sublimation of low-latitude snow by humidifying the lower atmosphere, but determining whether or not this would be enough to keep the snow stable at the surface for tens of thousands of years with a 3-D GCM would require impractically long computation times.

In summary, we have developed a new Martian general circulation model from the terrestrial Community Atmosphere Model. The model has been validated through comparisons to various spacecraft observations, and has been shown to be a useful tool

for simulating the Martian climate. We have used this model to study the possible greenhouse warming in an ancient Martian climate with a 500 mb CO_2 atmosphere, and various settings for cloud physics. The results suggest that the ancient climate would have been extremely sensitive to the water cycle, and that it could have been anywhere from cold and dry, to stably warm. Finally, using the parameters that led to the most warming, we investigated the global precipitation rates and patterns with various obliquities and sources of water. These simulations showed that without an ocean or some other significant source of surface water, precipitation at river valley latitudes would be very small. With large snowfields precipitation was enhanced at high obliquities. However with oceans, even frozen ones, precipitation rates of 5-10 cm/year could occur at varying latitudes at all obliquities, indicating that for continuous formation of the river valleys, oceans, or perhaps exposed ground water, significant lakes and rivers would be important.

Because of the extreme sensitivity of the ancient Martian climate to the water cycle, it will be important in the future to be able to predict things like cloud particle sizes, nucleation rates, growth rates, sedimentation rates, and their dependences on temperature. Unfortunately, without in situ measurements of the ancient climate, it is difficult to know these things due to uncertainties in parameters such as cloud condensation nuclei concentration, spatial distribution, size distribution, etc. One of the most concrete constraints we found for the possibility of a stably warm climate was that the surface pressure had to be above 250 mb of CO_2. This pressure is needed because during winter, the polar temperatures over the cap needed to be high enough so that they sustain a cloud layer throughout the year. When the surface pressure fell below this value, the combined effect of reduced greenhouse warming from CO_2 and less efficient heat transport from the

equator to pole resulted in the climate not being able to sustain the water cycle, and thus the warm temperatures. Hopefully, the results from the upcoming Mars Atmosphere and Volatile Evolution Mission (MAVEN) will be able to answer the question of how thick the ancient Martian atmosphere could have been.

References

Allison, M., and Schmunk, R., 2008. http://www.giss.nasa.gov/tools/mars24/

Andrews-Hanna, J.C., and Lewis, K.W., 2011. Early Mars hydrology: 2. Hydrological evolution in the Noachian and Hesperian epochs, *J. Geophys. Res., 116,* E02007, doi:10.1029/2010JE003709.

Baker, V.R., Strom, R.G., Gulick, V.C., Kargel, J.S., Komatsu, G., and Kale, V.S., 1991. Ancient oceans, ice sheets and the hydrological cycle on Mars, *Nature, 352,* 589-594.

Banfield, J.L., Glotch, T.D., and Christensen, P.R., 2003. Spectroscopic identification of carbonate minerals in the Martian dust, *Science, 22,* 1084-1087.

Bardeen, C.G., et al., 2010. Numerical simulations of the three-dimensional distribution of polar mesospheric clouds and comparisons with Cloud Imaging and Particle Size (CIPS) experiment and the Solar Occultation For Ice Experiment (SOFIE) observations, *J. Geophys. Res., 115,* D10204, doi:10.1029/2009JD012451.

Businger, J.A., Wyngaard, J.C., Izumi, Y., Bradley, E.F., 1971. Flux-profile relationships in the atmospheric surface layer, *J. Atmos. Sci., 28,* 181-189.

Cahalan, R.F., Ridgway, W., Wiscombe, W. J., Golmer, S., and Harshvardan, 1994. Independent pixel and Monte Carlo estimates of stratocumulus albedo, *J. Atmos. Sci., 51,* 3776-3790.

Carr, M.H., and Head, J.W. III, 2003. Oceans on Mars: An assessment of the observational evidence and possible fate, *J. Geophys. Res., 108,* No. E5, 5042, doi:10.1029/2002JE001963.

Christensen, P.R., et al., 2001. Mars Global Surveyor Thermal Emission Spectrometer experiment: Investigation description and surface science results, *J. Geophys. Res., 106,* 23,823-23,872.

Clancy, R.T., et al., 1996. Water vapor saturation at low altitudes around Mars aphelion: A key to Mars climate?, *Icarus, 122,* 36-62.

Clancy, R.T., Wolff, M.J., and Christensen, P.R., 2003. Mars Aerosol Studies with the MGS TES Emission Phase Function Observations: Optical Depths, Particle Sizes, and Ice Cloud Types versus Latitude and Solar Longitude, *J. Geophys. Res., 108,* No. E9, 5098, doi:10.1029/2003JE002058.

Clifford, S.M., and Parker, T.J., 2001. The evolution of the Martian hydrosphere: Implications for the fate of a primordial ocean and the current state of the Northern Plains, *Icarus, 154,* 40-79.

Colaprete, A., and Toon, O.B., 2003. Carbon dioxide clouds in an early dense Martian atmosphere, *J. Geophys. Res., 108,* No. E4, 5025, doi:10.1029/2002JE001967.

Colaprete, A., Barnes, J.R., Haberle, R.M., and Montmessin, F., 2008. CO_2 clouds, CAPE and convection on Mars: Observations and general circulation modeling, *Planetary and Space Science, 56,* 150-180.

Colburn, D.S., Pollack, J.B., and Haberle, R.M., 1989. Diurnal Variations in Optical Depth at Mars, *Icarus, 79,* 159-189.

Collins, W.D., et al., 2004. Description of the NCAR Community Atmosphere Model (CAM 3.0), NCAR Technical Note.

Conrath, B.J., 1975. Thermal structure of the Martian atmosphere during the dissipation of dust storm 1971, *Icarus, 24,* 34-46.

Davis, S.M., Avallone, L.M., Kahn, B.H., Meyer, K.G., Baumgardner, D., 2009. Comparison of airborne in situ measurements and Moderate Resolution Imaging Spectroradiometer (MODIS) retrievals of cirrus cloud optical and microphysical properties during Midlatitude Cirrus Experiment (MidCiX), *J. Geophys. Res., 114,* D02203, doi:10.1029/2008JD010284.

Di Achille, G., and Hynek, B.M., 2010. Ancient ocean on Mars supported by global distribution of deltas and valleys, *Nature Geoscience, 3,* doi:10.1038/NGEO891.

Dohm, J.M., et al., 2009. GRS evidence and the possibility of paleooceans on Mars, *Planetary and Space Science, 57,* 664-684.

Elteto, A., and Toon, O.B., 2010. The effects and characteristics of atmospheric dust during martian global dust storm 2001A, *Icarus, 210,* 589-611.

Fairen, A.G., Davila, A.F., Gago-Duport, L., Haqq-Misra, J.D., Gil, C., McKay, C.P., and Kasting, J.F., 2011. Cold glacial oceans could have inhibited phyllosilicate sedimentation on early Mars, *Nature Geoscience, 4,* 667-670.

Farmer, C.B., Davies, D.W., Holland, A.L., La Porte, D.P., and Doms, P.E., 1977. Mars: Water vapor observations from the Viking orbiters, *J. Geophys. Res., 82,* 4225-4248.

Fassett, C.I., and Head, J.W., 2008a. Valley network-fed, open-basin lakes on Mars: Distribution and implications for Noachian surface and subsurface hydrology, *Icarus, 198,* 37-56.

Fasset, C.I., and Head, J.W., 2008b. The timing of Martian valley network activity: constraints from buffered crater counting, *Icarus, 195,* 61-89, doi:10.1016/j.icarus.2007.12.009.

Flatau, P.J., Walko, R.L., and Cotton, W.R., 1992. Polynomial fits to saturation vapor pressure, *J. Appl. Meteor., 31,* 1507-1513.

Forget, F., and Pierrehumbert, R.T., 1997. Warming early Mars with carbon dioxide clouds that scatter infrared radiation, *Science, 278,* 1273-1276.

Forget, F., et al., 1999. Improved general circulation models of the martian atmosphere from the surface to above 80 km, *J. Geophys. Res, 104,* 24,155-24,176.

Goff, J. A., and Gratch, S., 1946. Low-pressure properties of water from -160 to 212 F, in Transactions of the American society of heating and ventilating engineers, pp 95-122, presented at the 52nd annual meeting of the American society of heating and ventilating engineers, New York.

Haberle, R.M., et al., 1993. Mars atmospheric dynamics as simulated by the NASA/Ames general circulation model, 1, the zonal-mean circulation, *J. Geophys. Res., 98,* 3093-3124.

Haberle, R.M., Barnes, J.R., Murphy, J.R., Joshi, M.M., and Schaeffer, J., 1997. Meteorological predictions for the Mars Pathfinder lander, *J. Geophys. Res., 102,* 13,301-13,311.

Haberle, R.M., 1998. Early Mars Climate Models, *J. Geophys. Res., 103,* 28,467-28,480.

Haberle, R.M., et al., 1999. General circulation model simulations of the Mars Pathfinder atmospheric structure investigation/meteorology data, *J. Geophys. Res., 104,* 8957-8974.

Haberle, R.M., Murphy, J.R., Schaeffer, J., 2003. Orbital change experiments with a Mars general circulation model, *Icarus, 161,* 66-89.

Haberle, R.M. et al., 2003. The NASA/Ames Mars General Circulation Model: Model improvements and comparison with observations, NASA Technical Report.

Haberle, R.M., et al., 2011. Radiative effects of water ice clouds on the Martian seasonal water cycle, *Fourth international workshop on the Mars atmosphere: Modeling and observations*.

Hansen, J.E. and Travis, L.D., 1974. Light scattering in planetary atmospheres, *Space Science Reviews, 16*, 527-610.

Haqq-Misra, J.D., Domogal-Goldman, S.D., Kasting, P.J., and Kasting, J.F., 2008. A revised, hazy methane greenhouse for the archean Earth, *Astrobiology, 8,* No. 6, doi:10.1089/ast.2007.0197.

Hartogh, P., Medvedev, A.S., Kuroda, T., Saito, R., and Villanueva, G., 2005. Description and climatology of a new general circulation model of the Martian atmosphere, *J. Geophys. Res., 110*, E11008, doi:10.1029/2005JE002498.

Head, J.W. III, Hiesinger, H., Ivanov, M.A., Krelavsky, M.A., Pratt, S., and Thomson, B.J., 1999. Possible ancient oceans on Mars: Evidence from Mars Orbiter Laser Altimeter data, *Science, 286,* 2134-2137.

Hinson, D.P., Patzold, M., Tellmann, S., Hausler, B., and Tyler, G.L., 2008. The depth of the convective boundary layer on Mars, *Icarus, 198*, 57-66.

Hoke, M.R.T., Hynek, B.M., 2009. Roaming zones of precipitation on Mars as recorded in valley networks, *J. Geophys. Res., 114*, doi:10.1029/2008JE003247.

Holt, J.W., et al., 2008. Radar sounding evidence for buried glaciers in the southern mid-latitudes of Mars, *Science, 322,* 1235-1238.

Horne, D., and Smith, M.D., 2009. Mars Global Surveyor Thermal Emission Spectrometer (TES) observations of variations in atmospheric dust optical depth over cold surfaces, *Icarus, 200*, 118-128.

Hourdin, F., Van, P.L., Forget, F., and Talagrand, O., 1993. Meteorological variability and the annual surface pressure cycle on Mars, *J. Atmos. Sci., 50*, 3625-3640.

Hourdin, F., Forget, F., and Talagrand, O., 1995. The sensitivity of the Martian surface pressure to various parameters: A comparison between numerical simulations and Viking observations, *J. Geophys. Res., 100*, 5501-5523.

Hynek, B.M., and Phillips, R.J., 2001. Evidence for extensive denudation of the Martian highlands, *Geology, 29*(5), 407– 410.

Hynek, B.M., and Phillips, R.J., 2003. New data reveal mature, integrated drainage systems on Mars indicative of past precipitation, *Geology*, *31*(9), 757–760.

Hynek, B.M., Beach, M., and Hoke, M.R.T., 2010. Updated global map of Martian valley networks and implications for climate and hydrologic processes, *J. Geophys. Res., 115*, E09008, doi:10.1029/2009JE003548.

Iraci, L.T., Phebus, B.D., Stone, B.M., Colaprete, A., 2010. Water ice cloud formation on Mars is more difficult than presumed: Laboratory studies of ice nucleation on surrogate materials, *Icarus, 210*.

Jakosky, B.M., and Farmer, C.B., 1982. The seasonal and global behavior of water vapor in the Mars atmosphere: Complete global results of the Viking atmospheric water detector experiment, *J. Geophys. Res., 87*, No. B4, 2999-3019.

Jakosky, B.M., Henderson, B.G., Mellon, M.T., 1995. Chaotic obliquity and the nature of the Martian climate, *J. Geophys. Res., 100*, 1579-1584.

James, P.B., 1990. The role of water ice clouds in the Martian hydrologic cycle, *J. Geophys. Res., 95*, No. B2, 1439-1445.

Jensen, E.J., O.B. Toon, H.B. Selkirk, J.D. Spinhirne, and M.R. Schoeberl, 1996. On the formation and persistence of subvisible cirrus clouds near the tropical tropopause, *J. Geophys. Res., 101*, NO. D16, 21,361-21,375.

Kahn, R., 1984. The spatial and seasonal distribution of Martian clouds, and some meteorological implications, *J. Geophys. Res., 89*, 6671-6688.

Kasting, J.F., Pollack, J.B., and Ackerman, T.P., 1984. Response of Earth's atmosphere to increases in solar flux and implications for loss of water from Venus, *Icarus, 57*, 335-355.

Kasting, J.F., 1991. CO_2 Condensation and the Climate of Early Mars, *Icarus, 90*, 1-13.

Kiehl, J.T. and Briegleb, B.P., 1991. A new parameterization of the absorptance due to the 15 μm band system of carbon dioxide, *J. Geophys. Res., 96*, 9013-9019.

Kiehl, J.T. and Ramanathan, V., 1983. CO_2 radiative parameterization used in climate models: comparison with narrow band models and with laboratory data, *J. Geophys. Res., 88*, 5191-5202.

Kite, E.S., Michaels, T.I., Rafkin, S., Manga, M., and Dietrich, W.E., 2011. Localized precipitation and runoff on Mars, *J. Geophys. Res., 116*, E07002, doi:10.1029/2010JE003783.

Kuroda, T., Hashimoto, N., Sakai, D., and Takahashi, M., 2005. Simulation of the Martian Atmosphere Using a CCSR/NIES AGCM, *J. Met. Soc. Jpn., 83,* 1, 1-19.

Laskar, J., and Robutel, P., 1993. The chaotic obliquity of the planets, *Nature, 361,* 608-612.

Laskar, J., Correia, A.C.M., Gastineau, M., Joutel, F., Levrard, B., and Robutel, P., 2004. Long term evolution and chaotic diffusion of the insolation quantities of Mars, *Icarus, 170,* 343-364.

Lefevre, F., Lebonnois, S., Montmessin, F., and Forget, F., 2004. Three-dimensional modeling of ozone on Mars, *J. Geophys. Res., 109,* E07004, doi:10.1029/2004JE002268.

Levitus, S., 1982. Climatological atlas of the world ocean, Technical Report NOAA Professional Paper 13, National Oceanic and Atmospheric Administration.

Leovy, C.B., et al., 1972. The Martian atmosphere: Mariner 9 television experiment progress report, *Icarus, 17,* 373-393, doi:10.1016/0019-1035(72)90006-1.

Leovy, C., and Y. Mintz, 1969. Numerical simulation of the atmospheric circulation and climate of Mars, *J. Atmos. Sci., 26,* 1167-1190.

Lin, S.-J., and Rood, R.B., 1996. Multidimensional flux form semi-lagrangian transport schemes, *Mon. Wea. Rev., 124,* 2046-2070.

Lin, Y.-L., Farley, R.D., and Orville, H.D., 1983. Bulk parameterization of the snow field in a cloud model, *J. Climate and App. Met., 22,* 1065-1092.

Maattanen, A. et al., 2005. Nucleation studies in the Martian atmosphere, *J. Geophys. Res., 110,* E02002, doi:10.1029/2004JE002308.

Machtoub, G., 2012. Modeling the hydrological cycle on Mars, *J. Advances in Modeling Earth Systems, 4,* M03001, doi:10.1029/2011MS000069.

Maltagliati, L. et al., 2011. Evidence of water vapor in excess of saturation in the atmosphere of Mars, *Science, 333,* doi:10.1126/science.1207957.

McCleese, D.J., et al., 2007. Mars Climate Sounder: An investigation of thermal and water vapor structure, dust and condensate distributions in the atmosphere, and energy balance of the polar regions, *J. Geophys. Res., 112,* E05S06, doi:10.1029/2006JE002790.

McKay, C.P., and Davis, W.L., 1991. Duration of liquid water habitats on early Mars, *Icarus, 90,* 214-221.

Mellon, M.T., Jakosky, B.M., 1995. The distribution and behavior of Martian ground ice during past and present epochs, *J. Geophys. Res., 100,* 11,781-11,800.

Mellon, M.T., Jakosky, B.M., and Christensen, P.R., 2000. High-Resolution Thermal Inertia Mapping from the Mars Global Surveyor Thermal Emission Spectrometer, *Icarus, 148,* 437-455.

Mischna, M., Richardson, M.I., Wilson, R.J., McCleese, D.J., 2003. On the orbital forcing of Martian water and CO_2 cycles: A general circulation model study with simplified volatile schemes, *J. Geophys. Res., 108,* No. E6, 5062, doi:10.1029/2003JE002051.

Montmessin, F., Forget, F., Rannou, P., Cabane, M., and Haberle, R.M., 2004. Origin and role of water ice clouds in the Martian water cycle as inferred from a general circulation model, *J. Geophys. Res. 109,* E10004, doi: 10.1029/2004E002284.

Moudden, Y. and McConnell, J.C., 2005. A new model for multiscale modeling of the Martian atmosphere, GM3, *J. Geophys. Res., 110,* E04001, doi:10.1029/2004JE002354.

Murphy, D.M. and Koop, T., 2005. Review of the vapour pressures of ice and supercooled water for atmospheric applications, *Quart. J. Royal Met. Soc., 131,* 1539-1565.

Murphy, J.R., Leovy, C.B., Tillman, J.E., 1990. Observations of the Martian Surface Winds at the Viking Lander 1 Site, *J. Geophys. Res., 95,* 14,555-14,576.

Murphy, J.R., Toon, O.B., Haberle, R.M., and Pollack, J.B., 1990. Numerical Simulations of the Decay of Martian Global Dust Storms, *J. Geophys. Res., 95,* B9, doi:10.1029/JB095iB09p14629.

Murphy, J.R., Haberle, R.M., Toon, O.B., and Pollack, J.B., 1993. Martian Global Dust Storms: Zonally Symmetric Numerical Simulations Including Size-Dependent Particle Transport, *J. Geophys. Res., 98,* E2, doi:10.1029/92JE02945.

Murphy, J.R., et al., 1995. Three-dimensional numerical simulation of Martian global dust storms, *J. Geophys. Res., 100,* E12, PP. 26,357-26,376.

Nelli, S.M., Murphy, J.R., Feldman, W.C., and Schaeffer, J.R., 2009. Characterization of the nighttime low-latitude water ice deposits in the NASA Ames Mars General Circulation Model 2.1 under present-day atmospheric conditions, *J. Geophys. Res., 114,* E11003, doi:10.1029/2008JE003289.

Oleson, K.W., et al., 2004 Technical Description of the Community Land Model (CLM), *NCAR/TN-461+STR.*

Oreopoulos, L., and Barker, H.W., 1999. Accounting for subgrid-scale cloud variability in a multi-layer 1D solar radiative transfer algorithm, *Q. J. R. Meteorol. Soc., 125*, 301– 330.

Paige, D.A., and Ingersoll, A.P., 1985. Annual heat balance of Martian polar caps: Viking observations, *Science, 228*, 1160-1168.

Paige, D.A., Bachman, J.E., and Keegan, K.D., 1994. Thermal and albedo mapping of the polar regions of Mars using Viking thermal mapper observations: 1. North polar region, *J. Geophys. Res., 99*, No. E12, 25,959-25,991.

Pang, H.L. Atten, P., and Reboud, J.-L., 2005. Corona discharge and electrostatic precipitation in carbon dioxide under reduced pressure simulating Mars atmosphere, *IEEE Trans. Ind. Appl., 1*, 346-353.

Parker, T.J., Saunders, R.S., and Schneeberger, D.M., 1989. Transitional morphology in West Deuteronilus Mensae, Mars: Implications for modification of the Lowland/Upland boundary, *Icarus, 82*, 114-145.

Parker, T.J., Gorsline, D.S., Saunders, R.S., Pieri, D.C., and Schneeberger, D.M., 1993. Coastal geomorphology of the Martian northern plains, *J. Geophys. Res., 98*, 11,061-11,078.

Pavlov, A.A., Kasting, J F., Brown, L.L., Rages, K.A., and Freedman, R., 2000. Greenhouse warming by CH_4 in the atmosphere of early Earth, *J. Geophys. Res., 105*, E5, 11,981-11,990.

Pfister, L., et al., 2001. Aircraft observations of thin cirrus clouds near the tropical tropopause, *J. Geophys. Res., 106*, No. D9, 9765-9786.

Phillips, R.J., et al., 2001. Ancient geodynamics and global-scale hydrology on Mars, *Science, 291*, 2587, doi:10.1126/science.1058701.

Pincus, R., Barker, H.W., and Morcrette, J.-J., 2003. A fast, flexible, approximate technique for computing radiative transfer in inhomogeneous cloud fields, *J. Geophys. Res., 108*(D13), 4376, doi:10.1029/2002JD003322.

Pollack, J.B., Leovy, C.B., Greiman, P.W., and Mintz, Y., 1981. General Circulation Model experiment with large topography, *J. Atmos. Sci, 28*, 3-29.

Pollack, J.B. and McKay, C.P., 1985. The impact of polar stratospheric clouds on the heating rates of the winter polar stratosphere, *J. Atmos. Sci., 42*, No. 3, 245-262.

Pollack, J.B., Kasting, J.F., Richardson, S.M., and Poliakoff, K., 1987. The case for a wet, warm climate on early Mars, *Icarus, 71*, 203-224.

Pollack, J.B., Haberle, R.M., Schaeffer, J., and Lee, H., 1990. Simulations of the general circulation of the Martian atmosphere 1, Polar processes, *J. Geophys. Res., 95*, 1447-1473.

Pollack, J.B., Haberle, R.M., Murphy, J.R., Schaeffer, J., and Lee, H., 1993. Simulations of the general circulation of the Martian atmosphere 2, Seasonal pressure variations, *J. Geophys. Res., 98*, 3149-3181.

Putzig, N.E., Mellon, M.T., 2007. Apparent thermal inertia and the surface heterogeneity of Mars, *Icarus, 191*, 68-94, doi: 10.1016/j.icarus.2007.05.013.

Rasch, P.J., and Kristjansson, J.E., 1998. A comparison of the CCM3 model climate using diagnosed and predicted condensate parameterizations, *J. Climate, 11*, 1587-1614.

Richardson, M.I., and Wilson, R.J., 2002. Investigation of the nature and stability of the Martian seasonal water cycle with a general circulation model, *J. Geophys. Res., 107*, No. E5, 10.1029/2001JE001536.

Richardson, M.I., Wilson, R.J., and Rodin, A.V., 2002. Water ice clouds in the Martian atmosphere: General circulation model experiments with a simple cloud scheme, *J. Geophys. Res., 107*, No. E9, 5064, doi:10.1029/2001JE001804.

Richardson, M.I., Toigo, A.D., and Newman, C.E., 2007. PlanetWRF: A general purpose, local to global numerical model for planetary atmospheric and climate dynamics, *J. Geophys. Res., 112*, E09001, doi:10.1029/2006JE002825.

Salby, M.L., 1996. *Fundamentals of Atmospheric Physics*, Elsevier, 336-338.

Savijarvi, H., 1995. Mars boundary layer modeling: Diurnal moisture cycle and soil properties at the Viking Lander 1 site, *Icarus, 117*, 120-127.

Segelstein, D., 1981. The Complex Refractive Index of Water, M.S. Thesis, University of Missouri, Kansas City, Missouri.

Segura, T.L., Toon, O.B., Colaprete, A., Zahnle, K., 2002. Environmental effects of large impacts on Mars, *Science, 298,* 1977, doi:10.1126/science.1073586.

Segura, T.L., Toon, O.B., Colaprete, A., 2008. Modeling the environmental effects of moderate-sized impacts on Mars, *J. Geophys. Res., 113*, E11007, doi:10.1029/2008JE003147.

Sleep, N.H., and Zahnle, K., 1998. Refugia from asteroid impacts on early Mars and the early Earth, *J. Geophys. Res., 103,* 28,529-28544.

Slingo, J. M., 1987. The development and verification of a cloud prediction scheme for the ECMWF model, *Q. J. R. Meteorol. Soc., 113*, 899–927.

Smith, D.E., Zuber, M.T., and Neumann, G.A., 2001. Seasonal Variations of Snow Depth on Mars, *Science, 294*, 2141-2146.

Smith, D., Neumann, G., Arvidson, R.E., Guinness, E.A., and Slavney, S., 2003. Mars Global Surveyor Laser Altimeter Mission Experiment Gridded Data Record, NASA Planetary Data System, MGS-M-MOLA-5-MEGDR-L3-V1.0.

Smith, M.D., Pearl, J.C., Conrath, B.J., and Christensen, P.R., 2001. One Martian year of atmospheric observations by the Thermal Emission Spectrometer, *Geophys. Res. Lett., 28, 22,* 4263-4266.

Smith, M.D., 2004. Interannual variability in TES atmospheric observations of Mars during 1999-2003, *Icarus, 167,* 148-165.

Smith, M.D., et al., 2006. One Martian year of atmospheric observations using MER Mini-TES, *J. Geophys. Res., 111,* E12S13, doi: 10.1029/2006JE002770.

Smith, M.D., 2008. Spacecraft Observations of the Martian Atmosphere, *Annu. Rev. Earth Planet. Sci.,* doi:10.1146/annurev.earth.36.031207.124334.

Spiga, A., Forget, F., Lewis, S.R., and Hinson, D.P., 2010. Structure and dynamics of the convective boundary layer on Mars as inferred from large-eddy simulations and remote-sensing measurements, *Q.J.R. Meteorol. Soc., 136*, 414-428.

Stephens, G. L., 1988. Radiative transfer through arbitrarily shaped optical media. 1. A general method of solution, *J. Atmos. Sci., 45*, 1818– 1836.

Sundqvist, H., 1988. Parameterization of condensation and associated clouds in models for weather prediction and general circulation simulation, *Physically-based Modeling and Simulation of Climate and Climate Change, Vol. 1*, edited by M. E. Schlesinger, 433–461, Kluwer Academic.

Sutton, J.L., Leovy, C.B., Tillman, J.E., 1978. Diurnal variations of the Martian surface layer meteorological parameters during the first 45 sols at two Viking lander sites, *J. Atmos. Sci., 35*, 2346-2355.

Thomas, M.E. and Nordstrom, R.J., 1985. Line shape model for describing infrared absorption by water vapor, *Applied Optics, 24,* 3526-3530.

Tian, F., Kasting, J.F., Solomon, S.C., 2009. Thermal escape of carbon from the early Martian atmosphere, *Geophys. Res. Lett., 36,* L02205, doi:10.1029/2008GL036513.

Toon, O. B., Pollack, J.B., Ward, W., Burns, J., and Bilski, K., 1980. The Astronomical Theory of Climate Change on Mars, *Icarus, 44*, 552-607.

Toon, O.B., Turco, R.P., Westphal, D., Malone, R., and Liu, M.S., 1988. A Multidimensional Model for Aerosols: Description of Computational Analogs, *J. Atmos. Sci., 45*, 2123-2143.

Toon, O.B., Mckay, C.P., Ackerman, T.P., and Santhanam, K., 1989. Rapid calculation of radiative heating rates and photodissociation rates in inhomogeneous multiple-scattering atmospheres, *J. Geophys. Res., 94*, 16,287-16,301.

Toon, O.B., Segura, T., and Zahnle, K., 2010. The formation of Martian river valleys by impacts, *Annu. Rev. Earth Planet. Sci., 38*, 303-322.

Touma, J., and Wisdom, J., 1993. The chaotic obliquity of Mars, *Science, 259*, 1294-1297.

Trainer, M.G., Toon, O.B., Tolbert, M.A., 2009. Measurements of depositional ice nucleation on insoluble substrates at low temperatures: implications for Earth and Mars, *J. Phys. Chem. C, 113,* 2036-2040.

Urata, R.A., and Toon, O.B., 2012a. A new general circulation model for Mars based on the NCAR Community Atmosphere Model, *Icarus, submitted*.

Urata, R.A., and Toon, O.B., 2012b. Simulations of the Martian hydrologic cycle with a general circulation model: Implications for the ancient Martian climate, *Icarus, submitted*.

Wang, H., and Ingersoll, A.P., 2002. Martian clouds observed by Mars Global Surveyor Mars Orbiter Camera, *J. Geophys. Res., 107*, doi:10.29/2001JE001815.

Warren, S.G., Wiscombe, W.J., and Firestone, J.F., 1990. Spectral albedo and emissivity of CO_2 in Martian polar caps: Model results, *J. Geophys. Res., 95*, No. B9, 14,717-14,741.

Warren, S.G., and Brandt, R.E., 2008. Optical constants of ice from the ultraviolet to the microwave: A revised compilation, *J. Geophys. Res., 113*, D14220, doi:10.1029/2007JD009744.

Whiteway, J.A., et al., 2009. Mars water-ice clouds and precipitation, *Science, 325, 68*, doi:10.1126/science.1172344.

Williams, D.R., Mars Fact Sheet, http://nssdc.gsfc.nasa.gov/planetary/factsheet/marsfact.html

Wilson, R.J., and Hamilton, K., 1996. Comprehensive model simulation of thermal tides in the Martian atmosphere, J. Atmos. Sci, 53, No. 9, 1290-1326.

Wolff, M.J., Clancy, R.T., 2003. Constraints on dust aerosols from the Mars Exploration Rovers using MGS overflights and Mini-TES, *J. Geophys. Res. 111,* E12517.

Wordsworth, R., Forget, F., Eymet, V., 2010. Infrared collision-induced and far-line absorption in dense CO_2 atmospheres, *Icarus, 210,* 992-997.

Wordsworth, R., Forget, F., Millour, E., Madeleine, J.-B., Charnay, B., Haberle, R., 2011. Modeling the past Mars climate and water cycle with a thicker CO_2 atmosphere, *Fourth international workshop on the Mars atmosphere: Modeling and observations.*

Zhang, M., Lin, W., Bretherton, C.S., Hack, J.J., and Rasch, P.J., 2003. A modified formulation of fractional stratiform condensation rate in the NCAR community atmospheric model CAM2, *J. Geophys. Res., 108* (D1).

Zhao, Q., Black, T.L., and Baldwin, M.E., 1997. Implementation of the cloud prediction scheme in the eta model at NCEP, *NCEP NOTES,* 697-712.

Appendix A. Water vapor pressure over ice.

We have replaced the equation for saturation vapor pressure over ice in the model with the Murphy-Koop relation (Murphy and Koop, 2005). This is derived as an exponential fit to the Clausius-Clapeyron equation with an experimentally determined temperature-dependent heat capacity. While this equation agrees with the Goff-Gratch (1946) equation for saturation vapor pressure over ice used in the atmosphere physics to within a few percent down to 100 K, the land physics used an eighth-order polynomial fit to the equation (Flatau et al., 1992) only valid to 198 K, below which the equation greatly strays from the correct answers. The vapor pressure equation in the land and atmosphere subroutines was replaced with the Murphy-Koop relations, valid for the low temperatures found on Mars.